THE VARIATIONS OF GEOMAGNETIC ENERGY AND SOLAR IRRADIANCE AND THEIR IMPACTS ON EARTH'S UPPER ATMOSPHERE

by

YANSHI HUANG

Presented to the Faculty of the Graduate School of
The University of Texas at Arlington in Partial Fulfillment
of the Requirements
for the Degree of

DOCTOR OF PHILOSOPHY

THE UNIVERSITY OF TEXAS AT ARLINGTON
December 2012

ACKNOWLEDGEMENTS

I am sincerely and heartily grateful to my Advisor Dr. Yue Deng, for her constant motivation and encouragement throughout my doctoral study. I feel very fortunate to have Dr. Deng as my advisor, who saw the potential in me and gave me the great opportunity to continue my graduate study. She has mentored me with her knowledge in Space Physics and gracious support over the years. It was a rewarding journey working with her.

I wish to thank my dissertation committee members: Dr. Yue Deng, Dr. Ramon Lopez, Dr. Zdzislaw Musielak, Dr. Manfred Cuntz and Dr. Qiming Zhang, for their interest in my research and valuable comments. This dissertation would not have been completed without their support.

I would like to express my appreciation to Dr. Arthur Richmond at the High Altitude Observatory (HAO) of the National Center for Atmospheric Research (NCAR) for mentoring me during my visits at HAO. His knowledge has greatly deepened my understanding about the upper atmosphere and NCAR Thermosphere-Ionosphere-Electrodynamics General Circulation Model (TIE-GCM). I am very grateful for his effort to improve my scientific skills and paper writing. Part of this work was conducted while I and Dr. Yue Deng were visitors in the Advanced Study Program at the National Center for Atmospheric Research, which is sponsored by the National Science Foundation.

I would also like to thank all my friends and colleagues at University of Texas at Arlington, University of Michigan and HAO for encouraging and inspiring me to finish this dissertation.

My special thanks go to my family: my parents, brother, sister-in-law and nephews, for their unconditional love and support throughout my life.

I am truly thankful to everyone who provided data for studies in this dissertation, including Dr. Stanley Solomon and Dr. Liying Qian at NCAR for solar index data, Dr. Phillip Chamberlin for the Flare Irradiance Spectral Model (FISM) data, Dr. Tobiska for SOLAR2000 data, and Dr. John Emmert for neutral density data. This research was supported by the National Science Foundation through grant ATM0955629.

October 1, 2012

ABSTRACT

THE VARIATIONS OF GEOMAGNETIC ENERGY AND SOLAR IRRADIANCE AND THEIR IMPACTS ON EARTH'S UPPER ATMOSPHERE

Yanshi Huang, Ph.D.
The University of Texas at Arlington, 2012

Supervising Professor: Yue Deng

The primary energy sources of Earth's upper atmosphere are the solar irradiance and geomagnetic energy including Joule heating and particle precipitation. Various data and models are utilized to investigate the variations of energy inputs and their influences on the coupled thermosphere-ionosphere system. First, the Flare Irradiance Spectral Model (FISM) has been used and the data show that the solar irradiance enhancement has wavelength dependence during flare events, and the solar irradiance increased largest in the XUV range. NCAR Thermosphere-Ionosphere-Electrodynamics General Circulation Model (TIE-GCM) simulations for the X17.2-class flare event on October 28^{th}, 2003 (X17.2) show that the impact of solar irradiance enhancement on the high-altitude thermosphere (400 km) is largest in the EUV wavebands instead. Secondly, the energy transfer processes into the upper atmosphere associated with high-speed solar wind stream has been investigated. It is a combination of Joule heating and particle precipitation, while Joule heating may play a more important role. We studied the high-latitude forcing from the measurements of DMSP satellite, empirical model Weimer05 and Assimilative mapping of ionospheric electrodynamics

(AMIE) model. The yearly average of the northern hemisphere integrated Joule heating (IJH) calculated from AMIE is 85% larger than that from Weimer05. Thirdly, the TIE-GCM model has been used to examine the altitudinal distribution of Joule heating and its influence on the upper atmosphere. The simulation results indicate that most of the Joule heating is deposited under 150 km. For solar minimum, Joule heating above 150 km (18% of total heat) causes about 60% of the total temperature variation and 50% of the total density variation, while for solar maximum, 34% of the total heat is above 150 km and results in 90% of the temperature variation and 80% density variation. This indicates that the high-altitude Joule heating has a stronger impact on the atmosphere at 400 km. At last, the long-term variation of different energy inputs in the last solar cycle has been studied as well. The solar EUV power in last solar minimum (2008) was reduced by 33 GW compared to the previous solar minimum (1996). The reduction of the total geomagnetic energy was close to 29 GW including 13 GW for Joule heating and 16 GW for particle precipitation. The change of the geomagnetic energy from 1996 to 2008 was comparable to that of the solar EUV power. The TIE-GCM simulations indicate that the variation of the solar irradiance and the geomagnetic energy accounts for 3/4 and 1/4 of the total neutral density reduction in 2008, respectively.

TABLE OF CONTENTS

LIST OF ILLUSTRATIONS

LIST OF TABLES

Table Page

CHAPTER 1

INTRODUCTION

1.1 Solar Physics

1.1.1 Structure

The primary compositions of the Sun are hydrogen (90%), helium (10%) and a small fraction of heavier elements such as C, N and O (0.1%). The energy is generated by nuclear reactions in the core and is transferred outward through the radiative zone, the convection zone and the atmosphere [81, 155]. Most of the Sun's energy is produced in the core, which extends from the center to about 0.25 solar radii. Radiation is the primary energy transfer mechanism below ~ 0.7 solar radii. The plasma density and temperature decrease with altitude [137]. At about 0.7 solar radii, the temperature is not high enough to strip electrons off of the nuclei. Atoms with electrons absorb photons easily, slowing down the transfer of energy by radiation significantly. Convection becomes the most efficient way to transfer energy in this region. The hotter gas rises upward and cools down at the photosphere, then sinks again downward to the top of the radiative zone [37]. The solar atmosphere consists of four layers. The lowest thin photosphere is the apparent solar surface which emits most of the sunlight such as solar visible and IR radiation [29]. Above the photosphere is the next layer known as the chromosphere, where the temperature increases from 4200 K to $\sim 10^4$ K due to the energy absorption of acoustic, gravity and magnetohydrodynamic waves merging from the convection zones [127]. The chromosphere is the source region of ultraviolet (UV) radiation and several transition lines, such as H-α. Although solar UV radiation only contains about 7% of the total radiation, it is very important in the terrestrial upper atmosphere. The uppermost layer of the solar atmosphere is known as the solar corona, which extends into the interplanetary space and becomes the solar wind. In this region the plasma temperature increases rapidly from $\sim 10^4$ K to $\sim 10^6$ K [73]. The structure of solar interior is depicted in Figure 1.1.

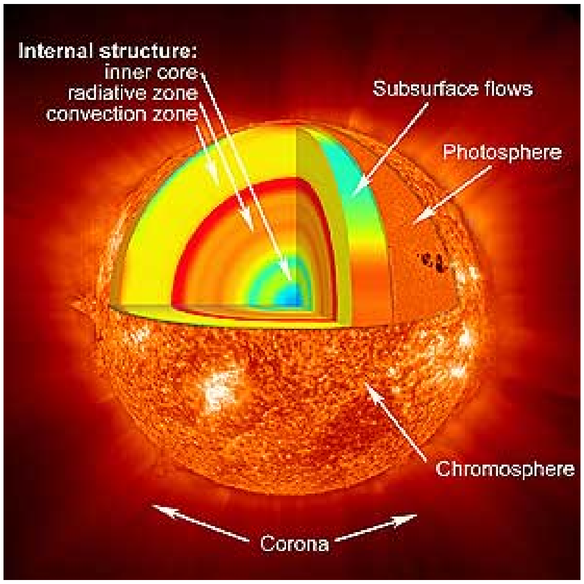

Figure 1.1. The structure of solar interior (Courtesy of University of Northern Colorado).

1.1.2 Solar Cycle

The complicated solar magnetic fields are generated by the large-scale motions of conducting fluid [14]. It can be either closed (the magnetic field lines emerging from one region on the Sun return back to another region on the Sun) or open (the magnetic lines emerging from the Sun extend outward into the interplanetary space) [37]. The closed field line regions are correlated with bright coronal regions due to the relatively dense plasma trapped there. In an open field line regions, plasma is allowed to escape and the plasma density is relatively lower. These areas filled with low density cold plasma appear dark in the solar X ray images, and are known as coronal holes [110]. The high-speed solar wind streams are coming from these coronal holes [34] as shown in Figure 1.2, while the low-speed solar wind streams are coming from the coronal helmet streamers that are associated with closed magnetic fields [72].

The rotation period of the Sun varies with solar latitudes. The Sun rotates faster at the equator than near its poles, varying from 24.9 days at equator to 31.5 days near poles. This phenomenon is called differential rotation which is due to the fact that the Sun is not solid. On average, an about 27 days of recurrence of solar activity is expected [114, 3]. The Sun is the ultimate energy source to the solar system in forms of irradiance, magnetic field and particles. Therefore, changes in solar activity

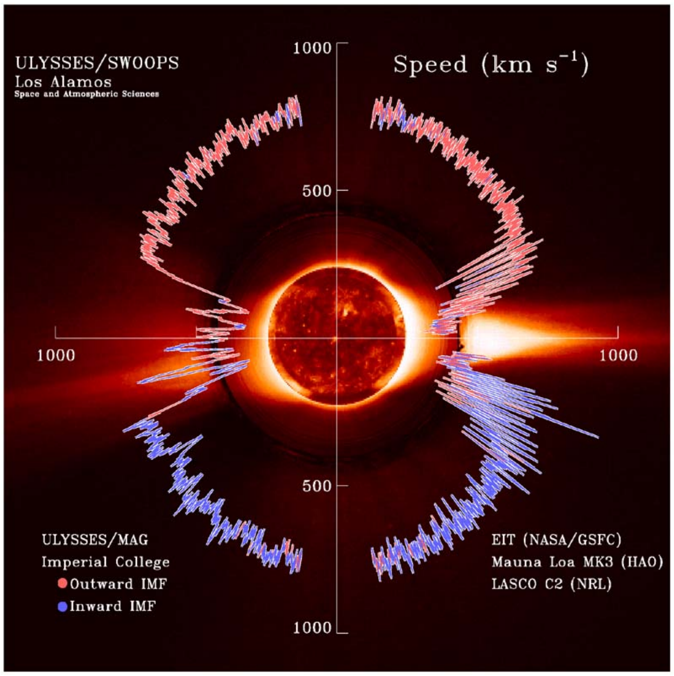

Figure 1.2. Plot of the solar wind speed over the Ulysses spacecraft orbit during solar minimum. It shows slow wind over the equator and fast wind over poles (Coronal hole) [67].

such as solar flares and coronal mass ejection result in important phenomena in the space environment.

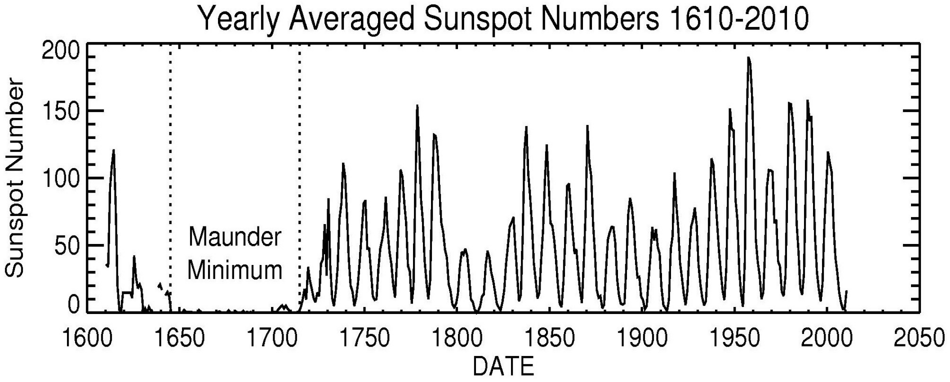

Figure 1.3. The observation of sunspot numbers from year 1600 to 2010 (Courtesy of NASA/MSFC, *http : //www.nasa.gov*).

The solar activity is often described by the sunspot numbers. Sunspots are dark areas on the solar surface which result from strong local magnetic fields (∼2000G) at the surface with cold plasma [37]. The time interval between a sunspot minimum (also called solar minimum) and the next sunspot minimum is called a solar cycle, which is generated by the evolution of solar magnetic fields through the cycle [137]. The period of solar cycle varies a lot from 8 to 15 years with an average of about 11.1 years [83]. There was a near disappearance of sunspots between 1640 to 1700, called Maunder minimum [22]. The recording of solar sunspot numbers began in 1755[46]. The 23rd solar cycle lasted 12.6 years, beginning in May 1996 and ending in December 2008. During this solar cycle, there were a total of 805 days with no sunspots (http://spaceweather.com/glossary/spotlessdays.htm). Figure 1.3 shows the sunspot numbers recorded from year 1600 to 2010. The 11-year regular variation of sunspot numbers is accompanied by a similar variation in the latitude distribution of sunspots and in the polarity of their magnetic fields. As the solar cycle progresses from solar minimum to maximum, the sunspots drift toward the equator. The sunspot groups in the next solar cycle are of opposite polarities. A 22-year magnetic solar oscillation results from this 11-year reversal of sunspot group polarities defines [37]. The solar cycle modulated the solar irradiance flux and the occurrence frequency of geoeffective events, such as solar flares and coronal mass ejections.

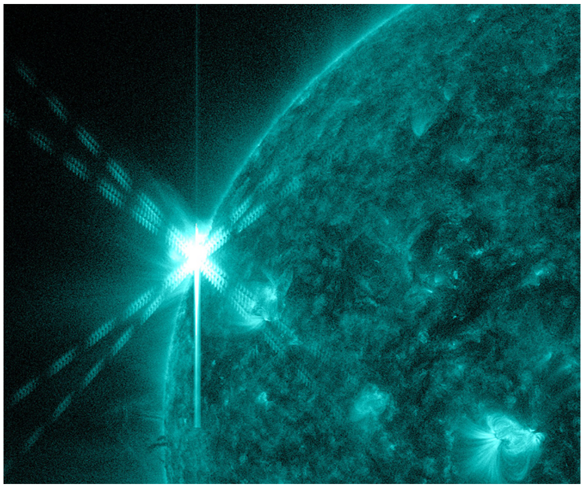

Figure 1.4. An M5.6 class solar flare from an active region on August 17, 2012 that captured by the Solar Dynamics Observatory (SDO) in EUV light at 131 Angstroms (Courtesy of NASA/SDO).

1.1.3 Solar Flare and Coronal Mass Ejection

A solar flare is transient, localized, explosive release of energy producing enhanced emissions which cover the entire radiative spectrum. It appears as a sudden, short-lived brightening of an area in the chromosphere [37] Solar flares release their energy mainly in the form of electromagnetic radiation and energetic particles. Flares are classified as A, B, C, M, or X according to the maximum flux of soft X-ray in the 0.1 - 0.8 nm range of the spectrum measured near the Earth [32]. Figure 1.4 depicts an M7.9 class solar flare on March 13, 2012 that captured by the Solar Dynamics

Observatory (SDO). While C-class flares are a common occurrence during years near solar maximum, the frequency of X-class flares during solar maximum is approximately two per month (http://spacemath.gsfc.nasa.gov). There is a large spectral difference between flares in magnitude [133]. The enhancement of the Extreme Ultraviolet (EUV) spectral irradiance depends on the location of a flare, while flare enhancement of soft X-ray (XUV) depends weakly on the location [88].

The solar UV photons are the primary energy sources of the neutral and ionized constituents of the Thermosphere-Ionosphere (T-I) system [70, 60]. The extra ionization in the ionosphere caused by flares increases electron density, which influences the absorption and refraction of radio waves propagating through the ionosphere from one station to another [126]. Also, flares are often associated with other solar activities, such as Coronal Mass Ejection (CME), which may cause significant geomagnetic storms [69, 4]. A CME is a transient ejection of large amount of materials. Magnetic reconnection is considered to be responsible for CME events. Magnetic reconnection is the physical process when two oppositely directed magnetic field lines merge and the magnetic topology is rearranged. Most CME events originate in closed magnetic field regions, where the plasma is constrained by the strong magnetic fields from expanding outward. During the magnetic reconnection process, closed field lines open and reform, which converts the magnetic energy into kinetic and thermal energy. CMEs are not generated by solar flares. Flares and coronal mass ejections are different aspects of solar activity that are not necessarily related. Flares are essentially photon output, whereas CMES mainly produce plasma. Both of CMEs and flares are important sources of dynamical phenomena in the space environment.

1.2 Solar Wind and Interplanetary Magnetic Field

The solar wind is quasi-neutral, fully ionized plasma which is ejected from the solar corona into the interplanetary space [45, 51]. The solar wind results from the huge pressure difference between the hot plasma at the base of the corona and the interstellar medium. The existence of continuous solar wind streams was first suggested by Ludwig Biermann [6] based on his studies of the acceleration of plasma structures in comet tails, and the detailed mathematical theory of solar wind was put forward by Eugene Parker [79, 80]. The solar wind starting subsonically at the base of the corona accelerates to supersonic speeds. At 1 Astronomical Unit (AU, the mean distance between the Sun and the Earth), the solar wind has an average density of $\sim$5 cm^{-3} and an average flow speed of 450 km/s. The mean travel time of solar wind from the Sun to the Earth is 3.5×10^5 seconds ($\sim$4 days). The solar magnetic fields frozen into the solar wind are transported into space with the solar wind and are known as the interplanetary magnetic field (IMF). The IMF at 1 AU has an average magnetic field of 7.0 nT [37].

Near solar minimum including the declining phase of the solar cycle, large, long-lived coronal holes extend from the polar regions to low heliographic latitudes. Near solar maximum, the coronal holes are mainly restricted to the polar regions of the Sun. The high-speed streams originate in coronal holes and typically exceed 600 km/s at 1 AU, while the speed of slow streams is usually less than 350 km/s [67]. When the high-speed streams catch up with slower streams, a high-pressure region is produced at the leading edge of the high-speed streams due to the plasma compression. This region is called the corotating interaction region (CIR), which is associated with recurring geomagnetic disturbances [45].

1.3 Terrestrial Magnetosphere

1.3.1 Structure

The magnetosphere is formed as a result of the interaction of the supersonic solar wind with the intrinsic magnetic field of the Earth [51]. The Earth's intrinsic magnetic fields, the solar wind and IMF at 1 AU determine the shape of the magnetosphere. The magnetosphere extends from the bottom of the ionosphere to more than ten Earth radii in the sunward direction and to several hundred Earth radii in the anti-sunward direction [112]. The solar wind slows down from supersonic flow to subsonic flow due to the bow shock at about 13 Earth radii. The solar wind can not penetrate the magnetopause and is deflected around the magnetosphere. The thermal pressure of the solar wind and magnetic pressure of the Earth's dipole field are balanced at the magnetopause. For average solar wind conditions, the standoff distance of the magnetopause is about 10 Earth radii [51, 37]. The magnetosheath between the bow shock and magnetopause is filled with shocked solar wind plasma. On the nightside, the magnetic field lines of the Earth are stretched along the direction of solar wind, and forms a cylindrical-shaped region known as the magnetotail. The polar cusps are located at the interface of closed and open magnetic field lines of the Earth. The magnetosheath plasma can extend deep into the atmosphere at the cusps [137]. Figure 1.5 illustrates the regions of the magnetosphere described in this section.

1.3.2 Geomagnetic Storms

Geomagnetic storms are large, prolonged, global disturbances of the magnetosphere caused by the variations in the solar wind and IMF. When the IMF has a significant southward component, magnetic reconnection occur at the dayside magnetopause. This increases the penetration of the solar wind electric field into Earth's magnetosphere, and also increases the magnetospheric convection [37]. The extended

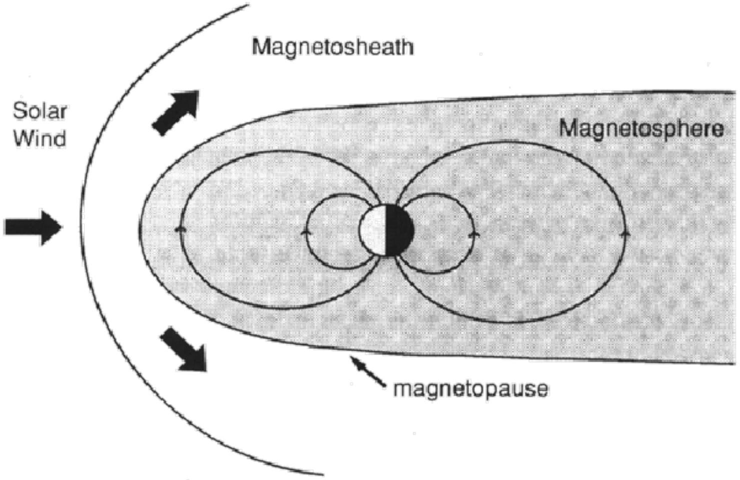

Figure 1.5. Schematic of Earth's bow shock, magnetosheath and magnetopause [15].

period with southward IMF is called the main phase of a storm, which typically lasts for several hours. As the southward component of IMF decreases, the magnetic reconnection weakens. This is called the recovery phase of a storm, which typically takes several days.

Geomagnetic activity indices are widely used to characterize the dynamic state of various aspects of the magnetosphere-ionosphere system. Geomagnetic indices are based on the ground magnetometers that record the temporal variation of magnetic field vector [37]. The fluctuations of horizontal magnetic component at a given observatory are measured during a three-hour interval and represented by the K index. The K value is an integer ranging from 0 to 9, with the strongest magnetic activity denoted by 9. By calculating a weighted average of K index of a network of high-latitude stations between geomagnetic latitudes from 48 to 63 degrees, *J.Bartels* introduced the K_p index in 1949, which is sensitive to auroral zone activity. The hourly D_{st} index is a measure of the current strength, and is calculated by taking the average of the adjusted residuals of the horizontal component of the magnetic field vector measured by low magnetic latitude observatories [51].

1.4 Terrestrial Upper Atmosphere

The upper atmosphere is the overlapped thermosphere-ionosphere region above 100 km. The thermosphere and ionosphere are tightly coupled through plasma-neutral interaction.

1.4.1 Thermosphere

The Earth's atmosphere is divided into different layers according to the vertical temperature structure. As shown in Figure 1.6, the lowest layer is the troposphere that extends from the surface to about 12 km. In the troposphere, the temperature decreases with altitude since most of the solar visible radiation is absorbed at the surface. Above the troposphere, the temperature increases due to the absorption of solar UV radiation by ozone layer. This layer is called the stratosphere and ranges from the top of the troposphere to about 50 km. Above the stratosphere lies the mesosphere which extends from 50 km to 90 km. In the mesosphere, the temperature decreases again with altitude due to the infrared cooling by carbon dioxide, and it is the coldest region at the top of the mesosphere in the Earth's atmosphere ($\sim$180 K). The thermosphere is the layer above the mesosphere where the temperature increases dramatically due to the efficient absorption of solar UV radiation. The thermospheric temperature becomes nearly constant above $\sim$300 km.

The thermosphere are mainly composed of O, O_2 and N_2, which are diffusively separated according to the molecular weights. The thermospheric composition is determined by the combined contributions from diffusion, wind and chemical reactions. Density and composition vary significantly with latitude and longitude, as well as time. The vertical transportation due to molecular diffusion tends to separate the atmospheric constituents according to their mass, while the turbulence (eddy mixing) mixes the atmospheric constituents. At lower altitudes below 100 km, the eddy

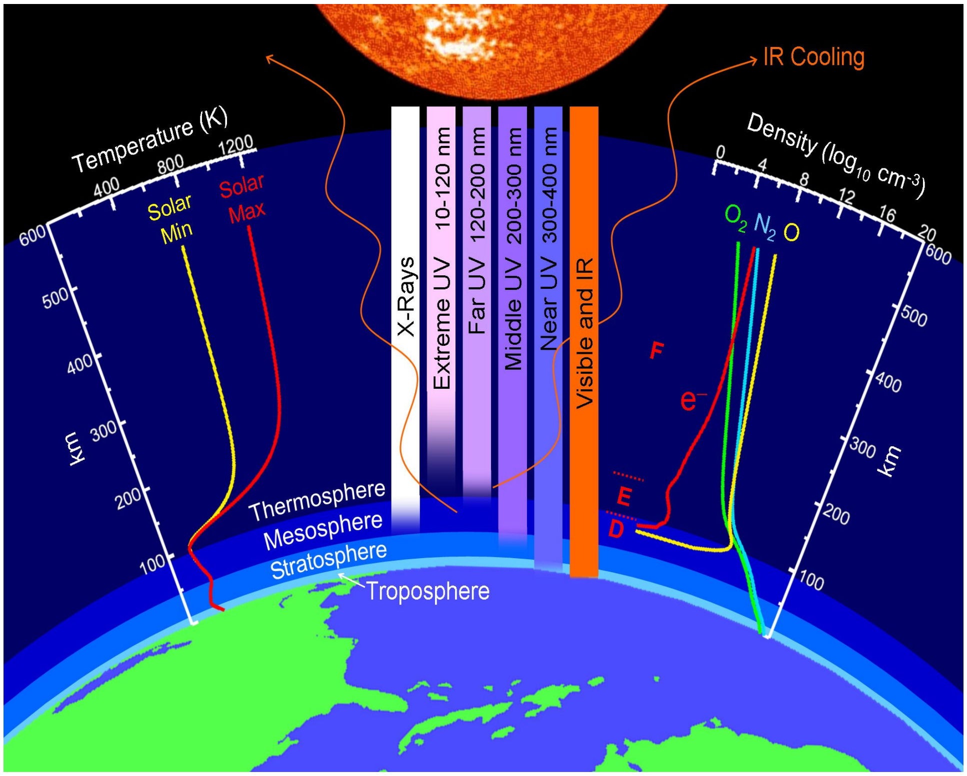

Figure 1.6. Typical profiles of neutral density and temperature with various layers of the upper atmosphere (Courtesy of NASA,$http://www.nasa.gov$).

mixing dominates and the region is called the homosphere, while at higher altitudes above 125 km, molecular diffusion prevails and the region is called the heterosphere [111].

The temporal variation of thermospheric neutral density has a scale from hours to decades because of the variations of solar irradiance, geomagnetic activity and lower atmospheric processes while the [84]. The neutral density is mainly modulated by the changes of EUV heating, such as solar flare events, diurnal variations, solar rotation (27 days) and solar cycle (11 years) [87]. It has been showed that the neutral density can increase by 20% in a few hours responding to a large flare from the measurements of Challenging Minisatellite Payload (CHAMP) satellite [123] and simulation results [118]. The diurnal variation of density is about 100% [86]. Solar rotation modulation

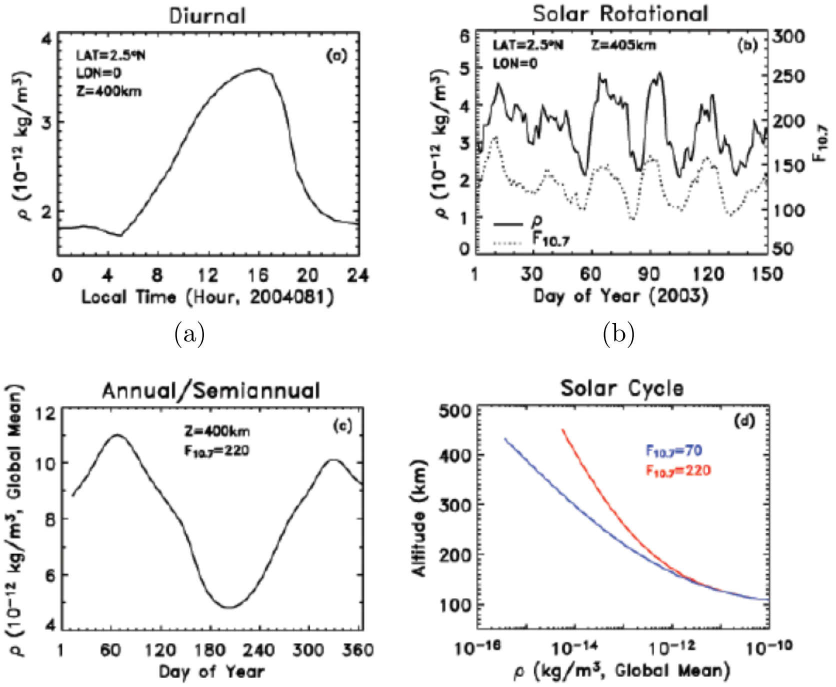

(a) (b)

(c) (d)

Figure 1.7. Neutral density variations of TIE-GCM simulations. (a) diurnal. (b) solar-rotational. (c) annual/semiannual. (d) solar-cycle [84].

of the thermospheric density varies from 10% for low solar activity to one order of magnitude for strong solar activity [56]. The solar cycle variation of neutral density is about one order of magnitude [30]. Figure 1.7 depicts the different types of neutral density variations due to solar EUV simulated by TIE-GCM in [84].

1.4.2 Ionosphere

Absorption of the solar EUV and X-ray irradiance ionizes the thermospheric constituents and creates the ionosphere, which extends from about 60 km to 1000 km. The ionosphere divided into different regions according to the vertical profile of the electron density. Figure 1.8 shows the ionospheric regions for both solar minimum and maximum conditions. The D-region (60 - 90 km) is characterized by low electron density. On top of the D-region is the E-region (90 - 140 km), which peaks around 110 km. The F-region (140 - 1000 km) can be further divided into F_1 and F_2 regions. The electron density in F_2 region is determined by both the chemical and diffusive processes, which peaks around 300 km. The D and F_1 regions disappear at night. The variation of ionosphere has a strong solar cycle dependence since the main source of ionization and energy is photoionization. Therefore, the electron variation is determined by the changes in solar zenith angle and solar EUV and X-ray fluxes [111].

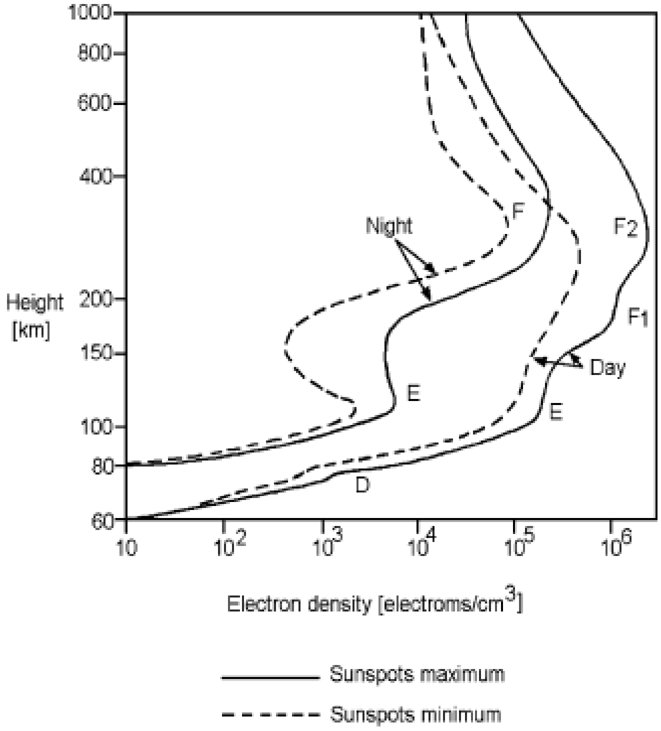

Figure 1.8. Typical vertical profile of electron density in the mid-latitude ionosphere [38].

As shown in Figure 1.9, the thermosphere-ionosphere system changes dramatically because of the significant variation of solar energy. Solar energy reaches the

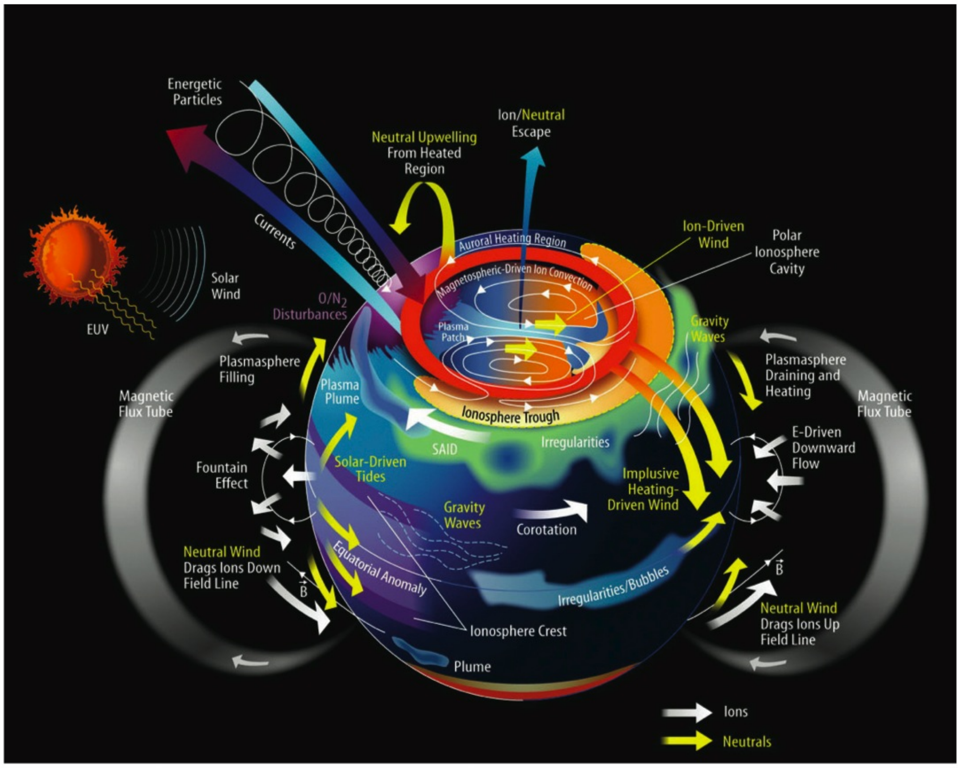

Figure 1.9. The prominent features in the ionosphere-thermosphere system and their coupling to the different energy inputs (Courtesy of NASA).

Earth mainly as electromagnetic irradiation and the solar wind. The energy of solar wind is dissipated into Earth's upper atmosphere through Joule heating and particle precipitation. The waves propagated from the lower atmosphere also bring energy and momentum into the upper atmosphere.

Solar irradiance is the primary energy input to the thermosphere-ionosphere system, and the EUV heating determines the mean thermal and composition structure of the thermosphere. The solar photons with wavelength shorter than 102.5 nm are absorbed by the major constituents (N_2, O_2 and O) through photoionization and photodissociation. The local absorption rate depends on the product of the absorption cross-sections and the total abundance of the absorbing species along the path. The

$F_{10.7}$ index is the radio flux from the Sun at a wavelength of 10.7 centimeter, and is most widely used as a proxy for solar irradiance.

The energy of solar wind is deposited into the Geospace from magnetosphere to the thermosphere-ionosphere system through plasma convection and energetic particle precipitation in the high latitudes. The ionosphere and magnetosphere are coupled through the current system and magnetospheric particle precipitation in the auroral region. The ionospheric currents heat the thermosphere through ion-neutral collisions, while the energetic particles heat the thermosphere through ionization, excitation and dissociation of the neutral species. Due to the interaction between the solar wind and Earth's magnetic fields, the magnetospheric electric fields and currents are generated. The magnetospheric currents flow into the ionosphere along the magnetic field lines and form a closed magnetosphere-ionosphere current system, which drives the convection of charged particles in the ionosphere. When the IMF is southward, the interplanetary electric field is mapped along the magnetic field lines to the ionosphere and generates an ionospheric polar cap electric field in the dawn to dusk direction [65]. A typical 2-cell plasma flow pattern is generated with anti-sunward flow over the polar cap and return flow equator-ward of the auroral oval, as shown in Figure 1.10 [47]. The potential difference of this mapped field is called the cross polar cap potential (CPCP). Consequently, the enhanced convection heats the thermosphere through collisions between charged particles and neutral atmosphere, which is called Joule heating. The energetic particles precipitating into the upper atmosphere at high latitudes also heat the thermosphere-ionosphere system. Precipitating electrons and ions excite the atmospheric species through dissipating the energy of magnetospheric particles. The following radiation of photons, which is mainly the emissions from nitrogen and oxygen atoms and molecules, is known as the aurora. The hemispheric power (HP) is used to characterize the auroral energy flux. Auroras occur primarily at high geomagnetic latitudes, where magnetospheric particles can access the upper atmosphere along the magnetic filed lines. The distribution of auroras has an oval shape. The position and size of the auroral oval depends on the geomagnetic activity. The aurora zone expends to the lower latitudes when geomagnetic storms occur [37]. The Geomagnetic energy inputs to the upper atmosphere, including both Joule heating and particle precipitation are the most variable, and can exceed the solar irradiance energy in geomagnetic storms.

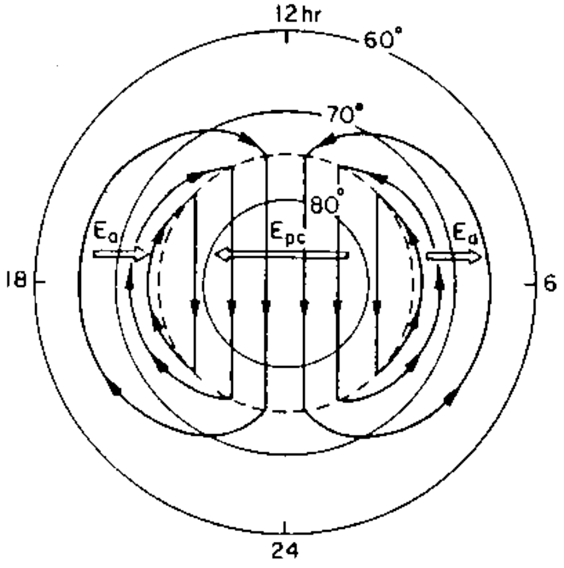

Figure 1.10. High-latitude electric fields and associated plasma drift in the northern hemisphere in the case of southward IMF [47].

Energy can also be transferred from the lower atmosphere by tides and gravity waves propagating upward. Gravity waves arise due to the buoyancy forces in the atmosphere. It can be generated in the stratosphere and mesosphere by perturbations in the flow of air over mountains, thunderstorms, volcanos and earthquakes [111]. Gravity waves carry large vertical fluxes of energy and momentum, and also propagate rapidly in the vertical direction. When the waves break, they deposit energy and momentum into the upper atmosphere. Tides are the special gravity waves with particular horizontal scales and specific periods [37]. Tides are generated primarily by the solar or lunar influences and have long wavelengths and low frequencies. The diurnal tides with 24-hour period and wavelength equal to the Earth's circumference dominate above 250 km, while the semi-diurnal tides with 12-hour period and wavelength equal to one half of the Earth's circumference dominate in the lower atmosphere [11]. The amplitude of tide grows as the wave propagates toward higher altitudes and eventually, the tide breaks forming gravity waves [111]. This part of energy from lower atmosphere is comparably small, and we focused on the solar irradiance and geomagnetic energy in this dissertation.

1.5 Dissertation Objective

The primary objective of this dissertation is to investigate the external forcing of thermosphere - ionosphere system and its impact on the thermospheric variations, such as neutral density and temperature. The neutral density is important for both the research and the satellite operation communities. We will focus on the wavelength dependence of solar irradiance enhancement during flares, the geomagnetic energy inputs associated with high-speed solar wind streams, the height distribution of Joule heating under different solar conditions and the variations of energy inputs to the upper atmosphere during last solar cycle.

In this chapter, a general description of the solar - terrestrial physics has been provided. Chapter 2 describes the models and data that used in this study. In chapter 3-6, a detailed investigation of the energy inputs and their impacts on the upper atmosphere are given. Chapter 7 concludes the main results.

CHAPTER 2

MODELS AND DATA

2.1 OMNI 2 data

The OMNI data set was first created at the National Space Science Data Center (NSSDC) in the mid-1970's. OMNI 2 was created in 2003 as a successor and maintained by NSSDC. The OMNI 2 data set is a multi-source data set now covering the period from November, 1963. The data are from a variety of satellites including IMP (Interplanetary Monitoring Platform), WIND, Advanced Composition Explorer (ACE) and GEOTAIL. OMNI 2 data provide the near-Earth (propagated to the bow-shock nose) interplanetary magnetic field (IMF), solar wind parameters, energetic particle data, solar and geomagnetic activity indices [50] and are widely used in the space science community. The OMNI 2 data were obtained from the GSFC/SPDF OMNIWeb interface at http://omniweb.gsfc.nasa.gov.

2.2 CHAMP data

The CHAllenging Mini-Satellite Payload (CHAMP) is depicted in Figure 2.1. The objections of CHAMP are to resolve the long-term temporal variations primarily in the gravity field, in the magnetic field and within Earth's atmosphere. The CHAMP satellite was launched in July 2000 at 450 km altitude. Its orbit is near-circular with an inclination of 87.3° and an period of 94 minutes. Standard methods are used to obtain the thermospheric mass densities from pole to pole, from accelerometer measurements [125]. The NRLMSISE00 empirical model is used to normalize the measured densities at satellite altitudes to a constant altitude of 400 km [82]. In this study, the thermospheric mass density around 400 km from the CHAMP satellite is utilized.

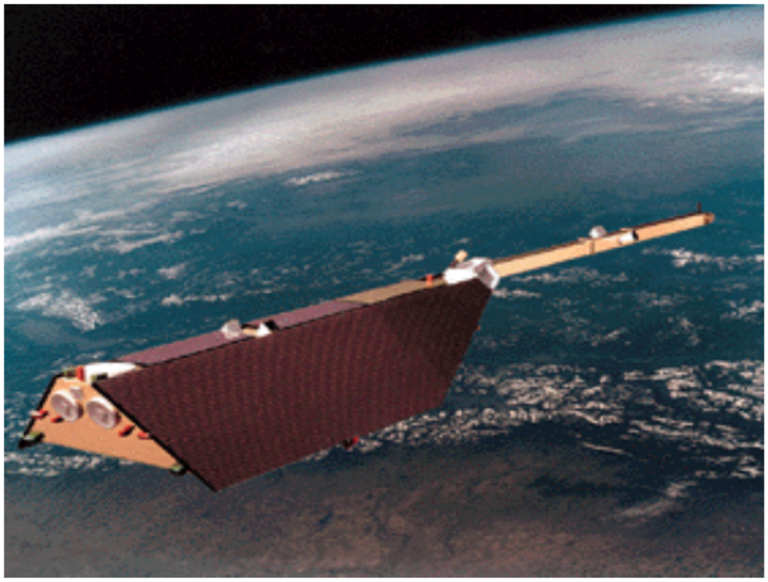

Figure 2.1. The CHAMP Satellite (Courtesy of GFZ German Research Centre for Geosciences).

2.3 DMSP data

The Defense Meteorological Satellite Program (DMSP) satellites have 101-minute, sun-synchronous, near-polar orbits at 830 km altitude above the surface of the Earth as depicted in Figure 2.2. The sensors onboard record plasma densities, cross-track and along-track ion velocities, and composition. In this study, we only use the convection data measured by Special Sensor Ionospheric Plasma Drift/Scintillation (SSIES) thermal plasma analysis package on two satellites: F13 and F15. F13 is in a roughly dawn-dusk orientation while F15 is in a 0930-2130 local time orientation.

The potential drop measured by F13 and convection data by both F13 and F15 are collected from DMSP SSIES database for the whole year of 2005. The potential drop is the difference between the maximum potential and minimum potential measured along the track of F13 through the potential distribution, and is not the same as the true CPCP, but always lower than the true CPCP. In this paper, the potential drop measured from DMSP is denoted as the CPCP from DMSP.

Figure 2.2. The DMSP Satellite (Courtesy of USAF Research Laboratory).

Every four-second set of data has two quality flags marked as good (flag=1), caution (flag=2), poor (flag=3), or undetermined (flag=4) to provide the reliability. In this study, we just use the SSIES data with quality flag 1 or 2. In addition to the quality of each single data point, the quality of the trajectory has also been considered by the offset, which is the difference between the final potential at the stopping endpoint and zero. The pass is ignored where the offset magnitude exceeds 50% of the CPCP calculated along that pass in this study.

2.4 Flare Irradiance Spectral Model (FISM)

FISM is an empirical model of the solar irradiance spectrum from 0.1 to 190 nm at 1nm resolution and on 1-minute time cadence [10]. The high temporal resolution of FISM makes it possible to study the variations due to solar flares. This model is based on the data provided by the Solar Extreme ultraviolet Experiment (SEE) [146] on the Thermosphere Ionosphere Mesosphere Energetic and Dynamics (TIMED) satellite and the SOLar STellar Irradiance Comparison Experiment (SOLSTICE) [108] on the Solar Radiation and Climate Experiment (SORCE).

FISM estimates the daily component of irradiance including the variations from the solar cycle and solar rotation of active regions. The flare component of FISM includes both the impulsive and gradual phase variations, and is based on a reference set of 39 large flares from 2002 to 2005 measured by SEE and SORCE [10]. This reference set of measurements is fit to the flare proxy to determine the coefficients. The Geostationary Operational Environmental Satellites (GOES) 0.1 - 0.8 nm fluxes are used as the flare proxy to empirically model the flare variation for FISM, because of its high temporal resolution and reliable data since 1970 with few data gap, as well as plans for continued future measurements. A linear relation is found between the irradiance of GOES 0.1 - 0.8 nm and the irradiance for the soft X-rays at wavelengths less than 14 nm, while a power law relation with exponent of 0.647 is found between the irradiance of GOES 0.1 - 0.8 nm and the irradiance for EUV at wavelengths larger than 14 nm [10].

Due to large variations during flares for different wavelengths and lack of measurements, the FISM flare uncertainty has wavelength dependence and varies from 10% to above 100%. However, compared to models with only daily outputs, FISM improves the estimation of solar flares significantly. More flare data can help reduce the FISM flare uncertainties. The newly available and more accurate data from the Extreme ultraviolet Variability Experiment (EVE) on the Solar Dynamics Observatory (SDO) [148, 147] will add the additional variable of temporal delays in some of the EUV emissions during the gradual phase of flares [8].

2.5 Weimer05 model

Weimer05 [141] is an empirical model of high-latitude electrodynamics, providing the electric potential, magnetic potential, field-aligned currents and Poynting flux. The inputs include the solar wind plasma number density, speed, the transverse orientation of the solar wind magnetic field B_y, B_z and the Earths dipole tilt angle. It is derived from the polar-orbiting DE (Dynamics Explorer) 2 satellite measurements of the ionospheric electric and magnetic fields from ∼2900 passes, as well as simultaneous measurements of IMF from IMP (Interplanetary Monitoring Platform) 8 and ISEE (International Sun-Earth Explorer) 3 were used [138].

Data from the ∼2900 passes were divided into 32 groups according to the angle of the IMF vector in the Geocentric Solar Magnetospheric System (GSM) Y-Z plane and its magnitude to obtain plasma convection patterns for different orientations of the IMF. Figure 2.3 shows the distribution of the IMF from all cases. The radial lines show the grouping of the data into eight angular bins, each 45° wide. The concentric circles show the grouping of the data according to the magnitude of IMF in this plane. There are four bins with an approximately equal number of cases in each group, with dividing lines at 3.5, 5.2, and 7.25 nT. angle. The measurements in each group are then used to derive the map of the electric potential over polar cap for the given conditions. The electric potential is described in the form:

$$\Phi(\theta,\phi)=\sum_{l=0}^{m}\sum_{m=-l}^{l}A_{lm}\sqrt{\frac{(2l+1)(l-m)!}{4\pi(l+m)!}}P_{lm}(cos\theta)e^{im\phi} \tag{2.1}$$

where P_{lm} is the associated Legendre function. The coefficients of a spherical harmonics expansion are found by least square error fits. The polar angle θ varies from 0 at the geomagnetic pole to π at the lower-latitude limit of 45°, while the azimuthal angle ϕ is derived from the magnetic local time. The coefficient variation with arbitrary solar wind conditions is calculated using a linear regression of the spherical harmonic coefficients in each IMF group [139].

As an empirical model, Weimer05 is often used to force General Circulation Models (GCMs). However, Weimer05 only represents the statistical average [66, 20]

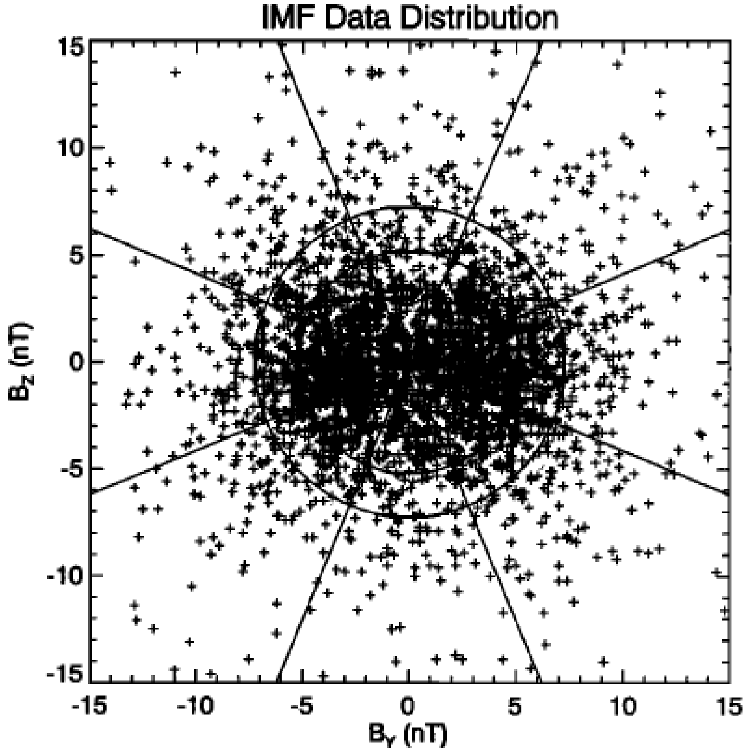

Figure 2.3. IMF data distribution. This graph shows the IMF B_y and B_z values in GSM coordinates, for each of the 2879 DE 2 passes which have IMF measurements available. The concentric circles show the dividing lines for the four qualities, each of which has an approximately equal number of cases, stored by the magnitude of the IMF in the GSM Y-Z plane. The radial lines show the division of the data according to the angle of the IMF vector in this plane. There are eight angular bins, each 45°s wide [138].

and probably underestimates the integrated Joule heating during moderate activity times, because it cannot capture sharp gradients and also due to the averaging process [139]. The integrated Joule heating during strong activity times is most likely overestimated by Weimer05 due to inaccurate saturation of the driving at high latitudes. An example of the Weimer05 is depicted in Figure 2.4.

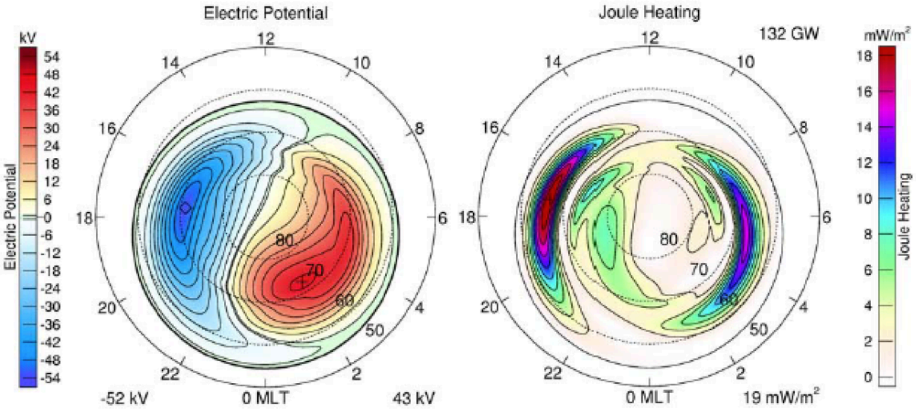

(a) (b)

Figure 2.4. Polar cap potentials and Joule heating in the Northern Hemisphere. (a) Electric potential. (b) Joule heating. [141].

2.6 AMIE model

Assimilative mapping of ionospheric electrodynamics (AMIE) is a procedure to derive the realistic, time-dependent, large-scale distribution of electromagnetic fields over the entire polar ionosphere by the synthesis of a variety of observations [97, 95,]. It is a form of optimally constrained, weighted least-squares fit of coefficients to the observations. In order to reduce the contribution of less reliable data to the fitting, each data set of observations is weighted by the inverse square of its effective error. AMIE estimates the height-integrated Pedersen and Hall conductivities using emperical auroral conductance models with modifications from actual observations. The modification is calculated through a least square fit to logarithms of the ratio of observed conductivities to empirical model values.

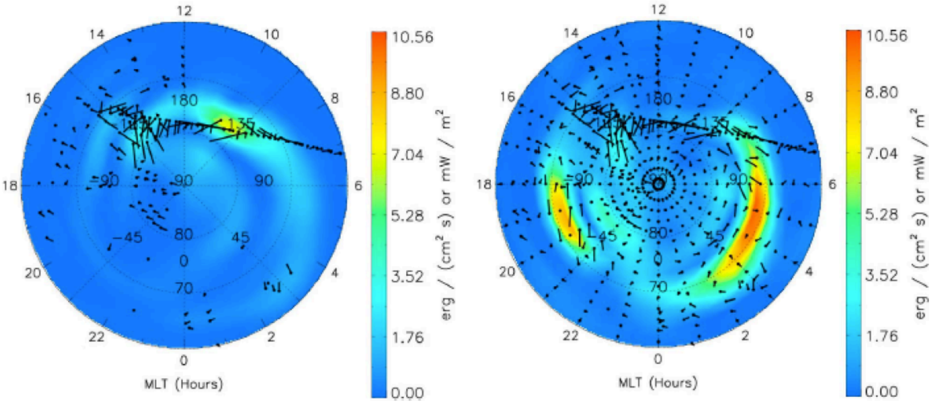

(a)

(b)

Figure 2.5. Joule heating maps calculated by AMIE on 5 April 2010 at 0:30 UT. (a) The left uses data from ground magnetometometers as well as plasma drift measurements from MDSP and SuperDARN. (b) The right pattern includes data from the Active Magnetosphere and Planetary Electrodynamics Response Experiment (AMPERE). [144].

There are many case studies for storm and substorm events by using AMIE outputs, while little effort has been made to study the Joule heating and other outputs for a long period, for instance, one year. Utilizing the background models and assimilating ground- and space-based measurements, AMIE calculates the electric potential pattern, the auroral precipitation and conductance patterns at a given time. From these, the polar cap potential, Joule heating rate and hemispheric power are derived. In this study, the [31,] model and [139,] model have been used for the empirical conductance and electric potential, respectively. AMIE can ingest data from a variety of sources including ground- and satellite-based magnetometers, incoherent scatter and high-frequency radars like those in the Super Dual Auroral Radar Network (SuperDARN), in-situ particle measuring and auroral imaging satellites like DMSP and TIMED/GUVI (Thermosphere Ionosphere Mesosphere Energy and Dynamics/Global Ultraviolet Imager). An example of Joule heating patterns from AMIE is depicted in Figure 2.5.

2.7 NCAR TIE-GCM

National Center for Atmospheric Research (NCAR) Thermosphere-Ionosphere-Electrodynamics General Circulation Model (TIE-GCM) [105] is a first-principle, three-dimensional, non-linear representation of the coupled thermosphere and ionosphere system. It solves the momentum, energy and continuity equations for neutral and ion species in pressure coordinates [107], with a self-consistent calculation of ionospheric wind dynamo effects [100]. In this study, the latest version (v1.94) of TIE-GCM is run with $5^\circ \times 5^\circ \times$ half scale height resolution (longitude × latitude × altitude).

The vertical coordinate of TIE-GCM consists of 25 pressure levels, which are defined as

$$Z = ln(\frac{P_0}{P}) \tag{2.2}$$

where P_0 is a reference pressure surface (50 μPa) at Z=0. The pressure scale height H is given by the hydrostatic equation

$$\frac{\partial Z}{\partial z} = \frac{R^* T_n}{\bar{m} g} = H \tag{2.3}$$

where z is the geopotential height, R^* is the universal gas constant, T_n is the neutral temperature, $\bar{m}$ is the mean molecular mass and g is the gravitational acceleration.

The mass mixing ratios of the major species (O, O_2 and N_2) are defined as

$$\Psi_i = n_i m_i (\sum_{j=1}^{3} n_j m_j)^{-1} \tag{2.4}$$

where Ψ_i with i = 1, 2 and 3 corresponding to the mass mixing ratios of O, O_2 and N_2, respectively. The vector of mass mixing ratios of O_2 and O is defined as

$$\vec{\Psi} = \begin{pmatrix} \Psi_{O_2} \\ \Psi_O \end{pmatrix} \tag{2.5}$$

and its coupled vector equation is given by [21] as

$$\begin{aligned} \frac{\partial}{\partial t}\vec{\Psi} = -e^Z \tau^{-1} \frac{\partial}{\partial Z}[\frac{\bar{m}}{m_{N_2}(\frac{T_{00}}{T_n})^{0.25}} \alpha^{-1} \mathbb{L}\vec{\Psi}] + e^Z \frac{\partial}{\partial Z}(K_E(Z) e^{-Z} \frac{\partial}{\partial Z}\vec{\Psi}) \\ -(\vec{v_n} \cdot \bigtriangledown \vec{\Psi} + W \frac{\partial}{\partial Z}\vec{\Psi}) + \vec{S} - \vec{R} \end{aligned} \tag{2.6}$$

where Z is the geometric height (pressure level), T_{00} is the standard temperature (273 K), m_{N_2} is the molecular mass of N_2, τ is the diffusion time scale ($1.86 \times 10^3 s$), K_E is the eddy diffusion coefficient, $\vec{v_n}$ is the horizontal neutral velocity, $W = \frac{dZ}{dt}$ is the vertical velocity, S is the effective mass source and R is the removal rate. The terms on the right hand side represent the vertical molecular diffusion, the vertical eddy diffusion, the horizontal and vertical nonlinear advection, and the chemical production and loss terms, respectively.

The N_2 mass mixing ratio is determined by

$$\Psi_3 = 1 - \Psi_1 - \Psi_2 \tag{2.7}$$

Therefore, the mean atmospheric molecular mass $\bar{m}$ is calculated as

$$\bar{m} = (\sum_{i=1}^{3} \frac{\Psi_i}{m_i})^{-1} \tag{2.8}$$

where m_i with i =1, 2 and 3 corresponding to the atomic mass of O and the molecular mass of O_2 and N_2, respectively.

By solving the continuity equation of the thermospheric neutral gas, the vertical velocity is determined as

$$\frac{1}{rcos\lambda}\frac{\partial}{\partial\lambda}(vcos\lambda)+\frac{1}{rcos\lambda}\frac{\partial u}{\partial\phi}+e^{Z}\frac{\partial}{\partial Z}(e^{-Z}W)=0 \tag{2.9}$$

The momentum equations in the zonal and meridional directions are given as

$$\begin{split}\frac{\partial u}{\partial t}=\frac{ge^{Z}}{P_0}\frac{\partial}{\partial Z}(\frac{\mu}{H}\frac{\partial u}{\partial Z})+fv+\lambda_{xx}(v_{E\times B,x}-u)+\lambda_{xy}(v_{E\times B,y}-v)\\ -\vec{v_n}\cdot\bigtriangledown u+\frac{uv}{r}tan\lambda-\frac{1}{rcos\lambda}\frac{\partial\Phi}{\partial\phi}-W\frac{\partial u}{\partial Z}-hd_u\end{split} \tag{2.10}$$

$$\begin{split}\frac{\partial v}{\partial t}=\frac{ge^{Z}}{P_0}\frac{\partial}{\partial Z}(\frac{\mu}{H}\frac{\partial v}{\partial Z})-fu+\lambda_{yy}(v_{E\times B,x}-v)+\lambda_{yx}(v_{E\times B,y}-u)\\ -\vec{v_n}\cdot\bigtriangledown v+\frac{u^2}{r}tan\lambda-\frac{1}{r}\frac{\partial\Phi}{\partial\lambda}-W\frac{\partial v}{\partial Z}-hd_v\end{split} \tag{2.11}$$

where λ, ϕ and Z are latitude, longitude and vertical coordinate. r is the radial distance from the center of the Earth, μ is the viscosity coefficient, f is the Coriolis parameter, Φ is the geopotential, and H is the pressure scale height, W is the vertical velocity, while u and v are zonal and meridional wind velocities, and λ_{xx}, λ_{xy}, λ_{yx} and λ_{yy} are components of the ion-drag coefficient tensor. The forcing terms on right hand side represent the vertical viscosity, the Coriolis force, the ion-drag force, the nonlinear horizontal advection and momentum force, the pressure gradient force, the vertical advection, and the horizontal diffusion.

The neutral temperature is obtained by solving the thermodynamic equation:

$$\begin{split}\frac{\partial T_n}{\partial t}=\frac{ge^{Z}}{P_0c_p}\frac{\partial}{\partial Z}(\frac{K_T}{H}\frac{\partial T_n}{\partial Z}+K_EH^2c_p\rho(\frac{g}{c_p}+\frac{1}{H}\frac{\partial T_n}{\partial Z}))-\vec{v_n}\cdot\bigtriangledown T_n\\ -W(\frac{\partial T_n}{\partial Z}+\frac{R^{*}T_n}{c_p\bar{m}})+\frac{Q^{exp}-e^{z}L^{exp}}{c_p}-L^{imp}\end{split} \tag{2.12}$$

where T_n is the neutral temperature, t is time, g is the gravitational acceleration, c_p is the specific heat at constant pressure, P_0 is the reference pressure, K_T is the molecular thermal conductivity, K_E is the eddy diffusion coefficient, ρ is atmospheric mass density, H is the pressure scale height, $\bar{m}$ is the mean molecular mass, W is the dimensionless vertical velocity, $\vec{v_n}$ is the horizontal neutral velocity with zonal and meridional components, and Q^{exp} and L^{exp} are the other heating and cooling terms. The first term on the right side is the heat transfer by vertical molecular heat conduction and adiabatic heating or cooling due to eddy diffusion. The second term is the heat transfer due to horizontal advection, and the third term is the adiabatic heating and cooling caused by the vertical winds [75].

The neutral gas heating rate Q consists of ten processes: (1) absorption of solar UV radiation in the O_2 Schumann-Runge continuum, (2) likewise in the Schumann-Runge bands, (3) heating by neutral-neutral chemical reactions, (4) heating by ion-neutral chemical reactions, (5) heating by collisions between ambient electrons, ions and neutrals, (6) quenching of $O(^1D)$ by N_2 and O_2, (7) atomic oxygen recombination, (8) absorption of solar UV energy in the O_3 Hartley bands, (9) absorption of solar $Lyman - \alpha$ radiation, (10) heating by fast photoelectrons [106]. The main cooling processes are: (1) molecular heat conduction, (2) eddy heat conduction, (3) nonlocal thermodynamic equilibrium NO 5.3μm cooling, (4) 63μm cooling from the fine structure of atomic oxygen, and (5) nonlocal thermodynamic equilibrium CO_2 15μm cooling in the lower thermosphere [75].

The contiunity equation of ionospheric electron is

$$\frac{\partial n_e}{\partial t} = - \bigtriangledown \cdot (n_e \vec{V_e}) + P - L \tag{2.13}$$

where n_e is the electron density, $\vec{V_e}$ is the bulk flow velocity of the electron gas, t is the time, P and L are the production and loss rates of the electrons, respectively.

The bulk velocity is given in the following form

$$\vec{V_e} = \vec{V_\perp} + \vec{V_\parallel} \tag{2.14}$$

$$\vec{V_\perp} = \frac{1}{\mid B \mid} \vec{E} \times \vec{b} \tag{2.15}$$

$$\vec{V_{\parallel}} = (\vec{b} \cdot \frac{1}{v_{pn}}(\vec{g} - \frac{1}{\rho_i} \bigtriangledown (P_i + P_e)) + \vec{b} \cdot \vec{v_n}) \cdot \vec{b} \tag{2.16}$$

where $\vec{V_{\perp}}$ and $\vec{V_{\parallel}}$ are the velocity perpendicular and parallel to the magnetic field lines, respectively, and $\vec{b}$ is a unit vector along the magnetic field, v_{pn} is the plasma-neutral collision frequency, $\vec{g}$ is the gravity acceleration, ρ_i, P_i and P_e are ion mass, ion and electron pressures respectively, $\vec{v_n}$ is the neutral wind velocity, $\vec{E}$ is the ionospheric electric field, and $\mid B \mid$ is the magnitude of the magnetic field [75].

The energy equation for electrons without chemical and viscous heating is

$$\frac{3}{2}n_e k \frac{\partial T_e}{\partial t} = -n_e k T_e \bigtriangledown \cdot \vec{V_e} - \frac{3}{2} n_e k \vec{V_e} \cdot \bigtriangledown T_e - \bigtriangledown \cdot \vec{q_e} + \sum Q_e - \sum L_e \tag{2.17}$$

where k is the Boltzmann constant, $\vec{q_e}$ is the electron heat flow vector, and $\sum Q_e$ and $\sum L_e$ are the sum of all the local electron heating and cooling rates, respectively.

The external forcing of TIE-GCM are mainly the solar irradiance, magnetospheric energy, and tidal perturbations at the lower boundary of the model. Magnetospheric energy inputs include auroral particle precipitation and high-latitude ion convection. The TIE-GCM uses the solar proxy models as the default solar input. The EUV flux model for Aeronomic Calculations (EUVAC) [92] is used in the spectral range between 5 and 105 nm. It is an empirical representation of solar irradiance including a reference spectrum at solar minimum and a wavelength-dependent solar variability. The variability is parameterized by solar indices, most usually $F_{10.7}$ index. The Woods and Rottman model [149] is used for the spetral range from 105 nm to 175 nm, based on measurements from UARS/SOLSTICE and a 1994 rocket. The Hinteregger model [42] is used for the wavelength range from 1.8 to 5 nm, while for the spectra shortward of 1.8 nm is based on the Geostationary Satellite system (GOES) X-ray measurements and early XUV measurements as described by [116].

The magnetospheric energy inputs includes Joule heating and auroral particle precipitation. The particle precipitation is usually calculated through empirical formula using geomagnetic indices, whereas Joule heating rate per unit mass Q_J is given as

$$\begin{aligned} Q_J &= \frac{\vec{J_\perp} \cdot (\vec{E} + \vec{v_n} \times \vec{B})}{\rho} \\ &= \frac{\sigma_P(\vec{E} + \vec{v_n} \times \vec{B})^2}{\rho} \\ &= \lambda_1(\vec{v}_{E\times B} - \vec{v}_{n\perp})^2 \end{aligned} \tag{2.18}$$

where v_n is the neutral wind velocity, $\vec{v}_{n\perp}$ is the component of $\vec{v_n}$ perpendicular to the geomagnetic field, σ_P is the Perdersen coonductivity, ρ is the atmospheric mass density, $\vec{v}_{E\times B}$ is the electrodynamic drift velocity, and λ_1 is the Perdersen ion drag coefficient. We assume that the whole Joule heating will go into the neutral heating eventually. In this study, the Heelis potential model [41] is used to specify the high-latitude electric field while the auroral particle precipitation is described as [103].

CHAPTER 3

WAVELENGTH DEPENDENCE OF SOLAR IRRADIANCE ENHANCEMENT DURING FLARES AND ITS INFLUENCE ON THE UPPER ATMOSPHERE

3.1 Introduction

A solar flare is a sudden, intense release of magnetic energy in the atmosphere of the Sun, which produces rapid increases in electromagnetic radiation from gamma rays to radio wavelengths [126]. Flares are classified as A, B, C, M, or X according to the maximum flux of soft X-ray in the 0.1 - 0.8 nm range of the spectrum measured near the Earth [32]. While C-class flares are a common occurrence during years near solar maximum, the frequency of X-class flares during solar maximum is approximately two per month (http://spacemath.gsfc.nasa.gov). There is a large spectral difference between flares in magnitude [133]. The enhancement of the Extreme Ultraviolet (EUV) spectral irradiance depends on the location of a flare, while flare enhancement of soft X-ray (XUV) depends weakly on the location [88].

The solar UV photons are the primary energy source of the neutral and ionized constituents of the Thermosphere-Ionosphere (T-I) system [70, 60]. The extra ionization in the ionosphere caused by flares increases electron density, which influences the absorption and refraction of radio waves propagating through the ionosphere from one station to another [126]. Also, flares are often associated with Coronal Mass Ejection (CME), which may cause significant geomagnetic storms [69, 4]. Previous studies have shown that the impacts of flares to T-I system varies because the flares have different magnitudes, locations on the solar disk, rise rates and decay rates [135, 124, 88, 85, 151]. Since the XUV dominates ionization in the lower thermosphere ($< 150\ km$), and EUV dominates in the upper thermosphere [85], the impact of solar flares on the upper atmosphere also depends on the variations in different wavelengths.

The purpose of this paper is to investigate how different wavebands of solar irradiance are enhanced during flares and how the different wavebands impact the global thermosphere. The Flare Irradiance Spectral Model (FISM) [9, 10] is employed to estimate the spectra of solar irradiance. The National Center for Atmospheric Research (NCAR) Thermosphere-Ionosphere-Electrodynamics General Circulation Model (TIE-GCM) [107, 100] driven by the FISM has been used to simulate the thermospheric and ionospheric responses to flares.

3.2 Methodolody

3.2.1 Flare Irradiance Spectral Model (FISM)

FISM estimates the daily component of irradiance including the variations from the solar cycle and solar rotation of active regions. The flare component of FISM includes both the impulsive and gradual phase variations, and is based on a reference set of 39 large flares from 2002 to 2005 measured by SEE and SORCE [10]. This reference set of measurements is fit to the flare proxy to determine the coefficients. The Geostationary Operational Environmental Satellites (GOES) 0.1 - 0.8 nm fluxes are used as the flare proxy to empirically model the flare variation for FISM, because of its high temporal resolution and reliable data since 1970 with few data gap, as well as plans for continued future measurements. A linear relation is found between the irradiance of GOES 0.1 - 0.8 nm and the irradiance for the soft X-rays at wavelengths less than 14 nm, while a power law relation with exponent of 0.647 is found between the irradiance of GOES 0.1 - 0.8 nm and the irradiance for EUV at wavelengths larger than 14 nm [10].

Due to large variations during flares for different wavelengths and lack of measurements, the FISM flare uncertainty has wavelength dependence and varies from 10% to above 100%. However, compared to models with only daily outputs, FISM improves the estimation of solar flares significantly. More flare data can help reduce the FISM flare uncertainties. The newly available and more accurate data from the Extreme ultraviolet Variability Experiment (EVE) on the Solar Dynamics Observatory (SDO) [148, 147] will add the additional variable of temporal delays in some of the EUV emissions during the gradual phase of flares [8].

3.2.2 NCAR TIE-GCM

Solar irradiance spectra estimated by FISM are used as solar input to TIE-GCM in our study. The spectral range required by TIE-GCM is 0.05 - 175 nm. A low-resolution binning scheme developed in [116] is utilized to refine the FISM spectrum into 37 bins for the solar EUV energy deposition calculation. The wavelength from 0.05 - 105 nm is divided into 22 non-uniform bins in the low-resolution binning scheme according to the changes of cross sections and photon energy within a bin. The spectrum with wavelength longer than 105 nm is divided evenly into 5-nm resolution bins except for $Lyman-\alpha$ line (121.56 nm) [84].

The contributions to the neutral heating caused by solar irradiance absorption include the EUV, the Schumann-Runge bands and continuum in TIE-GCM. The heating due to irradiance from 0.05 to 105 nm is calculated through integrating heating over the first 22 bins as shown by [137] in equation (1), which depends on the solar flux at different wavelengths, the ionization cross sections of N_2, O_2, and O, and the column number densities of N_2, O_2, and O. The heating efficiency ϵ is equal to 0.05

[120], which is due to the fact that the EUV heating of the neutral gas only accounts for approximately 5% of the total photon energy absorption. The contribution of Schumann-Runge continuum is integrated over the left 15 bins with the excess energy from O_2 and $O(^1D)$ product. The neutral gas heating by Schumann-Runge bands is specified by the empirical formula in [121], with a heating efficiency of about 0.3.

3.3 Results and discussion

3.3.1 Solar irradiance enhancements from FISM for X-class flares

Figure 3.1 depicts the FISM outputs for a X17.2 flare on October 28th, 2003 (day of year 301). The top panel shows the temporal variation of total solar flux integrated for 0 - 190 nm wavelength, which started to increase at 11:00 UT and reached maximum flux 100 mW/m^2 at around 11:10 UT. The wavelength dependences of solar flux before flare and at flare peak are shown in the middle panel. The black line is for the pre-flare time which is marked with a triangle in the top panel, while the red line is for the time at flare peak which is marked with a diamond in the top panel. The flux enhancement varied with the wavelength, which is also illustrated in the bottom panel, the percentage increase of solar flux at the flare peak compared to the pre-flare condition. The solar irradiance increased largest in the 0 - 14 nm range, about 1000% on average, and increased about 100% in 25 - 105 nm range for this flare.

To have a better understanding of the wavelength dependence of the percentage increase of X-class flares, we examined the spectra of solar irradiance percentage increase during 61 X-class flares between year 1989 and 2012 using FISM. A flare is classified as A, B, C, M or X according to the peak flux of 0.1 - 0.8 nm irradiance near Earth. Within each class, a linear scale from 1.0 to 9.9 is used to specify the

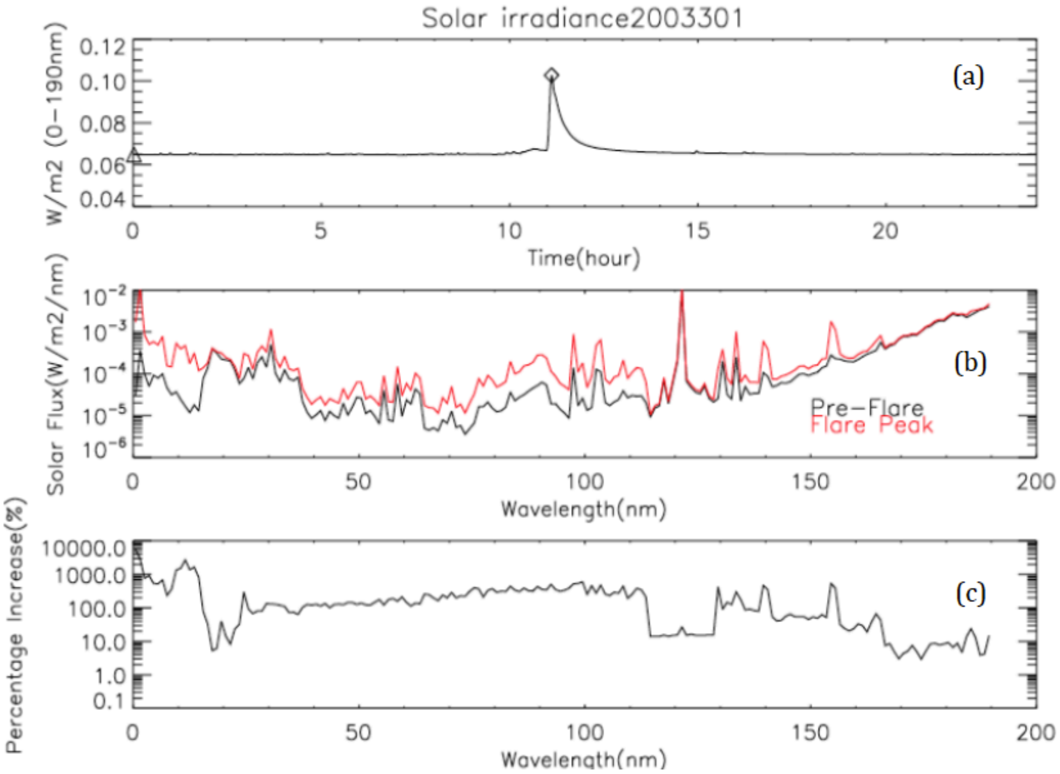

Figure 3.1. FISM solar irradiance results for X17.2 flare on October 28^{th}, 2003 (day of year 301). (a) Time variation of total solar irradiance integrated over wavelength from 0 to 190 nm. The flare reached maximum flux 0.1 W/m^2 at around 11:10 UT. (b) Solar spectra before flare at the moment denoted by triangle in top panel (black) and at flare peak denoted by diamond (red). (c) Percentage increase of solar irradiance comparing the peak and pre-flare conditions.

magnitude of a flare, except for X-class flares, the class number can exceed 9.9. The biggest flare ever recorded is an X28 flare occurred on November 4, 2003. The class numbers of 61X-class flares and their temporal distribution are depicted in Figure 3.2. These flares ranged from X1.0 to X28, and most occurred in the maximum and descending phases of the solar cycle. The 20 X-class flares marked with blue stars during 2002 - 2005, along with 19 M-class flares, are the 39 large flares, which are used as the basis of FISM. Figure 3.3 shows that the percentage increase of the 61 X-class flares varied a lot depending on the wavelength. The red line denotes the October

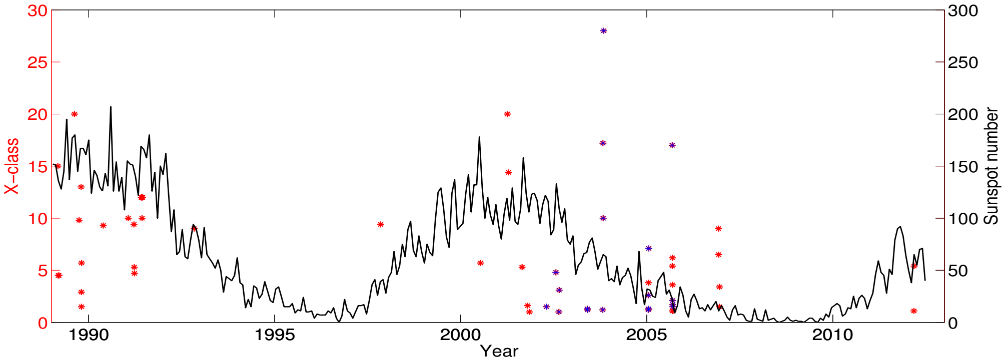

Figure 3.2. Temporal distribution of 61 X-class flares ranging from X1.0 to X28 shown in Figure 3.3. The classes are shown in left axis with stars. A flare is classified as A, B, C, M or X and there is a linear scale from 1.0 to 9.9 in each class expect X. The biggest flare ever recorded occurred on November 4, 2003 (X28). The blue stars represent the 20 X-class flares listed in Table 1 of [10], which are observed by TIMED/SEE during 2002-2005 and are part of the 39 large flares used as the basis of FISM, along with 19 M-class flares. The right axis depicts the sunspot number in black.

28th, 2003 flare event, and the green line is the average of 61 X-class flares. The 0 - 14 nm irradiance increases much more (~680% on average) than the one for 14 - 25 nm waveband (~65% on average), except for the peak around 24 nm (~220%). Moreover, the average percentage increases for 25 - 105 nm and 122 - 190 nm wavebands are ~120% and ~35%, respectively. There is a relatively small enhancement (~10%) in 15 - 25 nm wavelength range, which contains many strong solar emission lines, such as the Fe IX. When a flare happens these emissions do not increase very much, and sometimes even decrease [148]. This is because most of these emissions are formed in the solar corona at the approximate temperature of the corona around 1 to 2 million K. When there is a significant heating that heats the source ions to much higher temperatures, Fe IX quickly becomes Fe XX, for example. Therefore, the source ion population is depleted, and therefore, there is a relatively small enhancement in 15 - 25 nm wavelength range. The low enhancement in 115 - 129 nm range, excluding the

1 nm bin at 121.5 that includes the actual measurement of Hydrogen $Lyman - \alpha$, is rather instrumental. In the TIMED/SEE instrument, which FISM is based on, an Aluminum filter had to be put in place to block 99% of the $Lyman - \alpha$ emission line at 121.56 nm so that it will not saturate the detector [26]. However, it does not allow the 'wings' on each side to be measured significantly. Therefore, in the model, they all behave very close to the $Lyman - \alpha$ emission that is measured by SEE.

The solar spectrum from FISM is used as the solar input for TIE-GCM. The penetration depth of solar irradiance in different wavelengths through the atmosphere has been used as a criterion to divide the spectrum into different wavebands.

The whole irradiance spectra from 0 - 190 nm has been divided into 6 different wavebands: 0-14 nm and 14-25 nm wavebands for XUV irradiance, 25-105 nm

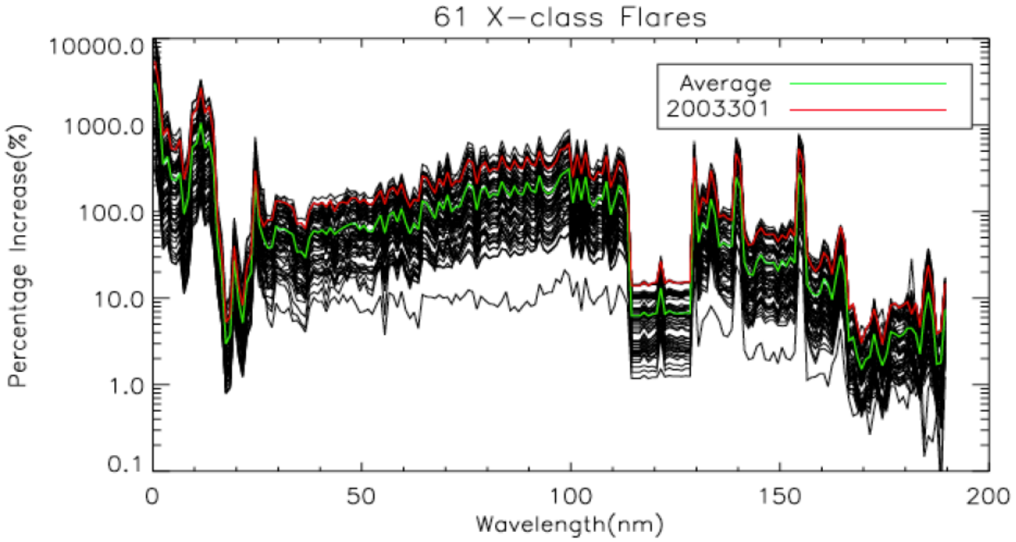

Figure 3.3. FISM solar irradiance results for percentage increases comparing the peak and pre-flare conditions for 61 X-class flares happened between year 1989 and 2012. The red line denotes the October 28th, 2003 flare event, and the green line is the average of 61 X-class flares. The low enhancement in 15 - 25 nm is a result of the depletion of source ion, while the low enhancement in 115 - 129 nm, except for the 121.5 nm bin, is rather instrumental. The lower envelope beyond 25 nm is for the X1.5 flare on April 21, 2002.

and 105-120 nm for EUV irradiance, $Lyman - \alpha$ line (121.56 nm) and 122-190 nm waveband for far ultraviolet (FUV) irradiance.

3.3.2 Temporal variation of high-altitude thermosphere response

In order to investigate the influence of solar flares at different wavelengths on the upper atmosphere, the irradiance spectra of FISM (0 - 190 nm) has been divided into six different wavebands. On October 28^{th}, 2003 (Day of year, 301), there was a X17.2-class solar flare, which was one of the most severe flares in the last solar cycle. For each waveband, two cases have been run using TIE-GCM. For example, for 0 - 14 nm waveband, in case 1, the constant solar inputs at pre-flare condition on DOY 301 have been enforced. In case 2, the temporal variation of solar irradiance in 0 - 14 nm waveband has been included. The difference between these two runs represents the influence of solar irradiance enhancement within the 0 - 14 nm wavelength bin on the thermosphere. The influence of solar irradiance enhancement within other wavebands has been calculated in the same way. To minimize geomagnetic influences, all the simulations are under the geomagnetic quiet condition ($Kp = 1$). In this study, the globally integrated or averaged values have been analyzed to focus on the large-scale response.

As shown in Figure 3.4, the temporal variations of solar irradiance flux in 0 - 14 nm, 25 - 105 nm and 122 - 190 nm wavebands have been selected and emphasized, since they have the most solar irradiance enhancement. The solar flux variations for different wavebands calculated from FISM are depicted in the first row. The solar flux in 0 - 14 nm waveband was quite small before flare (~ 1 mW/m^2) compared to that in 122 - 190 nm waveband (~ 49 mW/m^2), but it increased most (~ 20 mW/m^2) at the flare peak. The second row shows the enhancement of globally integrated solar heating in the upper atmosphere during the flare, which has been calculated through

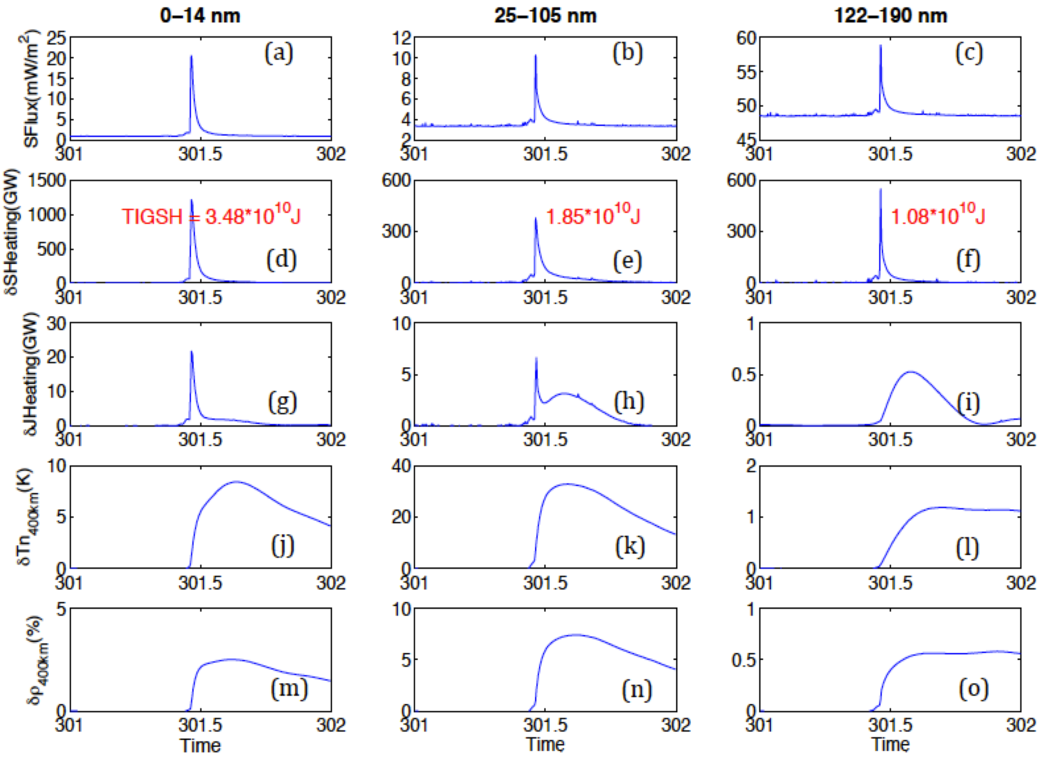

Figure 3.4. Time variations of different wavebands for DOY 301, first column for 0 - 14 nm, second column for 25 - 105 nm and third column for 122 - 190 nm. Top row (a, b, c): Solar irradiance calculated from FISM. Second row (d, e, f): Perturbation of global heating due to solar irradiance. The time integration of global solar heating (TIGSH) deposited are also labeled in red. Third row (g, h, i): Perturbation of globally integrated Joule heating. Fourth row (j, k, l): Globally averaged perturbation of temperature at 400 km. Bottom row (m, n, o): Globally averaged perturbation of neutral density at 400 km.

taking the difference between the flare and non-flare runs for each waveband. The peak of solar heating for 0 - 14 nm was the largest (∼ 1216 GW) and almost three times larger than the peak for 25 - 105 nm (∼ 379 GW). The time integration (1 day) of global solar heating (TIGSH) for 25 - 105 nm waveband (1.85×10^{10} J) is only half of that for 0 - 14 nm (∼ 3.48×10^{10} J) and larger than that for 122 - 190 nm waveband (∼ 1.08×10^{10} J). In the third row, the Joule heating enhancement due to increased Pedersen conductivity shows quite different responses in time and magnitude for different wavebands. There is a rather rapid and large enhancement of Joule heating responding to the solar flare irradiance for 0 - 14 nm waveband, however, for 122 - 190 nm, the peak of Joule heating enhancement has a obvious delay to the flare peak. The response for 25 - 105 nm is a combination of the patterns for 0 - 14 nm and 122 - 190 nm wavebands. The global Joule heating increased, but the magnitude is quite small compared with the global heating due to the solar irradiance. The irradiation in 122 - 190 nm impacts the thermosphere through dissociation, not ionization and is absorbed only by O_2, which has significant densities only in the lower thermosphere. Therefore, it affects the Pedersen conductivity indirectly through affecting the neutral temperature and density in the lower thermosphere, which in turn affect the ion density and ion-neutral collision frequency. Due to the fact that the neutral temperature and density changes persist longer than the ionization enhancements, the associated changes of Pedersen conductivity and Joule heating also persist hours after the flare. Joule heating in these results is rather small because the imposed high-latitude electric field is relatively small.

The fourth and bottom rows depict the thermospheric temperature and density perturbations at 400 km, which is close to the altitude of the Low-Earth Orbiting (LEO) satellites. The high-altitude thermospheric perturbations due to solar irradiance enhancement in 25 - 105 nm ($\sim$ 33 K increase of temperature; $\sim$ 7.4% increase of neutral density) were much larger than that in 0 - 14 nm ($\sim$ 8 K increase of temperature; $\sim$ 2.5% increase of neutral density). The enhancement of the 122 - 190 nm waveband results in little effect on the high-altitude thermospheric responses. Although the magnitude is rather small but the disturbance due to 122 - 190 nm enhancement is long lasting. The XUV irradiance (0 - 14 nm band) has a larger initial impact on the thermospheric temperature and density than the Schumann-Runge continuum, and the thermospheric perturbations due to it decays more rapidly. Most of the irradiance in 122 - 190 nm is absorbed by O_2 in the lower thermosphere. Some of the heat deposited in the lower thermosphere conducts up to the upper thermosphere and produces small but long-lasting thermospheric perturbations. Different from 122 - 190 nm, the 0 - 14 nm irradiance is absorbed by O and N_2 as well as O_2. Therefore , it has a larger fraction absorbed in the upper thermosphere compared to the Schumann-Runge continuum. As the high-altitude heat conducts downward over time, the upper thermosphere cools down.

As also summarized in table 3.1, although the largest heating enhancement comes from solar irradiance in 0 - 14 nm wavelength, most of the thermospheric perturbations at 400 km are due to 25 - 105 nm waveband. The heating efficiency, temperature and density perturbations divided by the solar heating peak, is an order larger for 25 - 105 nm waveband than those for the other two wavebands. Therefore, the solar irradiance in 25 - 105 nm of EUV influences the high-altitude thermosphere most effectively. The high-altitude temperature and neutral density respond 3 $\sim$ 5 hours later than the flare peak. This could be explained by the energy transportation time and the neutral density variation feedback to the energy absorption, which will be discussed in the next section.

Table 3.1. Heating efficiency of solar irradiance at different wavelengths to thermosphere at 400 km

	$0-14$ nm	$25-105$ nm	$122-190$ nm
δSH peak (GW)	1216	379	548
TIGSH (J)	3.48e10	1.85e10	1.08e10
δTn peak (K)	8.4	32.8	1.2
$\delta\rho$peak	2.50%	7.39%	0.58%
δTn/δSH (K/GW)	0.0069	0.0865	0.0022
δTn/TIGSH (K/J)	2.41e-10	17.73e-10	1.09e-10
$\delta\rho$/δSH (%/GW)	0.0021	0.0200	0.0011
$\delta\rho$/TIGSH (%/J)	0.7e-10	4.0e-10	0.5e-10

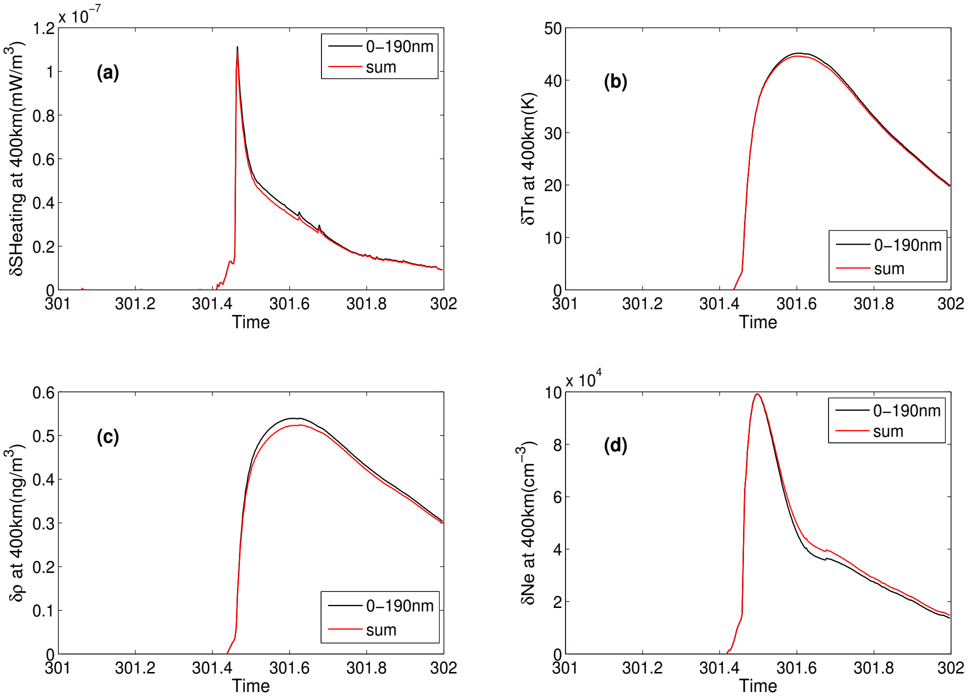

Figure 3.5. Comparison between the full simulation with the change of all wavebands and the summation of perturbations due to 6 separate bands. The black lines show the variations using FISM solar spectra in 0 - 190 nm as solar input, while the red lines represent the total sum of variations due to FISM spectra in separated wavebands. (a) Globally averaged solar heating perturbation at 400 km. (b) Globally averaged temperature perturbation at 400 km. (c) Globally averaged neutral density perturbation at 400 km. (d) Globally averaged electron density perturbation at 400 km.

Figure 3.5 compared the full simulation including all the variation in 0 - 190 nm wavelength with the summation of perturbations due to six separate wavebands. The black lines represent the globally averaged perturbations of solar heating, neutral density , temperature and electron density at 400 km due to the whole flare spectrum from 0 to 190 nm, while the red lines represent the summations of perturbations at 400 km due to six separated bands. The high-altitude response to the flare spectra in 0 - 190 nm is almost a linear combination of those to separated wavebands. The black lines and red lines are very close to each other, which illustrates the nearly linear response of T-I system at 400 km to different wavebands of solar irradiance, and suggests a possibility to predict the variations of temperature, neutral and electron density at satellites orbits due to the flares using the solar irradiance measurements at different wavebands.

3.3.3 Altitudinal distribution of the thermospheric disturbance

The results for 0 - 14 nm and 25 - 105 nm wavebands are discussed in this section since they have the most significant influence on the thermosphere. Figure 3.6 (a) depicts the altitudinal distributions of perturbations due to solar irradiance in different wavebands at the flare peak. Most of the solar irradiance in the 0 - 14 nm waveband heated the thermosphere below 150 km, while a significant part of solar heating in 25 - 105 nm was above $\sim$ 150 km. Consequently, the largest perturbations of electron density due to ionization from 0 - 14 nm waveband and 25 - 105 nm are in E region and F region, respectively. As shown in Figure 3.6 (b), the temperature perturbation below $\sim$150 km is dominated by the solar heating in 0 - 14 nm waveband, while for the upper thermosphere above 150 km, the perturbation is largest for the 25 - 105 nm waveband. Therefore, the solar irradiance in 25 - 105 nm is important for high altitude ionization and heating at flare peak, while the irradiance in 0 - 14 nm plays a dominant role below 150 km.

The temporal and altitudinal response of T-I system to solar flare irradiance varied significantly with the irradiance wavebands. Figure 3.7 shows the temporal variations of the altitudinal distributions for different wavebands: the first column for 0 - 14 nm waveband, the second column for 25 - 105 nm and the third column for the full waveband from 0 to 190 nm. As shown in the first row, the largest percentage increase of heating due to solar irradiance in 0 - 14 nm waveband is below 150 km,

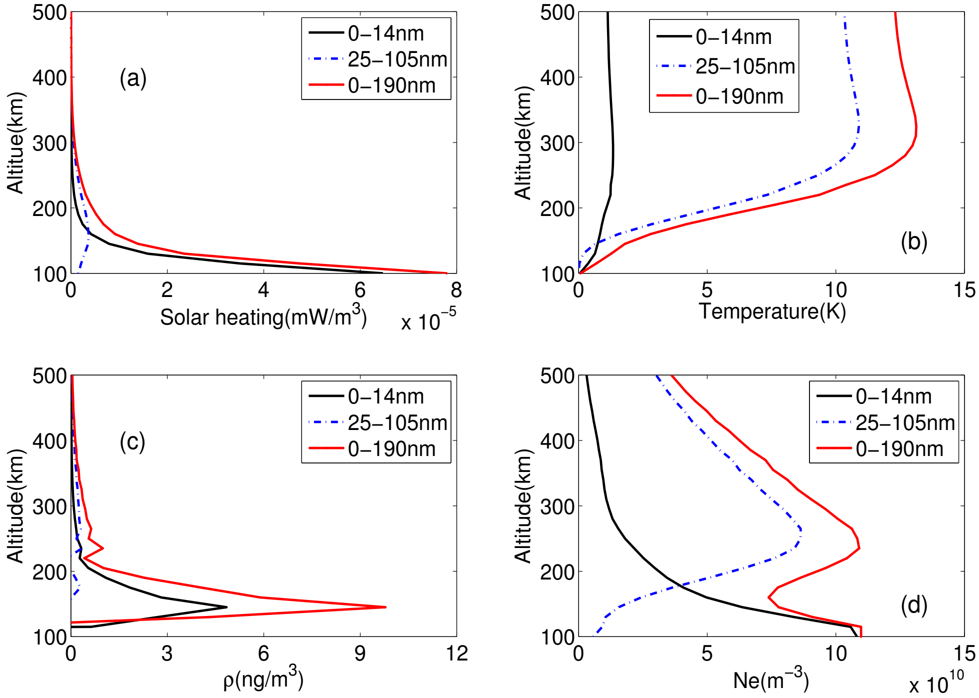

Figure 3.6. Altitudinal distribution of TIE-GCM simulation results at flare peak for solar irradiance in different wavelength ranges. (a) Globally averaged heating perturbation due to solar irradiance. (b) Globally averaged temperature perturbation. (c) Globally averaged neutral density perturbation. (d) Globally averaged electron density perturbation.

while the one in 25 - 105 nm is above 150 km. The total heating due to solar irradiance for the full waveband from 0- 190 nm increased up to 140% below ∼ 150 km. The following rows show the corresponding perturbations of temperature, neutral density and electron density, respectively. The maximum temperature perturbation for 0 - 190 nm was about 45 K at high altitude, with only 8 K contributed from 0 - 14 nm waveband and above 30 K from 25 - 105 nm waveband. Similarly, the maximum neutral density enhancement for 0 - 190 nm was around 17%, with ∼3.5% contribution from 0 - 14 nm and above 11% from 25 - 105 nm. Obviously, the solar irradiance in 25 - 105 nm plays a dominant role to impact the upper atmosphere. It can be

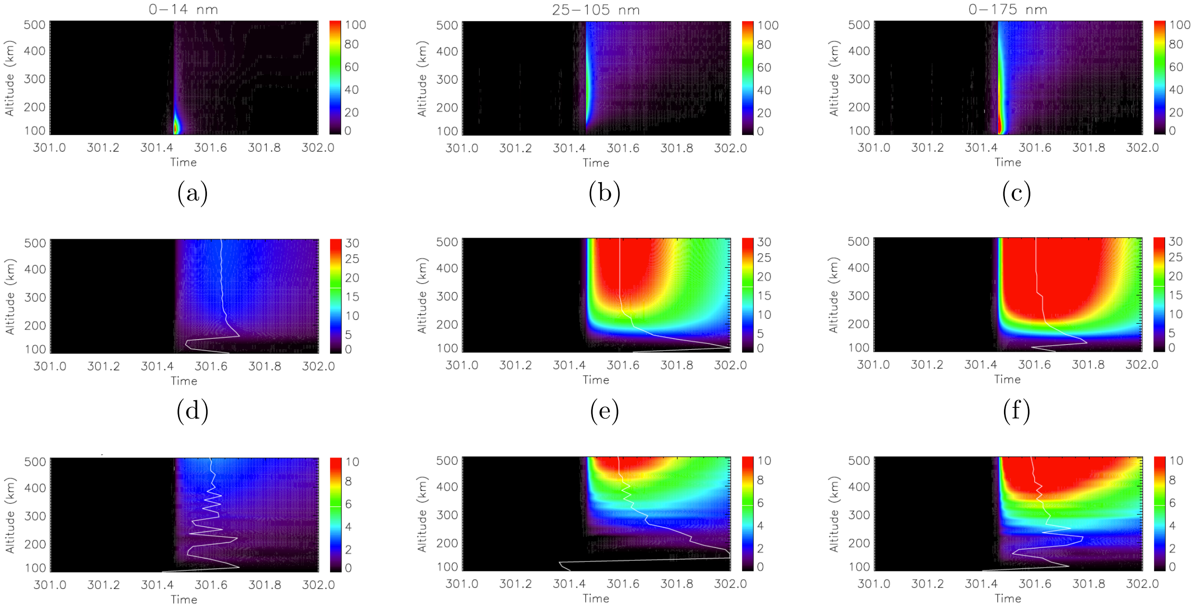

(a) (b) (c)

(d) (e) (f)

(g) (h) (i)

Figure 3.7. Temporal variations of the altitudinal distribution of TIE-GCM simulation results due to the solar irradiance enhancement in 0 -14 nm, 25 - 105 nm and 0 - 190 nm wavelength range. First row (a, b, c): Globally averaged percentage increase of solar heating. Second row (d, e, f): Globally averaged temperature enhancement. Third row (g, h, i): Globally averaged percentage increase of neutral density.

explained by the fact that the upper thermospheric response is much stronger to the heating in the upper thermosphere than to the heating in the lower thermosphere [18, 44]. The upper thermospheric perturbation peaks had 3 $\sim$ 5 hour time delay to the flare peak, which might be due to two processes. First, it takes time for heat deposited in the lower thermosphere to be redistributed by heat conduction and affect the upper atmosphere. Second, the neutral density variation feeds back to the energy absorption. The absorption rate at an altitude is proportional to the multiplication of neutral density and photon flux. The enhanced density after a flare increases the solar irradiance absorption at that altitude.

3.4 Conclusions

The response of T-I system to flare irradiance is different in magnitude and duration, since flares have different energy deposition heights, magnitudes and durations for different wavebands. The wavelength dependence of solar flare enhancement is one of the important factors determining how the terrestrial atmosphere respond to flares. The FISM data show that for the 61 X-class solar flares between year 1989 and 2012, the solar irradiance enhancement at the flare peak relative to the pre-flare condition has wavelength dependence. The solar irradiance increased most in the XUV range (0 - 25 nm), about 1000% on average, and increased about 100% in EUV range (25 - 120 nm).

The thermospheric and ionospheric response to the different wavebands of solar irradiance for the X17.2-class solar flare on October 28^{th}, 2003 has been investigated. The solar irradiance spectrum of FISM (0 - 190 nm) has been divided into six different wavebands. For each waveband, two cases have been run, for example, for 0 - 14 nm waveband, in case 1, the constant solar inputs at pre-flare condition on DOY 301 have been enforced. In case 2, the temporal variation of solar irradiance in 0 - 14 nm is included. The influence of solar irradiance enhancement in 0 - 14 nm is calculated through taking the difference between the two cases. The globally integrated solar heating and the one-day integration of it was largest in the 0 - 14 nm waveband. The impact of solar irradiance enhancement on the thermosphere at 400 km is largest for 25 - 105 nm waveband, which accounts for about 33 K in total 45 K temperature disturbance, and about 7.4% in total 11% neutral density enhancement at 400 km. The effect of 122 - 190 nm irradiance is small in magnitude, but is long lasting.

CHAPTER 4

GEOMAGNETIC ENERGY INPUTS INTO THE UPPER ATMOSPHERE ASSOCIATED WITH HIGH-SPEED SOLAR WIND STREAMS IN 2005

4.1 Introduction

During the declining phase of the solar cycle, when the IMF is decreasing and the solar irradiation remains almost constant [36], high-speed solar wind streams (HSSs) are typical and dominate the Sun-Earth interaction. For much of 2005, an unusual arrangement of three equally-spaced coronal holes resulted in a sequence of HSSs that corotated past the Earth at intervals of 9 days [128]. The strong correlation between these solar wind stream, geomagnetic activity and thermosphere density at a 9-day period has been reported recently [58]. Specifically, a 9-day recurrence seen in neutral densities derived from accelerometer measurements on the CHAMP satellite [91] is simultaneously present in the solar wind and geomagnetic activity index Kp, but not in the solar EUV flux [88], which indicates a strong linkage between solar wind energy input into the magnetosphere and thermospheric density. [130] reported a predominant 7-day oscillation in the 2006 CHAMP-derived thermospheric density, and related this oscillation to solar wind fast streams. The global mean Total Electron Content (TEC) [59] and $\sum O/N_2$ ratios measured by the Global Ultraviolet Imager (GUVI) on the TIMED satellite [16] also present strong 9 and 7 day periodic oscillations in 2005 and 2006, respectively, that are well correlated with the solar wind speed and Kp index.

While it is proposed that the periodic oscillations observed in thermosphere/ionosphere are a direct response to recurrent geomagnetic activity and associated high-speed solar wind streams, the energy transfer processes between the solar wind, the magnetosphere and the ionosphere are not clear and still a key question for the solar wind/magnetosphere/ionosphere coupling. The 9-day periodicity has been reported in the global electron particle precipitation [23, 154] and the localized Joule heating [115], but no periodic oscillation in the global integrated Joule heating has yet been presented due to the difficulty of global measurement. At present, there are no direct ways to measure the total energy deposited by Joule heating in the polar region. It is however very important to confirm if the periodic oscillation exists in the integrated Joule heating and varies in the same manner as neutral density.

In this study, we investigate two major magnetospheric energy deposition methods, Joule heating and particle precipitation, associated with this 9-day periodic oscillation. Joule heating and hemispheric power (HP) from Assimilative Mapping of Ionospheric Electrodynamics (AMIE) [97] output have been examined with the Lomb-Scargle spectral analysis [61, 109]. The correlation of the energy inputs to the neutral density variation has been evaluated using the band-pass filter centered at 9-day period. The sensitivities of Joule heating and HP to the solar wind speed have been examined as well. The [31] model and [139] model have been used for the empirical conductance and electric potential, respectively. Only ground-base magnetometer data ($>$ 80 magnetometers) for the entire year 2005 have been assimilated. The outputs of AMIE include Joule heating, HP, D_{st} and cross polar cap potential (CPCP).

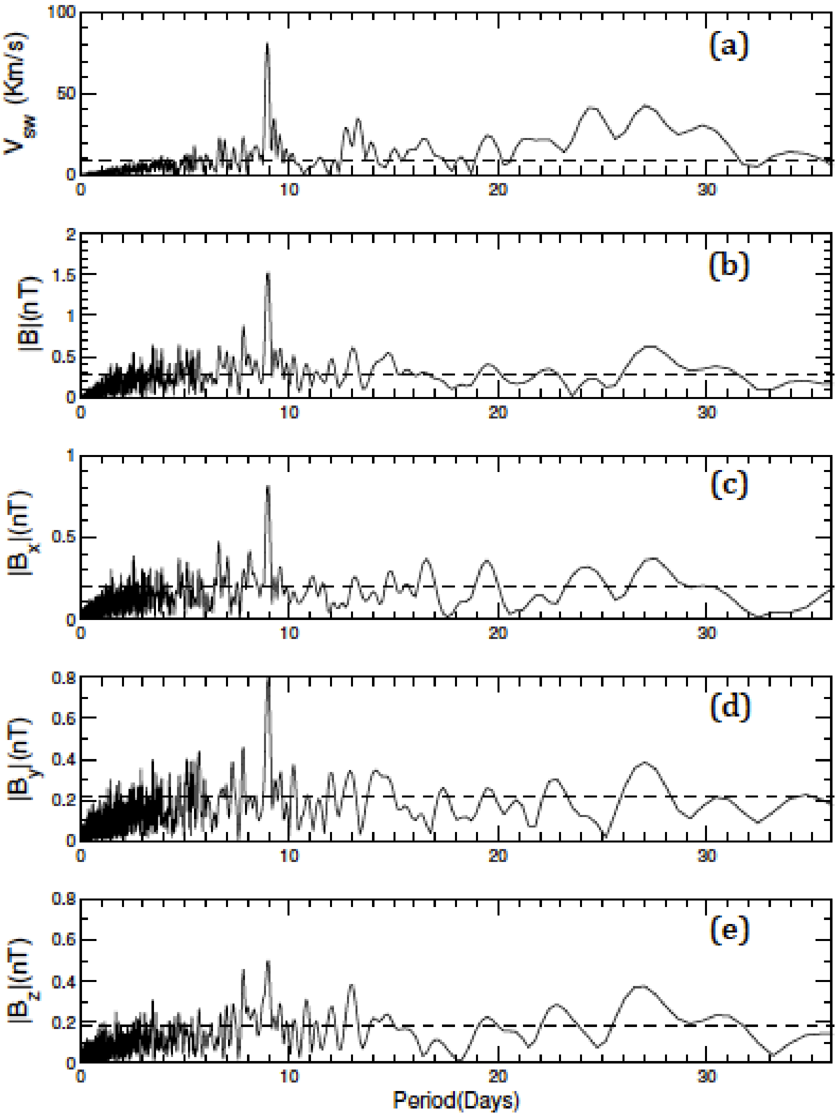

Figure 4.1. Periodograms of (a) solar wind speed, (b) $|B|$, (c) $|B_x|$, (d) $|B_y|$ and (e) $|B_z|$ in 2005 from Lomb-Scargle spectral analysis (GSFC/SPDF OMNIWeb interface at http://omniweb.gsfc.nasa.gov). The dashed lines represent the 99% significance level.

4.2 Results and Discussion

4.2.1 Lomb-Scargle analysis

The interaction between the high-speed stream (HSS) and the slower solar wind ahead of it forms a compression region, the corotating interaction region, in which the magnetic field intensity and solar wind density are enhanced due to the compression [5]. When there is a strong 9-day periodic oscillation in solar wind, we expect that a similar oscillation appears in IMF. Figure 4.1 depicts the periodograms of solar wind speed and IMF intensity and components from Lomb-Scargle spectral analysis. The dashed lines are the upper limits of the 99% significance level. To reduce the effect of IMF sector polarity [54] and the high frequency oscillation of the IMF in corotating interaction regions (CIRs), we choose $|B_x|, |B_y|$ and $|B_z|$ over B_x, B_y and B_z in our analysis. The solar wind speed periodogram clearly shows a prominent peak at 9 days associated with the three equally spaced high-speed streams. There is also a 9 day peak in the IMF intensity and components that is related to the enhanced magnetic fields in the corotating interaction regions formed at the leading edges of the high-speed streams. Both IMF and solar wind velocity affect the magnetic reconnection rate in the magnetosphere, such as the dayside Magnetic Merging Rate ($MMR = V^{4/3}B_T^{2/3}sin^{8/3}(\theta_c/2)$[74]), and the Interplanetary Electric Field ($IEF = -V \times B$), which directly controls magnetospheric energy inputs into the upper atmosphere . Therefore, there are two components associated to HSSs that influence the magnetospheric energy inputs into the upper atmosphere: the direct variation in solar wind velocity and the indirect variation in IMF. Since the effects of the variation in the solar wind speed and IMF cannot be separated through the data analysis in this study, the change of solar wind speed has been used to represent all the corresponding change in the solar wind conditions caused by HSSs.

Figure 4.2 shows that the Lomb-Scargle periodograms of Joule heating, CPCP, HP and D_{st} index from AMIE output in 2005 have clear peaks at 9 day above the 99% significance level. Joule heating and particle precipitation are two primary methods through which the magnetospheric energy is deposited in the upper atmosphere. The 9-day periodicity in particle precipitation has been seen in NOAA particle observa-

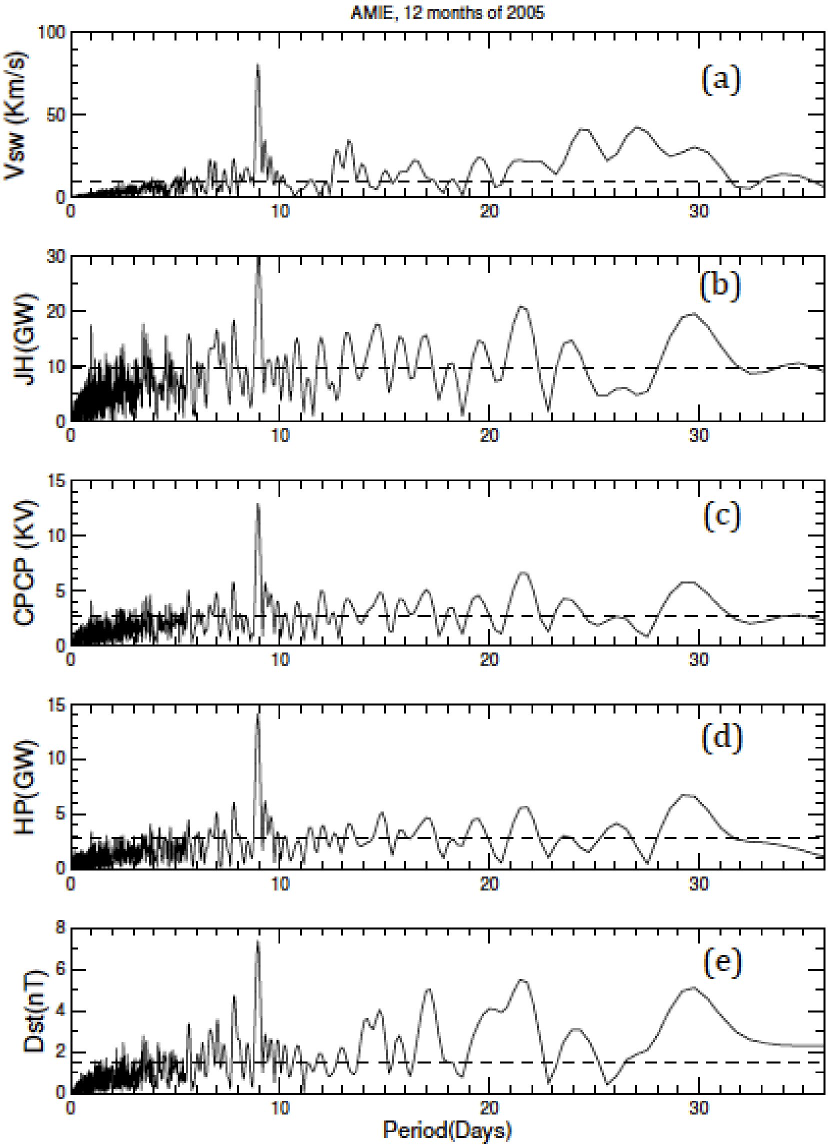

Figure 4.2. Periodograms of (a) solar wind speed, (b) Joule heating, (c) CPCP, (d) hemispheric power and (e) D_{st} in 2005 from Lomb-Scargle spectral analysis of AMIE outputs. The dashed lines represent the 99% significance level.

tions [23] and TIMED GUVI observations [154]. However, a 9-day periodicity of the global integrated Joule heating has not been reported due to the difficulty of measurement. The data assimilated model, AMIE, is an important method to estimate the variation of global Joule heating and other energy inputs, although it is limited by the distribution and quality of data and the assumptions carried by the model. For example, the distribution of the magnetometer data is not uniform and quite sparse at some locations. Joule heating related to the small-scale electric field variation is not well presented in the model. As shown in Figure 4.2, the existence of 9-day oscillation in the integrated Joule heating has been demonstrated for the first time. Comparison of the magnitudes of the 9-day oscillations between Joule heating and HP shows that the amplitude of Joule heating at 9-day is close to 30 GW and almost two times as large as that of HP (14 GW), which indicates that Joule heating might be more important than HP in producing the 9-day oscillations in thermospheric density.

The prominent feature of a 9-day periodicity in the solar wind speed during 2005 is quite unusual and different periodicity peaks may present in different years [130]. Nevertheless, the coexistence of the 9-day periodic variation in both the solar wind speed and the magnetospheric energy inputs supports the cause and effect relationship between HSSs and thermospheric density enhancements. The ICMEs in 2005 [94] produced significant geomagnetic storms and technically their contribution cannot totally be excluded in the processing. Since ICMEs are transient phenomena and have no well-organized repeatable feature with a 9-day periodicity like HSSs, their contribution to the 9-day period oscillations should not be dominant.

Figure 4.1 shows a dominant 27-day peak in both solar wind speed and IMF conditions, which is directly related to the solar rotation. However, in Figure 4.2, there is no peak at 27 days but a primary peak at 30 days instead in both Joule heating and HP. The 30-day peak and 27-day minimum have also been shown in Kp [58], HP and O/N2 from TIMED/GUVI observations [154]. The stronger geospace driver in the 30-day component than in the 27-day component is a very interesting feature and will be investigated at some point.

4.2.2 Band-pass filter and sensitivity of energy inputs to the solar wind speed

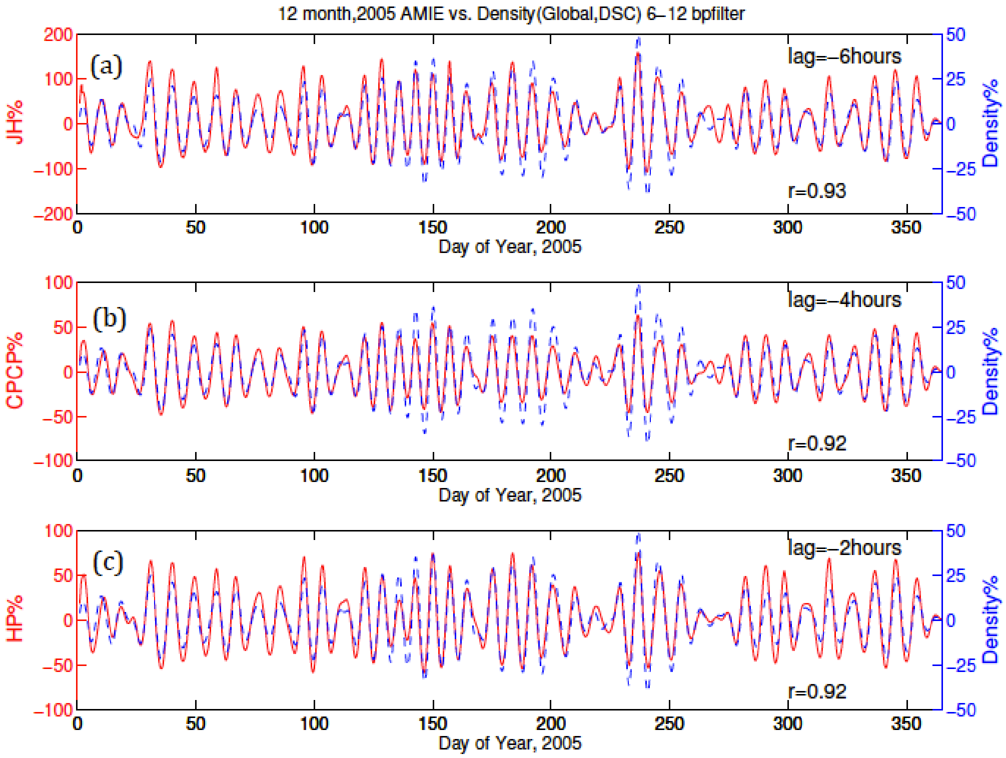

Figure 4.3. Band-pass filtered results. (a) The percentage of the band-pass filter Joule heating residuals (red) from AMIE output to the 12-day running mean and the percentage of the band-pass filter neutral density residuals (blue) from CHAMP satellite measurements to the 12-day running mean. The band-pass filter is centered at 9 days with range from 6 to 12 days. The X-axis is the day of year (DOY) in 2005 and the Y-axis is the percentage difference. The correlation coefficient between Joule heating and neutral density is $r = 0.93$ and the observed neutral density variation is 6 hours after the Joule heating variation. Lag=-6 Hours shows that the observed neutral density variation is 6 hours after the Joule heating variation. (b) The same as the top except for the CPCP and the neutral density with 4 hours lag between them. (c) The same as the top except for the HP and the neutral density with 2 hours lag between them.

A band-pass filter centered at 9 days with range from 6 to 12 days has been utilized to further study the energy transfer processes from the high-speed solar wind streams into the upper atmosphere through Joule heating and particle precipitation.

Figure 4.3 shows the percentage of the band-pass filtered Joule heating residuals (red) to the 12-day running mean and the percentage of the band-pass filtered CHAMP measured neutral density residuals (blue) to the 12-day running mean. The correlation coefficient between Joule heating and neutral density is $r = 0.93$. The correlation coefficient between HP and neutral density is also high ($r = 0.92$). The very good correlation between AMIE outputs and thermospheric neutral density for 6-12 days periodic oscillation suggests that the energy associated with the high-speed solar wind streams is dissipated in the upper atmosphere through both Joule heating and particle precipitation heating.

The sensitivities of Joule heating and HP variations to the solar wind speed change have been compared for year 2005. First, the same band-pass filter process has been applied to the solar wind data. The band-pass filtered Joule heating residuals are then correlated with solar wind speed residuals after taking into account the time lag between them. Due to the nonsinusoidal nature of the periodicity, the specific period window (6-12 days) has been used for the band-path filter. We have also investigated the situations with other window size (7-11 days and 8-10 days) and find only very slight change in the sensitivity ($\leq 5\%$).

Figure 4.4 presents the variations of Joule heating and HP corresponding to the variation of solar wind speed. The red lines are the best-linear-fit, which show that the sensitivity of Joule heating to the solar wind speed is close to 0.40 GW/(km/s), and the sensitivity of HP to the solar wind speed is close to 0.15 GW/(km/s). When the solar wind changes from low-speed stream (400 km/s) to high-speed stream (700 km/s), Joule heating and HP increase by 120 GW and 45 GW, respectively. In a quiet time, the average value of Joule heating and HP are close to 95 GW and 36 GW [52]. These results indicate that the high-speed solar wind streams roughly double the quiet time magnetospheric energy inputs into the upper atmosphere and cause global variations. The red lines in Figure 4.4 only represent the statistical average. Due to the difference of the IMF and solar wind conditions other than the solar wind speed, the slope has a relatively broad range, including some outlying paths. Meanwhile, the red line may not represent the response to ”pure” high-speed streams because of the influence of transient activities, but represents the yearly average response to high-speed streams.

A direct comparison of the relative significance of Joule heating and HP on CHAMP densities should be made with caution, because Joule heating and HP influence the upper atmosphere through different processes. For HP, only a fraction ($\sim 50\%$ [90]) goes into heating the neutral atmosphere directly with the remainder going into ionization, dissociation and emission. In contrast, all of the Joule heating

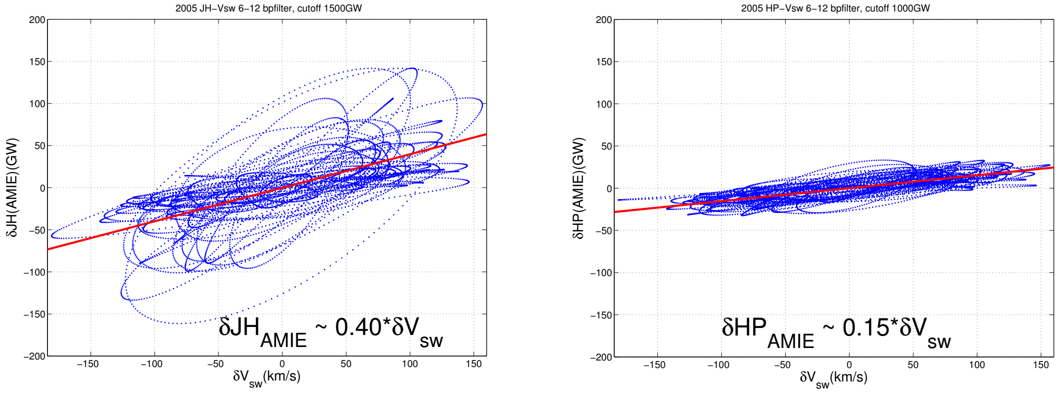

(a) (b)

Figure 4.4. Sensitivities of Joule heating and hemispheric power to the solar wind speed. (a) Sensitivity of the Joule heating variation to the periodical oscillation of the solar wind speed. The X-axis is the solar wind speed residual after the 6-12 day band-path filter and the 0 point represents the average. The Y-axis is the corresponding Joule heating residual after taking into account the time lag between Joule heating and solar wind speed. The linear fit is plotted out in the red line and the correlation between Joule heating and solar wind speed is close to 0.40 GW/(km/s). (b) The same as the left except for the sensitivity of hemispheric power (HP) to solar wind speed. The correlation between HP and solar wind speed is close to 0.15 GW/(km/s).

heats the atmosphere. Simulation study is needed in the future to compare the consequences in the thermosphere of the Joule heating and HP changes related to the high-speed solar wind streams. In this paper only the sensitivity of energy inputs to the solar wind speed has been presented. Given that the magnetospheric energy input into the upper atmosphere depends on both solar wind and IMF, the sensitivity to other parameters, such as BV^2 and ρV^2, is also very important and has been investigated in a separated paper [43], and will be mentioned in the next section.

4.2.3 Comparison of Joule heating between different models and observations

The capability of General Circulation Models (GCMs) to precisely simulate the variations of neutral density, composition and temperature caused by the solar wind speed highly depends on the capability of electrodynamic models driving GCMs to represent the variations of ionospheric forcing related to solar wind speed. The energy of solar wind is deposited into the upper atmosphere mainly by Joule, or frictional heating and particle precipitation heating [64, 132]. Joule heating usually plays a much more significant role than particle precipitation in dissipating energy and affecting the dynamics of upper atmosphere [62, 52, 18]. A couple of models have been created to describe the magnetospheric energy input into the upper atmosphere. For example, the NCAR newly developed empirical model shows an improved description of the Joule heating in the thermosphere [20]. [68] presented a model of the total integrated Joule heating as a function of IMF. However, none of them specifically investigates the solar wind speed dependence of Joule heating.

In this section, we focus on the dependence of Joule heating on the solar wind speed changes. A year of data in 2005 from different electrodynamic models and observations are employed to compare their capabilities to represent the variations of forcing associated with the solar wind speed changes. The variations of the cross polar cap potential (CPCP) and northern hemisphere integrated Joule heating (IJH) are examined and the periodicities present in CPCP and IJH are evaluated using Lomb-Scargle spectral analysis. Utilizing a bandpass filter centered at 9 days, the sensitivity of the IJH modeled by the empirical formulations and different data sources to the solar wind speed is examined. This comparison of different observations and models helps us to estimate Joule heating more precisely, and gives an improved quantitative understanding of the solar wind/Magnetosphere/Ionosphere coupling processes.

The CPCP and IJH in year 2005 have been calculated from different observations and models, which have been widely used in the space physics community [62, 102, 49, 145, 13] and have been summarized in 4.1. For AMIE 1, only the data from ground-based magnetometers are assimilated. Magnetometers offer a consistency in location of measurement that in-situ satellites do not offer. For AMIE 2, both the ground-based magnetometer data and the DMSP convection data are assimilated.

Table 4.1. Models and observations.

Model/observation	Description	Used quantities	
DMSP (F13)	Satellite		CPCP
Weimer05	Empirical model	IJH	CPCP
AMIE 1	Data assimilative model (ground magnetometers only)	IJH	CPCP
AMIE 2	Data assimilative model (ground magnetometers + DMSP convection data of F13 and F15)	IJH	CPCP

4.2.3.1 Temporal variation of high-latitude electrodynamics

To compare the seasonal variations of the CPCP and IJH from different sources in year 2005, monthly averages of outputs are calculated and shown in Figure 4.5. The first panel depicts the monthly averaged CPCPs measured by DMSP F13 satellite, calculated from Weimer05, AMIE 1 and AMIE 2. The numbers in the legends demonstrate the yearly averaged values of CPCPs, which is 49 kV for DMSP, 56 kV for Weimer05, 54 kV for AMIE 1 and 61 kV for AMIE 2. The CPCPs from Weimer05 and AMIE 1 are very close on average, while the CPCP from AMIE 2 is about 13% larger than that from AMIE 1. CPCPs from Weimer05, AMIE 1 and 2 agree better in summer than in winter. With only the ground-based magnetometer data assimilated, CPCP from AMIE 1 is sometimes smaller than that from Weimer05, however, with both the ground-based magnetometer data and space-based DMSP convection data assimilated, the CPCP from AMIE 2 always tends to exceed that from Weimer05.

The CPCPs from Weimer05, AMIE 1 and 2 exhibit similar seasonal variations with two maxima around May and September due to the combined effect of dipole title angle and orientation of IMF. A clear seasonal variation is shown in the CPCP from DMSP and the difference between summer and winter can be as much as 40 kV, which makes the CPCP in winter 45% larger than that in summer. Because the DMSP satellites do not go through the maximum and minimum of the true potential, the 45% enhancement of the DMSP measured CPCP in the winter does not necessarily indicate a 45% increase of the real CPCP. This seasonal variation of CPCP from DMSP has also been reported in other years and the percentage enhancement in winter on average is 10-15% [78, 49]. During the summer season, the CPCP from DMSP is typically smaller than those from other sources. For instance, compared to Weimer05, it is 10-20 kV smaller. During the winter season, the CPCP from DMSP tends to increase and is larger than those from other sources. Because of the winter helium bulge, [He^+] is significantly enhanced in winter even with lower solar fluxes [89, 76, 93]. Therefore, the ratio of [He^+]/[O^+] at a fixed altitude increases in winter and makes the DMSP ion drift measurements difficult [113]. The measurement of DMSP satellites therefore is less reliable during winter, which partially contributes to the large seasonal variation of the potential drop. For the last two months of 2005 (DOY 300-365), DMSP measurements are consistently larger then Weimer05 by 10-30 kV, which results in the difference between AMIE 1 and 2. Besides the possibility that the DMSP ion drift measurements in winter are less reliable than in summer, the minimum value for conductance of AMIE might be too high for winter, resulting

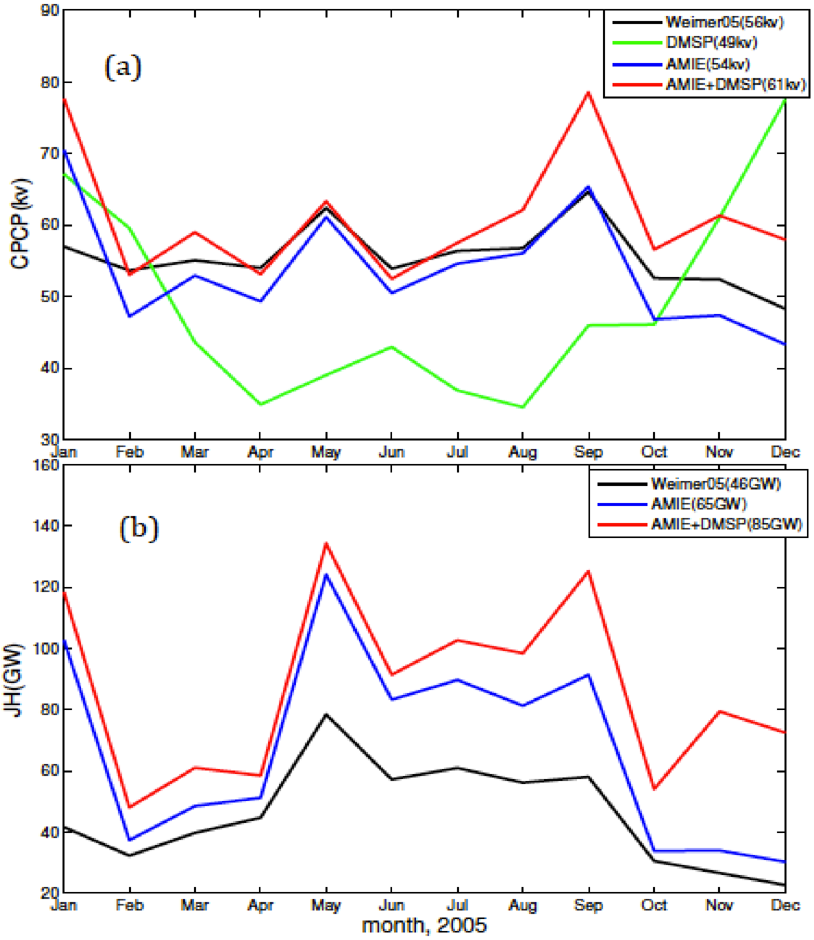

Figure 4.5. Monthly averaged cross polar cap potential and northern hemisphere integrated Joule heating from different models. (a) the monthly averaged cross polar cap potentials (CPCP) in year 2005 from Weimer05 (black), DMSP satellite F13 (green), AMIE 1 (blue) and AMIE 2 (red). The number in the legend shows the yearly averaged CPCPs from different sources. (b) the same as the top panel, but for northern hemisphere integrated Joule heating (IJH) from Weimer05, AMIE 1 and 2.

in low of a potential [102, 49] for the magnetometer only run. Therefore, physical interpretation of the seasonal dependence should be made with caution.

The difference between AMIE 1 and 2 represents the effect of the DMSP data on AMIE CPCP, which depends on the season, the quality of the data and the way AMIE ingests data. To emphasize the relative contribution of DMSP data to the AMIE run, the CPCP percentage difference between DMSP and AMIE 1, and the percentage difference between AMIE 2 and AMIE 1 have been shown in Figure 4.6. In general, these two have a positive correlation, which indicates that the impact of the DMSP data on AMIE is larger when the difference between DMSP and AMIE 1 is larger. The measurement of DMSP satellites is less reliable for the winter than for the summer, which partially contributes to the large seasonal variation of the DMSP CPCP. In AMIE, a single set of fitted coefficients is applicable simultaneously to the fitted distribution of the potential, independent of the measurement type [97], and thus the assimilation of the DMSP data changes the fitted coefficients and changes the global patterns of the ionospheric convection. AMIE utilizes Weimer96 as the background model and assimilates data from observations. In principle, the more data AMIE ingests, the more realistic the result should be, since the error associated with the spatial smoothing is reduced. However, the observational error might increase concerning the quality of data that ingested. Therefore, the impact of the data to the AMIE result is a balance between different processes.

The bottom panel of Figure 4.5 shows the monthly averaged IJHs in 2005 from Weimer05, AMIE 1 and AMIE 2. The numbers in legends demonstrate the yearly averaged IJHs, which is 46 GW for Weimer05, 65 GW for AMIE 1 and 85 GW for AMIE 2. The IJH from AMIE 1 is about 41% larger than that from Weimer05, whereas IJH from AMIE 2 is about 85% large than that from Weimer05, and 31% larger than that from AMIE 1 on average. All of the outputs show a clear seasonal variation,

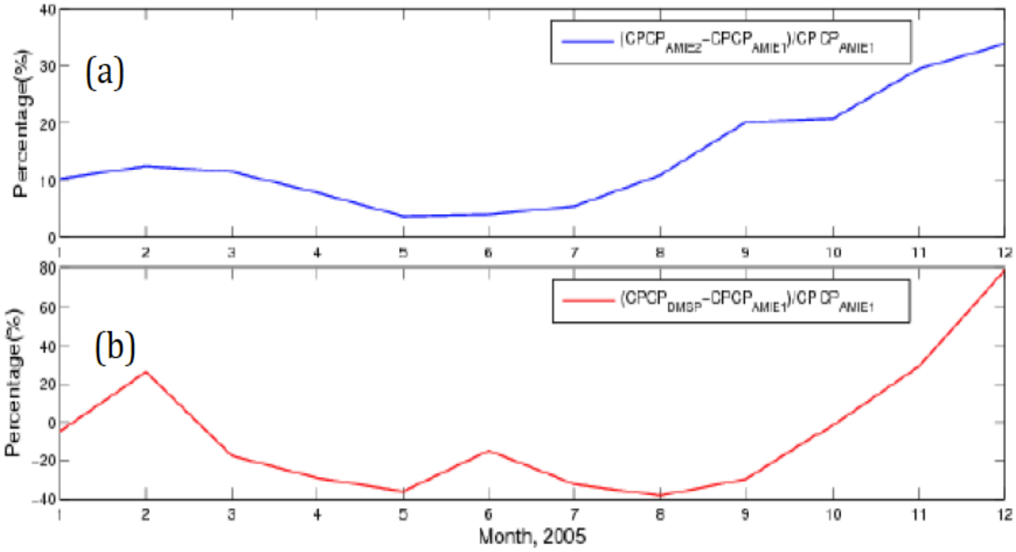

Figure 4.6. Comparisons of CPCPs between different models. (a) the CPCP percentage difference between AMIE 1 and AMIE 2 for year 2005. (b) the CPCP percentage difference between DMSP and AMIE 1 for year 2005.

with a relatively larger IJH in summer than in winter. The seasonal variation of the ionospheric conductivity in the northern hemisphere from solar irradiation results in larger IJHs in May than in September. IJHs from AMIE 1 and 2 are larger than that from Weimer05 in all seasons. The difference between Weimer05 and AMIE indicates that both the ground magnetometer and satellite observations can significantly change the estimation of Joule heating.

To show the contribution of the spatial scale variations to the difference between AMIE and Weimer IJHs, the global distributions of Joule heating rates from Weimer and AMIE 1 have been compared. The first panel of Figure 4.7 shows the distributions of Joule heating rate from Weimer and AMIE 1 for the northern hemisphere at 0300 UT on April 7th, 2005, when the solar wind speed was 483 km/s and the IMF Bz was -2.27 nT. The IJH is about 46 GW for both Weimer and AMIE 1. Although the positions of maximum Joule heating rate are different on the dawnside,

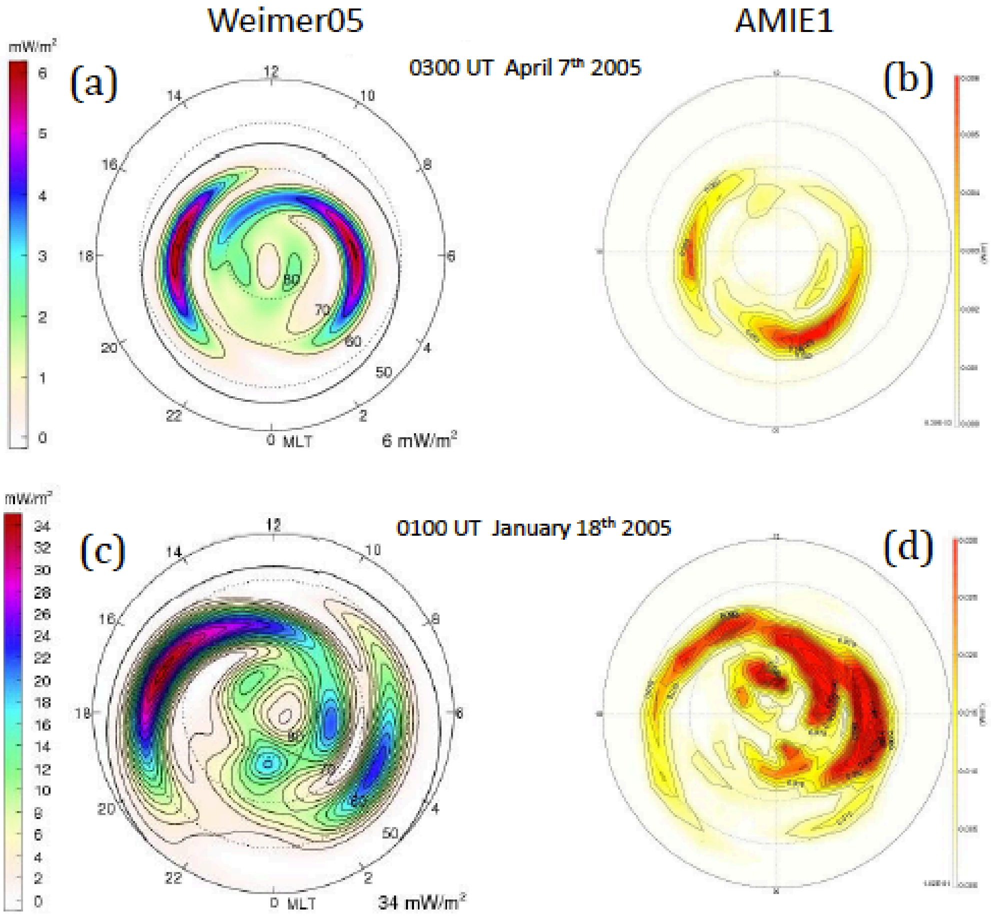

Figure 4.7. Comparisons of Joule heating distribution between Weomer05 and AMIE 1. Top (a, b): the Joule heating distributions of northern hemisphere at 0300 UT on April 7th, 2005 derived from Weimer05 (left) and AMIE 1 (right). Bottom (c, d): the same as the top panel, but for distributions at 0100 UT on January, 18th, 2005 derived from Weimer05 (left) and AMIE 1 (right).

the maximum values are close and the distribution areas were similar. The second panel of Figure 4.7 shows the distributions of Joule heating rates from Weimer and AMIE 1 at 0100 UT on January 18th, 2005, when the solar wind speed was 580 km/s and the IMF Bz was -11.7 nT. The IJH is about 371 GW for Weimer and 461 GW for AMIE 1. They have similar structures, such as one peak on the dawnside and two peaks on the duskside. However, the dawnside Joule heating rate peaks are smaller

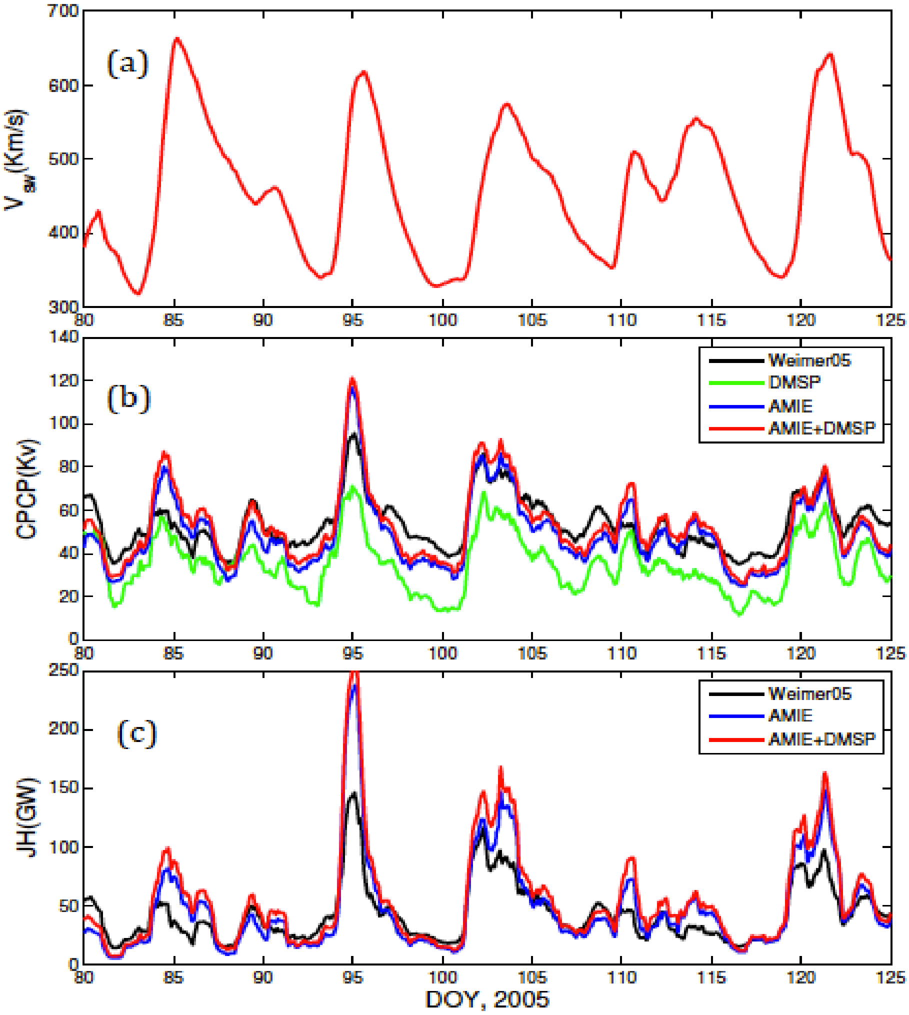

Figure 4.8. Solar wind speed, CPCPs and IJHs from day of year 80 to 125. (a) daily average of solar wind speed (GSFC/SPDF OMNIWeb interface at http://omniweb.gsfc.nasa.gov) from day of year 80 to 125 of 2005. (b) daily average of CPCPs from Weimer05, DMSP satellite F13, AMIE 1 and 2 for the same interval as the top panel. (c) the same as the middle panel, but for IJHs from Weimer05, AMIE 1 and 2.

and smoother in Weimer than in AMIE 1. This indicates that the spatial variation of AMIE 1 was bigger than that of Weimer on the dawnside, which may contribute to the difference of IJH between AMIE and Weimer.

The IJH is one of the global quantities that represent the significant features of high-latitude ionospheric electrodynamic states. The global quantities are often more reliable than many characteristics of the patterns themselves, since much of the random error or uncertainty inherent in the patterns is effectively averaged out in producing the global quantities [98]. Therefore, this paper emphasizes the integrated Joule heating rate. The distribution is certainly very interesting and desires a more systemic study in the future.

In year 2005, the HSSs from three solar coronal holes dominated the Sun-Earth interaction, resulting in a 9-day periodicity in the energy input into the geospace. Figure 4.8 depicts the daily average of solar wind speed (from the OMNI 2 database), CPCPs and IJHs from the different simulations and sources from day of year (DOY) 80 to 125. In this 45-day interval, there are five HSSs resulting in increases of the CPCPs and IJHs correspondingly. The second panel shows that for the times of fast solar wind, for example, from DOY 94 to 96, the CPCP from AMIE 1 and 2 exceed the CPCP from Weimer05. Similarly, as shown in the bottom panel, for the times of fast solar wind, the IJH from AMIE 1 and 2 exceeds that from Weimer05. For the times of slow solar wind, for example, from DOY 97 to 101, the CPCP from AMIE 1 and 2 are smaller than that from Weimer05, but the IJH from Weimer05, AMIE 1 and 2 agree well. The different correlation between CPCP and IJH during slow and fast solar wind periods indicates a non-linear relationship between CPCP and IJH.

Meanwhile, the electric and magnetic potentials are calculated independently in Weimer05, which could lead to spatial mismatch between E and B potentials, and can definitely impact the Joule heating estimation in Weimer05. As shown in [20], Weimer05 estimates the height-integrated Joule heating from the pointing flux at the top of ionosphere, which is the vector cross product of the statistical averages $< E >$ and $< B >$ ($< E > \times < B > / \mu_0$). It is different from Joule heating calculated from the statistical average of cross product $< E \times B >/\mu_0$, which includes the interaction between E and B, and represents the Joule heating more appropriately.

The Joule heating by AMIE might be underestimated due to the non-uniform distribution of the data, overestimation of the conductance and model uncertainty. [13] compared the Joule heating measured by the Sondrestrom incoherent scatter radar with that modeled by AMIE during a moderate storm on 9-10 January 1997. It was found that the overall average Joule heating rate modeled by AMIE (3.5 mW/m^2) is 29% less than that measured by Sondrestrom (5.0 mW/m^2), as shown in Figure 3 of [13]. Running Weimer05 for this interval, we found that the average Joule heating rate modeled by Weimer05 is about 1.75 mW/m^2, which is about 50% of AMIE output. The comparison between Weimer05, AMIE and Sondrestrom observation indicates that AMIE may give a more realistic estimation of the Joule heating than Weimer05. Certainly, it is just one particular example and more comprehensive statistics study is needed before making a general conclusion.

The error of AMIE model includes observational errors, errors associated with AMIEs inherent spatial smoothing and errors associated with inaccuracies in the simplifying physical assumptions that are used [99]. While the errors have not been saved in AMIE outputs for this study, the statistically expected root-mean-square value of the error is roughly 20% [97]. Certainly, the relative importance of the electric field error to the estimation of Joule heating depends on the quality and spatial coverage of the available data [98].

4.2.3.2 Spectral analysis and sensitivity study

A spectral analysis is conducted to illustrate the 9-day periodicity present in the solar wind speed and other variables for year 2005. Figure 4.9 depicts the Lomb-Scargle periodograms of daily solar wind speed, CPCP and IJH from the different simulations and sources. The dashed line shows the upper limit of the 99% significance level of each quantity, and a period with power above this line has confidence greater than 99%. The number in the legend shows the value of the 9-day peak of each quantity. The 9-day periodicity can be clearly seen in CPCP and IJH from all sources. However, the magnitudes of CPCP and IJH from Weimer05 are much smaller than those from others. For example, the 9-day peaks of the CPCP from the DMSP measurements and AMIE runs are about 1.4 and 1.8 times larger than that from Weimer05. The 9-day peaks of the IJH from AMIE 1 and 2 are 2.0 and 2.4 times larger than that from Weimer05, respectively. In addition, although the 9-day peaks of CPCP from AMIE 1 and 2 are the same, the 9-day peak of IJH from AMIE 2 is about 18% larger than that from AMIE 1, which again suggests the non-linear relationship between CPCP and IJH. The solar wind speed shows 27-day periodic oscillation due to the rotation of the Sun. However, the IJH from all sources consistently show the elimination of 27-day peak and a dominant 30-day peak instead. This is possibly caused by the interaction between the solar wind and the magnetosphere, and a more systematic study is desirable.

To investigate the dependence of the IJH on the solar wind speed, oscillations of the IJH centered at 9-day are filtered utilizing a band-pass filter from 6 to 12 days as illustrated in Figure 4.9. The solar wind data have also been processed in the same manner and correlated with the IJH to calculate the time lag between them. Taking into account this lag, the variation of the IJH verses the variation of solar wind speed is plotted in Figure 4.10. Then the best linear fit to the whole year data is used to represent the sensitivity of IJH to the solar wind speed on average. Figure 4.10 depicts the sensitivities of IJH to the solar wind speed for Weimer05, AMIE 1 and 2. The correlation coefficient is printed in the top right corner and the red line represents the best-linear-fit of the dependence. All of them show positive dependence

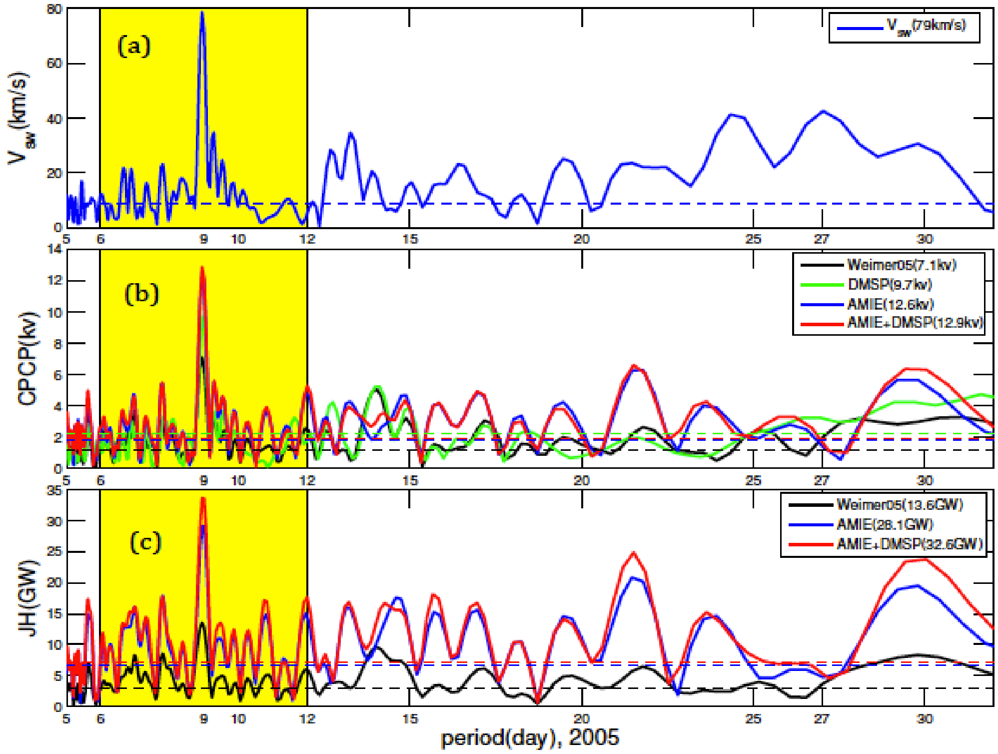

Figure 4.9. LombScargle spectrums of daily average (a) solar wind speed, (b) CPCP and (c) IJH in year 2005 from different models and observations. The dashed lines represent the 99% significance level. The numbers in the legends show the values of the 9-day peak of each quantity. The yellow areas illustrate the band-pass filter centered at 9 days.

on the solar wind speed, but with different sensitivities. The IJH from Weimer05 is approximately proportional to the solar wind speed as 0.19 GW/(km/s), while the IJH from AMIE 1 and 2 are proportional to the solar wind speed as 0.42 and 0.47 GW/(km/s). When the solar wind speed increases 400 km/s (e.g. from 400 to 800 km/s), the IJHs from Weimer05, AMIE 1 and 2 will increase 76, 168 and 188 GW, respectively. Therefore, the IJH from AMIE 1 and 2 have a sensitivity to changes in the solar wind speed about 2.2 and 2.5 times larger than that from Weimer05. This is close to the ratio of the 9-day peaks shown in Figure 4.9.

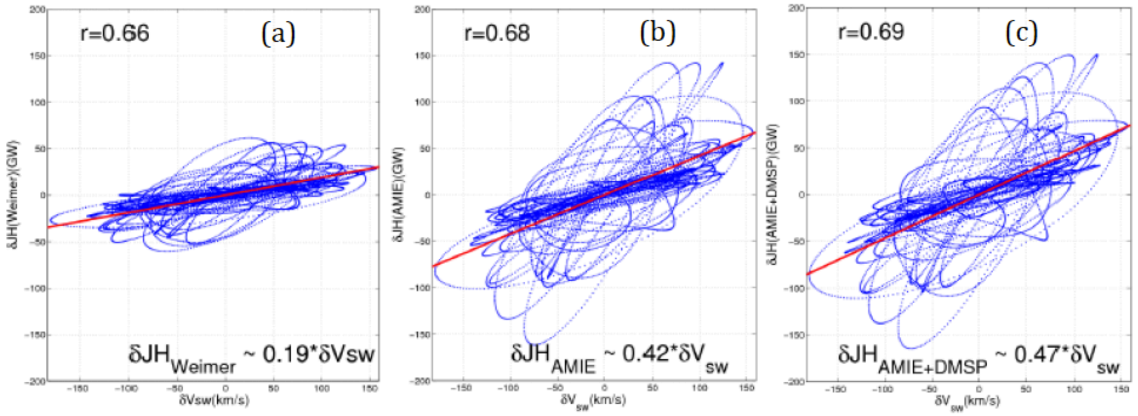

Figure 4.10. Sensitivities of the IJH variation from (a) Weimer05, (b) AMIE 1 and (c) AMIE 2 to the solar wind speed variation. The X-axis is the solar wind speed residual after the 6-12 day band-path filter. The Y-axis is the corresponding IJH residual after taking into account the time lag between IJH and solar wind. The best linear fit is plotted out as the red line. The correlation coefficient between IJH variation and solar wind speed variation is printed in the top right corner.

The dependence of the IJH on the solar wind speed has previously been studied by [152] using a compiled empirical global Joule heating model (CEJH). When the solar wind speed increased by 400 km/s with other parameters fixed (B_t = 10.0 nT, N_{sw} = 8.0/cc, Tilt = 23.9°, clock angle = 135.0°, K_p = 4.0, $F_{10.7}$ = 226, AL = -200 nT), the IJH increased by 167 GW such that the sensitivity of the IJH to solar wind speed changes is around 0.42 GW/(km/s). Similar sensitivity (0.41 GW/(km/s)) is obtained when using the same parameters as input to the empirical model Weimer05. This similarity is not surprising, since Weimer05 and Weimer01 used for the electric potential model in CEJH are similar in most quiet and moderate geomagnetic conditions [141]. However, this sensitivity is higher than that of Weimer05 shown in this study (0.19 GW/(km/s)) and there are several possible reasons for the discrepancy. The analysis in [152] is highly case-dependent. If parameters for a rather quiet time are used as inputs, the sensitivity is very small. For instance, in an extremely quiet case (B_t = 1.4 nT, N_{sw} = 5.0/cc, Tilt = -22.5°, clock angle = 135.0°), IJH just increased by 17 GW resulting in a sensitivity of 0.04 GW/(km/s). Our results present a yearly average, which is lower than that in the active time shown in [152]. Moreover, there is a 9 day peak in the IMF, which is related to the enhanced magnetic fields in the CIRs formed at the leading edges of the high-speed streams [18]. The effect to the Joule heating caused by the IMF change has also been included in our analysis but not in [152].

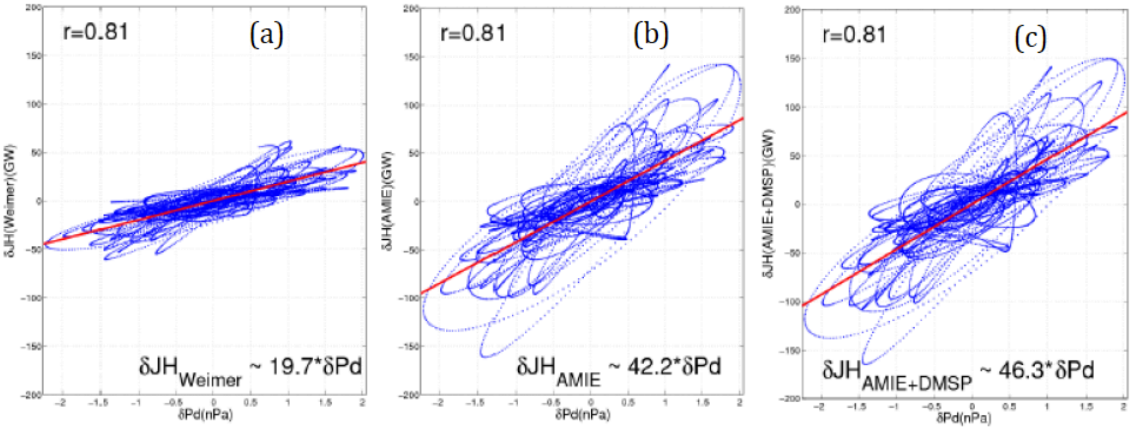

Figure 4.11. Same as Figure 4.10 except for the solar wind dynamic pressure.

Figure 4.11 depicts the sensitivity of the IJH to the solar wind dynamic pressure changes for Weimer05, AMIE 1 and 2. The correlation coefficients are all the same at 0.81. The best-linear-fit lines show positive dependences as 19.7, 42.2 and 46.3 GW/nPa, respectively. [77] has studied the role of solar wind dynamic pressure in driving Joule heating in several events (three substorms and one synthetic event) using the global MHD model GUMICS-4. It was reported that the dependence is 2.96 GW/nPa for southward IMF and 2.19 GW/nPa for northward IMF, which is close to one order of magnitude smaller than our results. This difference is possibly caused by the underestimation of Joule heating in the GUMICS-4 simulations. [77] pointed out that the Joule heating simulated by GUMICS-4 is 10 times smaller than that from [28], which describes the single hemispheric IJH at the equinoxes. The empirical formula (IJH $= 4+20\times \mathrm{K}_p$) in [28] represents a climatologic average situation and underestimates Joule heating compared with AMIE results in our study. We furthered the sensitivity study to test the effect of the magnitude of IMF $|B|$ and the product $|B|V^2$. The IJH from AMIE 1 and 2 have consistent sensitivities about 2.2 and 2.4 times larger than that from Weimer05.

4.3 Conclusion

The 9-day periodicity found in the upper atmosphere is consistent with a similar periodicity present in the solar wind speed. To understand the energy transfer processes into the upper atmosphere associated with high-speed solar wind stream, we first examined solar wind speed and IMF conditions in year 2005 by Lomb-Scargle spectral analysis. The solar wind speed periodogram clearly shows a prominent peak at 9 days associated with the three equally spaced high-speed streams. There is also a 9 day peak in the IMF intensity and components that is related to the enhanced magnetic fields in the corotating interaction regions formed at the leading edges of the high-speed streams. The Lomb-Scargle periodograms of Joule heating, CPCP, HP and D_{st} index from AMIE outputs in 2005 have clear peaks at 9 days. The presence of 9-day periodic oscillation in integrated Joule heating is demonstrated for the first time due to the difficulty to measure the global integrated Joule heating in observation.

The strong correlation of the 9-day oscillation in Joule heating and particle precipitation to the variation in neutral density suggests that the energy transfer processes into the upper atmosphere associated with high-speed solar wind stream is a combination of Joule heating and particle precipitation, while Joule heating may play a more important role. The sensitivities of Joule heating and HP to the solar wind speed are close to 0.40 GW/(km/s) and 0.15 GW/(km/s). When the solar wind changes from low-speed stream to high-speed stream, Joule heating and HP increase by 120 GW and 45 GW, respectively, which indicates that the high-speed solar wind streams roughly double the quiet time magnetospheric energy inputs into the upper atmosphere and cause global variations.

We also have collected a year of convection data from two DMSP satellites (F13 and F15), and yearly runs of the empirical model Weimer05 and two different inputs to the data assimilative model AMIE, one assimilating only the ground-based magnetometers (AMIE 1), the other assimilating both the magnetometer data and DMSP convection data (AMIE 2). The cross polar cap potential (CPCP) and northern hemisphere integrated Joule heating (IJH) calculated from different sources are compared for year 2005.

The results show that the yearly averaged CPCPs from Weimer05 and AMIE 1 are very close whereas the yearly averaged CPCP from AMIE 2 is about 11% larger than that from Weimer05, and 15% larger than that from AMIE 1. The IJH from AMIE 1 is about 41% larger than that from Weimer05, and the IJH from AMIE 2 is about 85% large than that from Weimer05, and 31% larger than that from AMIE 1 on average. The potential drop measured by DMSP satellite F13 shows a clear seasonal variation, with summer less than winter, while CPCPs from other sources have larger values in summer. And for all the sources, IJHs are relatively larger in summer than in winter because of the additional solar conductance.

Corresponding to the 9-day periodicity in Solar wind speed, CPCPs and IJHs from different sources present dominant 9-day period peaks in the Lomb-Scargle spectral analysis. The sensitivity of IJH to solar wind speed is then investigated utilizing a bandpass filter from 6 to 12 days centered at 9 day. The variation of IJH shows a positive dependence on the variation of solar wind speed from all sources. However, the sensitivities of IJHs from AMIE 1 and 2 are about 2.2 and 2.4 times larger than that from Weimer05, respectively. Further study of the IJH dependence on solar wind dynamic pressure Pd, $|B|$ and $|B|V^2$ consistently shows that IJHs from AMIE 1 and 2 have sensitivities about 2.2 and 2.4 times larger than that from Weimer05.

The results of this study improve our capability to describe Joule heating related to the variation of solar wind properties and provide more accurate estimation of the magnetospheric energy input into ionosphere/thermosphere, which are important for understanding the physical processes in the solar wind/magnetosphere/upper atmosphere coupling.

CHAPTER 5

HEIGHT DISTRIBUTION OF JOULE HEATING UNDER DIFFERENT SOLAR CONDITIONS AND ITS INFLUENCE ON THE THERMOSPHERE

5.1 Introduction

The magnetospheric energy input to the upper atmosphere in the polar regions can significantly affect the dynamics and structure of the coupled thermosphere-ionosphere system [39, 40, 63]. It is important to estimate the magnetospheric forcing variation and its impact on the upper atmosphere accurately. Due to spatial and temporal limitations of direct observations, it is difficult to obtain a global view of electrodynamic quantities like Joule heating from these alone. To supplement the observational evidence, three-dimensional, time-dependent thermosphere-ionosphere general circulation models can be used to estimate the Joule heating distribution and its effects.

A number of previous studies have examined the two-dimensional distribution of height-integrated Joule heating [64, 141, 18, 43], while few studies have investigated the altitudinal distribution of Joule heating [129, 19, 17]. As discussed in [27], the consequence of Joule heating on the thermospheric temperature depends on its height profile. If energy is deposited at high altitudes, larger temperature response is expected at those high altitudes. Most of the Joule heating is deposited in the upper part of the ionospheric E region, where the Pedersen conductivity usually maximizes [7]. [17] showed that Joule heat deposited at higher altitudes (F region) has a much larger impact than that deposited at lower altitudes (E region) in affecting the neutral density at 300 km, using the Global Ionosphere Thermosphere Model (GITM)

[101] simulations. [17] examined the high-altitude thermosphere variation at a particular location for the first hour after an abrupt Joule heating enhancement, roughly dividing the thermosphere into E and F regions at 150 km.

In this study, the effect on the thermosphere at 400 km (the altitude of the CHAMP satellite orbit) of Joule heating deposited at different pressure levels is investigated systematically over a longer period (days) and with different solar activity conditions. The investigation we did in this paper is quite different from previous studies. Rather than investigating the height distribution of Joule heating per unit mass, which is important for determining the temperature response on short time scales, before heat is conducted or radiated away, we instead examine the total globally integrated Joule heating and the response of thermosphere for longer time scales, which show the effects of both the heat conduction and radiative cooling. The characteristic time scales of heat conduction and radiative cooling are investigated using both the TIE-GCM and a simple one-dimensional model to explain the responses of temperature and density at 400 km to heat deposition at different heights.

5.2 TIE-GCM simulations

5.2.1 Model conditions

The latest version (v1.94) of the National Center for Atmospheric Research Thermosphere - Ionosphere - Electrodynamics General Circulation Model (TIE-GCM) is employed. TIE-GCM is a first-principle, three-dimensional, non-linear representation of the coupled thermosphere and ionosphere system. It solves the momentum, energy and continuity equations for neutral and ion species in pressure coordinates [107] with $5^\circ \times 5^\circ \times$ half scale height resolution (longitude × latitude × altitude). It has a self-consistent calculation of ionospheric wind dynamo effects [100]. The external forcings are mainly the solar irradiance, magnetospheric energy, and tidal perturbations at the lower boundary of the model. The Heelis potential model [41] is used to specify the high-latitude electric field in this study, with a 50 kV cross-polar-cap potential. The hemispheric power of precipitating auroral particles is set to 20 GW. To show the solar cycle dependence of the results, simulations are conducted for both solar minimum ($F_{10.7} = 70$ sfu, year 2008) and solar maximum ($F_{10.7} = 200$ sfu, year 2001).

Observations [e.g.,][122,] and modeling [e.g.,][57,] indicate that the density disturbances originating in the polar regions spread globally fairly rapidly, reaching the equator within about four hours. In this study we focus primarily on time scales of hours to days, for which the thermospheric response is global. Therefore, the results are analyzed in terms of values horizontally integrated or averaged over the globe. By taking the global average, we also smooth out complex smaller-scale features like traveling atmospheric disturbances.

To analyze the influence of Joule heating at a particular pressure level, we could run the TIEGCM with the Joule heating turned off at that level, and then subtract results of that run from results of another run in which all Joule heating is kept active. The differences in model output would represent the effects due to the difference of heating between the two runs, which would correspond to a switched-on source at that level (since the run with switched-off heating was subtracted from the run with full heating). What we actually do is different from this, but should give nearly the same results, if the the model responds approximately linearly to changes in heating. Starting at day of year (DOY) 80, we first run the TIE-GCM for 20 days until DOY 100 to reach a steady state. We then turn off all the Joule heating below a specified pressure level and run for another 4 days, from DOY 100 to 104. This specified pressure level, which is referred to as cutting pressure level (CPL) in this paper, is set progressively higher for successive runs. As the CPL increases, a larger and larger amount of Joule heating is missing from the model. The thermosphere below the CPL cools, the downward heat conduction above the CPL increases, and the temperature at 400 km decays at a rate which increases with the CPL. If the simulation were run long enough, a new equilibrium would eventually be reached, in which the revised heating, downward heat conduction, and radiative cooling would again come into balance. Next, we take the difference between runs with CPLs one scale height apart to represent effects of a change in heating throughout a layer one scale height thick. For example, the difference between two runs with CPLs 0.5 and 1.5 is taken to represent the effects of Joule heating "switched on" in one full scale height centered at pressure level 1. If we examine the thermospheric response to the switched-on Joule heating in a particular layer, we find that the total downward heat conduction above the heating layer initially decreases and the temperature at 400 km increases. Instead of considering this as a reduction of total downward heat conduction above the heating layer, we can also consider it as an upward conduction of heat from the heating layer, superposed upon the background downward heat conduction. That is, Joule heat deposited in the layer conducts both upward and downward away from the layer.

Very similar results are obtained for differences calculated when Joule heating is turned off above, instead of below, a given pressure level (not shown), validating our assumption that the response is nearly linear for the moderate levels of Joule heating we use.

5.2.2 Height distribution of Joule heating

Figure 5.1 shows the daily average of globally-integrated Joule heating deposited per scale height when the heating at all altitudes is turned on. We use pressure level as the vertical coordinate for this theoretical study. The corresponding geometric altitudes for the solar minimum and maximum cases are also shown in brackets (smin/smax). For both the solar maximum (solid line) and solar minimum (dashed line) cases, the largest Joule heating deposition per scale height happens at pressure level ($z = ln(p_0/p)$, where p_0 is the reference pressure) -4, which is around 125 km in altitude. The altitudinal distribution of Joule heating varies with solar cycle. Due to the increased electric conductivity, Joule heating in the solar maximum case is larger than that in the minimum case at all pressure levels, as expected. Although the structures are similar, in the F region, around pressure level 0, there is a large difference between solar minimum and maximum, owing to the much larger Pedersen conductivity there at solar maximum. In our study, about 18% of the total Joule heating is deposited above 150 km for the solar minimum case, and about 34%

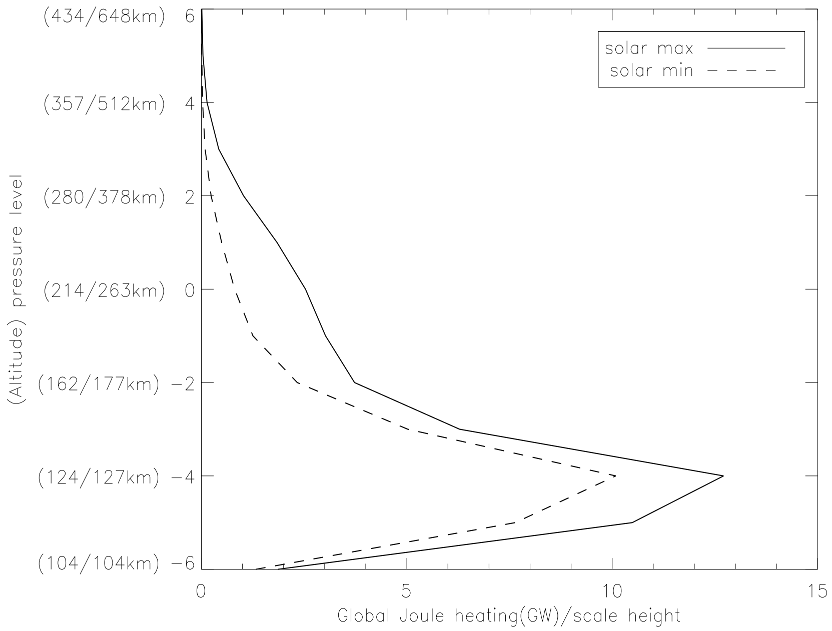

Figure 5.1. Globally integrated Joule heating per scale height. The solid line is for solar maximum and the dashed line is for solar minimum. The y-axis is described in pressure levels and also in geometric altitude (brackets).

is deposited above 150 km for the solar maximum case. In the theoretical study of [17], approximately 25% of the total Joule heating was deposited above 150 km at a particular location, which falls in between our results.

5.2.3 Response of the thermosphere at 400 km to heating at different heights

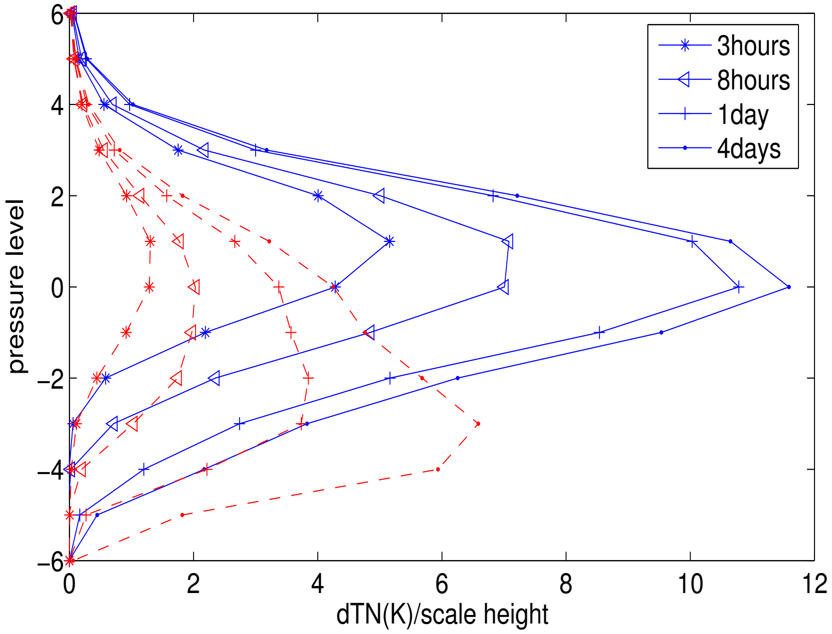

Figure 5.2. Temperature perturbation at 400 km responding to heat deposited at different pressure levels at times $t = 3hours$, $t = 8hours$, $t = 1day$, and $t = 4days$. The solid blue line is for solar maximum and the dashed red line is for solar minimum.

By calculating the difference of temperatures at 400 km for two successive runs with CPLs one scale height apart, the influence of Joule heating deposited between these two pressure levels on the high-altitude temperature is obtained. As explained in Section 2.1, the temperature change can be interpreted as though Joule heating had been switched on between the two CPLs, with heat then conducting upward and downward away from the heating layer. Figure 5.2 illustrates the variation of the globally-averaged temperature perturbation at 400 km to the Joule heating deposited at different pressure levels after 3 hours, 8 hours, 1 day and 4 days. The blue solid lines are for solar maximum and the red dashed lines are for solar minimum. For both cases, the temperature perturbation after 3 hours has little response to the low-altitude (e.g., pressure level -3) heating, while there are immediate responses to high-altitude (e.g., pressure level 0) heating. At solar maximum, the temperature at 400 km continues to respond most strongly to heat deposited around pressure level 0 for all times out to 4 days, but there is also increasing influence from the heat deposited at lower altitudes. In contrast, at solar minimum, the heating height for which the temperature at 400 km responds most strongly descends with increasing time, down to pressure level -3 after 4 days. In fact, at pressure level -3, for times beyond about 6 hours, the temperature response at 400 km is greater at solar minimum than at solar maximum, in spite of less heating at this level at solar minimum (Figure 5.1). At solar maximum, the much larger F-region heating around pressure level 0 ensures that the high-altitude thermospheric temperature response is at least twice as large as that at solar minimum, for all times out to 4 days.

To understand the different responses of the high-altitude temperature to heating at different altitudes and different levels of solar activity, it is useful to examine the time scales of heat conduction and radiative cooling at different heights, as shown in Figure 5.3. The global-average values of the characteristic heat conduction time τ_κ, described later in section 3, as obtained from the TIE-GCM simulations for solar minimum (dashed line) and maximum (solid line), are depicted with red lines. At pressure level -3, τ_κ is about 12 hours, while at pressure level 0 it is about 50 minutes. Therefore, the characteristic time for temperature perturbations to conduct upward to 400 km is much faster for high-altitude heating than for low-altitude heating. At a given pressure level, τ_κ is slightly smaller for solar minimum than for solar maximum,

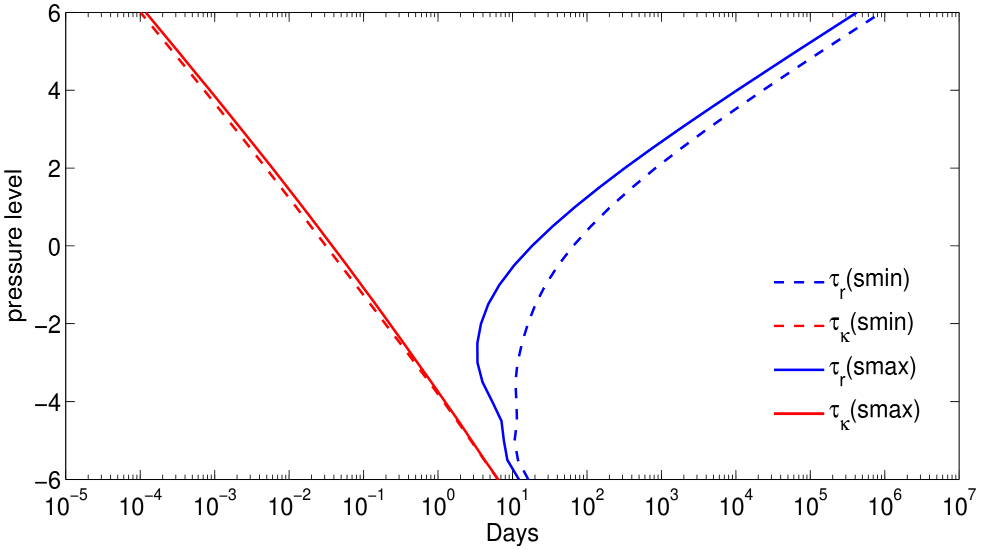

Figure 5.3. Altitudinal variation of time scales for heat conduction (τ_κ) and radiative cooling (τ_r). The solid line is for solar maximum case and the dashed line is for solar minimum case.

as explained in section 3. Figure 5.3 also depicts the global-average values of the characteristic radiative cooling time τ_r in blue lines for solar minimum (dashed line) and maximum (solid line), obtained by dividing the global-average specific enthalpy, c_pT, by the global-average rate of radiative heat loss per unit mass at a given pressure level, dQ_r/dt. τ_r is 3 days or more at all heights, and is smaller at solar maximum than at solar minimum. The thermospheric heat is lost in the form of infrared radiative cooling, mainly by carbon dioxide (CO_2) and nitric oxide (NO). The cooling rate is faster at solar maximum because of an increased concentration of NO. Because of this, much of the low-altitude heat at solar maximum is lost through radiation before it can conduct up to the upper thermosphere, making the low-altitude heating less effective in raising the temperature at solar maximum than at solar minimum. It should be noted that the chemical production of NO increases with increasing temperature [71, 2], leading to an increase in NO density and a decrease in τ_r that applies not only to the temperature perturbation, but also to the background temperature. That is, the radiative cooling is nonlinear with respect to temperature, such that τ_r in Figure 5.3 overestimates the effective radiative time scale, and underestimates its solar-cycle dependence. This fact can help explain why the solar minimum/maximum difference in high-altitude temperature response to low-altitude heating seen in Figure 5.2 after four days is greater than would be expected by a simple consideration of the radiative cooling rates obtained from Figure 5.3. The importance of the heat conduction time scale τ_κ and the radiative cooling time scale τ_r will be discussed in more detail in section 3.

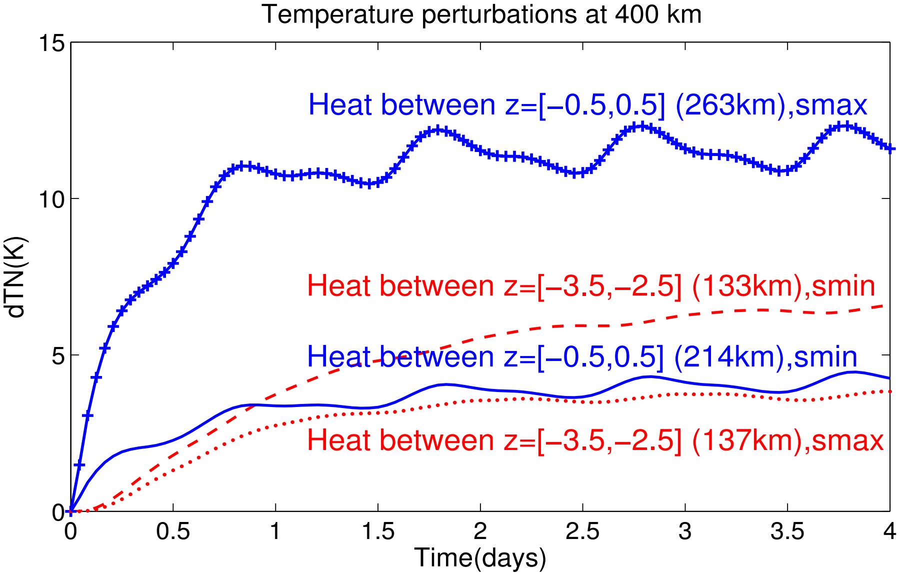

Figure 5.4. Temporal variation of globally averaged temperature perturbations at 400 km due to heat deposited in one scale height centered at pressure level 0 (blue lines) or -3 (red lines).

For the long-term response of the temperature perturbation at 400 km, the profiles in Figure 5.2 after 4 days peak for Joule heating deposited in the scale height centered at ∼ 140 km (pressure level -3) for solar minimum and ∼ 263 km (pressure level 0) for solar maximum. The integration of each profile in Figure 5.2 with respect to pressure level gives the total temperature variation at 400 km responding to the total deposited heat for each case. The heating above 150 km (18% of total energy) causes about 60% of the total temperature variation at 400 km at solar minimum at 4 days, while at solar maximum, it accounts for 34% of the total heat and is responsible 90% of the temperature variation.

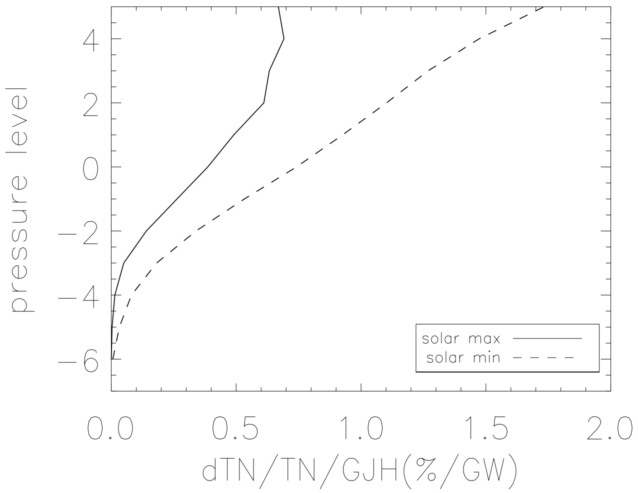

Figure 5.5. Percentage temperature increase at 400 km per unit Joule heating input after 4 days. The solid line is for solar maximum and the dashed line is for solar minimum.

Figure 5.4 depicts the temperature changes due to heat deposited in one scale height centered at pressure levels -3 and 0, at both solar minimum and maximum. There is some daily modulation of heat input as the Earth rotates, which causes the daily variation in temperature responses. The high-altitude heating (blue lines) produces stronger initial responses than the low-altitude heating (red lines). However, at solar minimum, after ∼20 hours, the low-altitude heating produces a larger temperature response at 400 km than the high-altitude heating. It is also found that Joule heating deposited in the low altitude for solar minimum changes the temperature at 400 km more than for solar maximum. As discussed for Figure 5.3, this could be explained by the fact that in a steady state, when heating and cooling are balanced, more low-altitude heating is radiated away before it can conduct up to 400 km at solar maximum than at solar minimum.

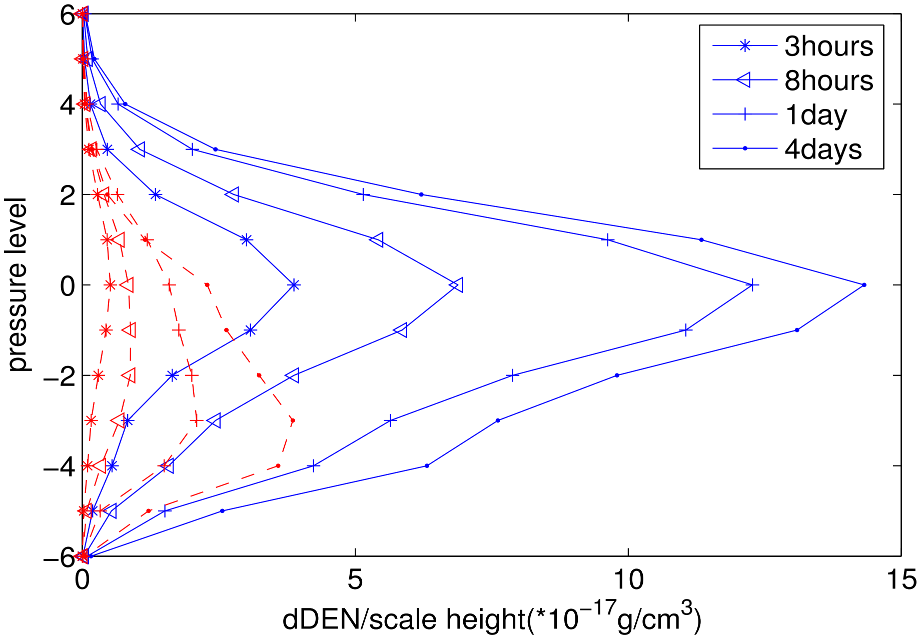

Figure 5.6. Neutral density perturbation at 400 km responding to heat deposited at different pressure levels at times $t = 3hours$, $t = 8hours$, $t = 1day$, and $t = 4days$. The solid blue line is for solar maximum case and the dashed red line is for solar minimum case.

Figure 5.5 shows the percentage temperature increase at 400 km per unit energy input 4 days after the heat is turned off below the CPLs, as a function of the height of the input. This is obtained by dividing the percentage temperature variation at 400 km to Joule heating at a given pressure level by the Joule heating deposited at that level. This represents the heating efficiency of Joule heating to the temperature. It increases with height, and is larger for solar minimum at all pressure levels compared with solar maximum, due both to the lower background temperature and to the slower loss of heat at solar minimum.

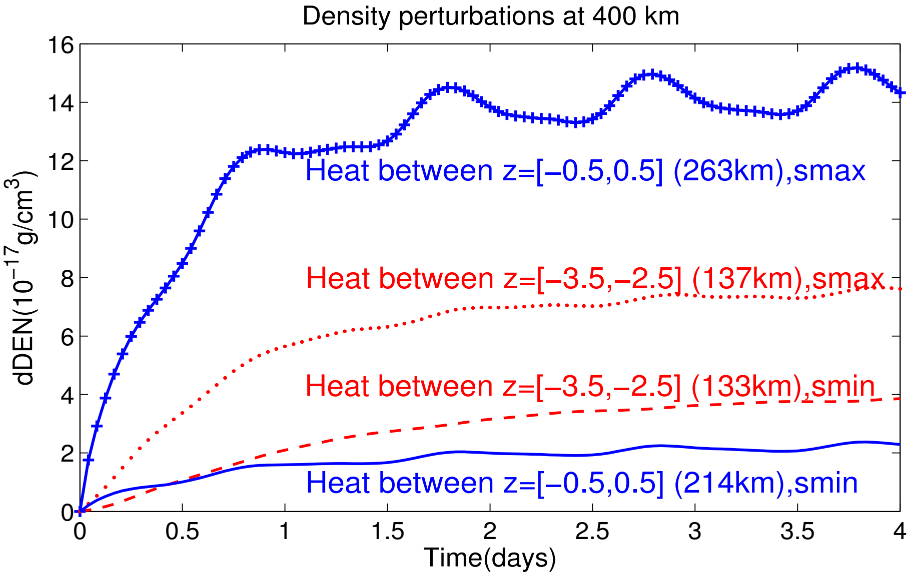

Figure 5.7. Temporal variation of globally averaged density perturbations at 400 km due to heat deposited in one scale height centered at pressure level 0 (blue lines) or -3 (red lines).

The density perturbation at 400 km due to Joule heating deposited in different altitudes is also examined. It peaks for heating deposited at ∼ 140 km (pressure level -3) for solar minimum and ∼ 263 km (pressure level 0) for solar maximum at 4 days, as illustrated in Figure 5.6, consistent with the results for temperature perturbations. There is a large difference in response between solar minimum and and solar maximum to the high-altitude heating, partly due to the greater *F*-region heating at solar maximum. Figure 5.7 depicts the density changes due to heat deposited in one scale height centered at pressure levels -3 and 0 at both solar minimum and maximum. At solar maximum, the high-altitude heating produces a larger density response than the low-altitude heating, while, at solar minimum, after around 20 hours, the low-altitude heating dominates the density response at 400 km, as was seen for the temperature perturbation.

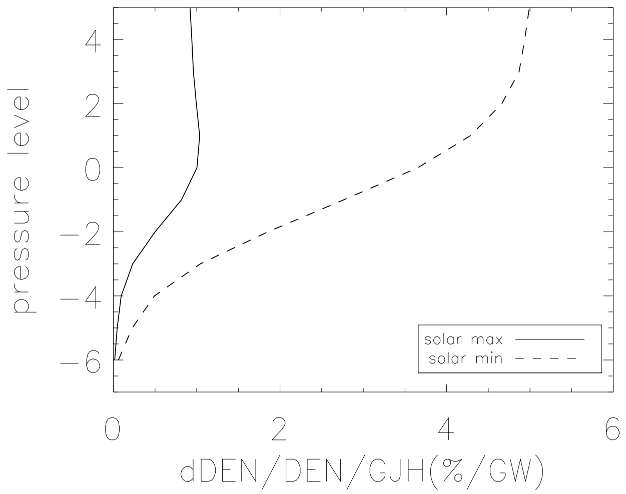

Figure 5.8. Percentage neutral density increase at 400 km per unit Joule heating input after 4 days. The solid line is for solar maximum and the dashed line is for solar minimum.

Furthermore, as for the temperature change, although Joule heating peaks at around 127 km, the density variation at 400 km peaks for heat deposited at much higher altitude (263 km) for the solar maximum case. For the solar minimum case, the heating above 150 km (18% of total energy) causes about 50% of the total density variation, while for the solar maximum case, it results in a 80% density variation due to 34% of the total energy. This result again indicates that the high-altitude Joule heating has a stronger impact on the atmosphere at 400 km. The efficiency of Joule heating in producing steady-state density variations at 400 km is also calculated, as shown in Figure 5.8. The curves tend to asymptote at high altitudes. This is because the heat deposited in the upper thermosphere is redistributed vertically very rapidly by heat conduction, so that heat deposited anywhere at high altitude has almost the same effect on the density.

5.3 One-Dimensional Model

To further evaluate the importance of the characteristic time scales shown in Figure 5.3, a simple one-dimensional (1D) model is employed. Since density disturbances originating in the polar regions reach the equator within about four hours, the basic physics of the thermospheric temperature and density changes can be illustrated with a 1D model representative of global-average conditions, for time scales of this order or longer. The 1D energy equation for a hydrostatic atmosphere, valid in regions above the turbopause (~ 110 km), can be written

$$\frac{\partial(c_p T)}{\partial t} - \frac{1}{\rho H}\frac{\partial}{\partial z}\left(\frac{\kappa}{H}\frac{\partial T}{\partial z}\right) = \frac{dQ}{dt} \tag{5.1}$$

where t is time, T is temperature, c_p is specific heat at constant pressure, ρ is density, H is pressure scale height, z is the dimensionless height coordinate $\ln(p_r/p)$, p is pressure, p_r is a constant reference pressure, κ is the coefficient of molecular heat conduction, and dQ/dt is the rate of net heat input per unit mass. An addition of heat per unit mass of the air δQ increases the specific enthalpy by an amount $c_p \delta T = \delta Q$.

The steady-state temperature, T_0, varies with z such that

$$-\frac{1}{\rho H}\frac{\partial}{\partial z}\left(\frac{\kappa}{H}\frac{\partial T_0}{\partial z}\right) = \frac{dQ_0}{dt}, \tag{5.2}$$

where dQ_0/dt is the steady-state net heating rate. For simplicity, let us assume that a temperature perturbation $\delta T = T - T_0$ causes a proportional change in radiative cooling, such that the perturbation in net heating due to radiation is

$$\frac{d\delta Q_r}{dt} = -\frac{c_p \delta T}{\tau_r}, \tag{5.3}$$

where τ_r is the radiative cooling time constant. τ_r can differ from the earlier definition due to the fact that the cooling rate is nonlinear with respect to temperature.

Let us consider a simple model in which c_p, κ/H, τ_r, and gravity g are constants. Then $\rho H = p/g$ varies as e^{-z}, and the equation for temperature perturbations becomes

$$\frac{\partial \delta T}{\partial t} - \frac{1}{\tau_\kappa}\frac{\partial^2 \delta T}{\partial z^2} + \frac{\delta T}{\tau_r} = \frac{1}{c_p}\frac{d\delta Q_J}{dt}, \tag{5.4}$$

$$\tau_\kappa = \frac{\rho c_p H^2}{\kappa} \tag{5.5}$$

where $d\delta Q_J/dt$ is the disturbance Joule heating rate.

Just as τ_r is a characteristic time scale for radiative cooling, τ_κ can be considered a characteristic time scale for heat conduction. τ_κ decreases with altitude roughly as $1/p$; in fact, under the assumptions of our simple model, τ_κ decreases with increasing z exactly as e^{-z}. At a given pressure level, τ_κ increases moderately with increasing temperature; while $\rho H = p/g$ is invariant on a pressure level, H increases with temperature more rapidly than κ.

Let us first consider a case where additional Joule heat δQ_J is deposited impulsively at time $t = 0$, with the vertical distribution

$$\delta Q_J = c_p \delta T_1 \exp\left(1 + z_1 - z - e^{z_1 - z}\right) \tag{5.6}$$

where δT_1 is the peak value of the temperature perturbation δT produced by this heat input, occurring at $z = z_1$ at $t = 0$. The black curve in Figure 5.9a shows

$\delta T/\delta T_1$ as a function of $z - z_1$ at $t = 0$. Let τ_1 be the value of τ_κ at z_1. The solution to Equation (4) for $t > 0$ is

$$\delta T = \delta T_1 f(z, t; z_1, \tau_r) \tag{5.7}$$

$$f(z, t; z_1, \tau_r) = \left[\frac{\tau_1^3 e^{z_1 - z}}{(\tau_1 + t)^3} - \frac{\tau_1^2}{(\tau_1 + t)^2} + \frac{\tau_1}{\tau_1 + t}\right] \exp\left(1 - \frac{\tau_1 e^{z_1 - z}}{\tau_1 + t} - \frac{t}{\tau_r}\right) \tag{5.8}$$

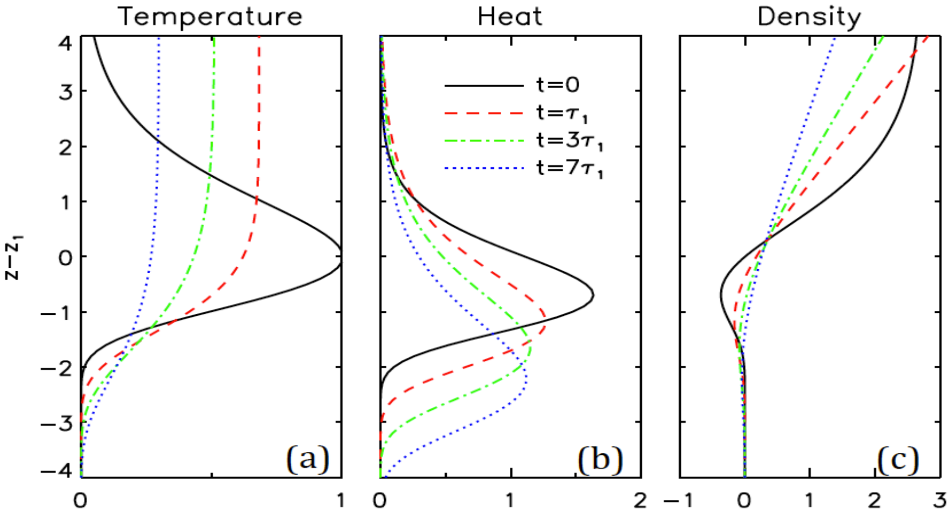

Figure 5.9. Perturbations of temperature and density from 1D model. (a)Temperature perturbation δT at various times, normalized by its value δT_1 at $z = z_1$ and $t = 0$. (b) Excess heat (enthalpy) content per unit area and per scale height, $\rho c_p H \delta T$, at various times, normalized by the value at $z = z_1$ and $t = 0$. (c) Fractional density perturbation at constant height, $\delta\rho/\rho_0$, normalized by $\delta T_1/T_0$.

Figure 5.9a shows this solution at times $t = 0$, $t = \tau_1$, $t = 3\tau_1$, and $t = 7\tau_1$, for the case where $\tau_r \gg \tau_1$, so that radiative cooling can be neglected. The relevant radiative cooling time scale is that for the height where most of the excess heat resides. Because the excess heat conducts downward with time, most of it resides below 150 km by the time radiative effects become significant. At these low altitudes, τ_r is on the order of 3-10 days. At $t = 0$, δT varies with z in the same manner as the input heat per unit mass δQ_J. The temperature perturbation expands upward relatively quickly, with time scale τ_1, to produce an approximately isothermal perturbation at higher altitudes that then decays in time. On the other hand, the temperature perturbation expands to lower altitudes much more slowly. Figure 5.9b shows the corresponding atmospheric energy perturbations expressed as excess enthalpy per unit horizontal area, per scale height in the vertical, as given by $\rho H c_p \delta T$. At $t = 0$ it maximizes 0.7 scale height below z_1 for this example. When integrated with respect to z it gives the total excess energy per unit area. If radiative loss is neglected, as in Figure 5.9b, this total energy is conserved as the excess heat conducts downward.

Density perturbations, which affect satellite drag, are most relevant at fixed heights rather than at fixed pressure levels. Assuming that $\delta T/T_0 \ll 1$, the fractional density change at a fixed height due to thermal expansion of the atmosphere below is $\int_{-\infty}^{z} (\delta T/T_0) dz'$ (neglecting changes of mean molecular mass), and the fractional density change due to local thermal expansion on a constant-pressure surface is $-\delta T/T_0$, so that the net fractional density change at a fixed height is

$$\frac{\delta\rho}{\rho_0} \approx \int_{-\infty}^{z} \frac{\delta T}{T_0} dz' - \frac{\delta T}{T_0}, \tag{5.9}$$

where ρ_0 is the unperturbed density and $\delta\rho$ is the density perturbation. Figure 5.9c shows the fractional density perturbations corresponding to the temperature perturbations in Figure 5.9a, assuming constant T_0. The relative density perturbation is negative toward the bottom of the region of perturbed temperature, but becomes positive above this region. After the high-altitude temperature becomes approximately isothermal, the high-altitude density perturbation increases exponentially with increasing height.

The characteristic time scale over which changes occur is τ_1, which is the heat conduction time scale at the height of maximum heating per unit mass, which is somewhat above (0.7 scale height in this case) the height of maximum heating per scale height. This time scale decreases exponentially with increasing z_1. At high altitude upward heat conduction causes both the temperature and density perturbations initially to increase with time, even though there is no further heat added to the atmosphere, before beginning to relax back toward zero. For this example, the high-altitude perturbations maximize at $t = \tau_1$. As time progresses beyond $t = \tau_1$, the perturbations at the higher altitudes decays approximately as $1/(\tau_1 + t)$, while the excess heat gradually moves to lower altitudes through conduction.

Let us now consider a heat source that turns on and stays on at $t = 0$, corresponding to the type of step-function change presented for the TIE-GCM simulations. Let us assume a vertical heating profile with the same shape as in the case above with impulsive heating:

$$\frac{dQ_J}{dt} = \left(\frac{dQ_J}{dt}\right)_1 \exp\left(1 + z_1 - z - e^{z_1 - z}\right) \tag{5.10}$$

for $t > 0$, where $(dQ_J/dt)_1$ is the peak heating rate per unit mass, occurring at $z = z_1$. The solution to Equation (4) for $t > 0$ is proportional to the time integral of (7):

$$\delta T = \frac{1}{c_p}\left(\frac{dQ_J}{dt}\right)_1 \int_0^t f(z, u; z_1, \tau_r) du \tag{5.11}$$

Figure 5.10 shows the temporal evolution of δT at $z = 3.7$ for heat inputs having $z_1 = -2.4$ or $z_1 = 0.6$, either with or without radiative cooling. Since z_1 is approximately 0.7 scale height above the midpoint of the heat input, the heating for these cases lies around $z = -3.1$ or $z = -0.1$, corresponding approximately to the heating altitudes used for Figures 4 and 7. We choose parameters representing conditions midway between minimum and maximum solar activity. The altitude for which δT is shown is then approximately 400 km. And the midpoint altitudes of the lower and higher heat inputs are approximately 135 km and 238 km. With reference

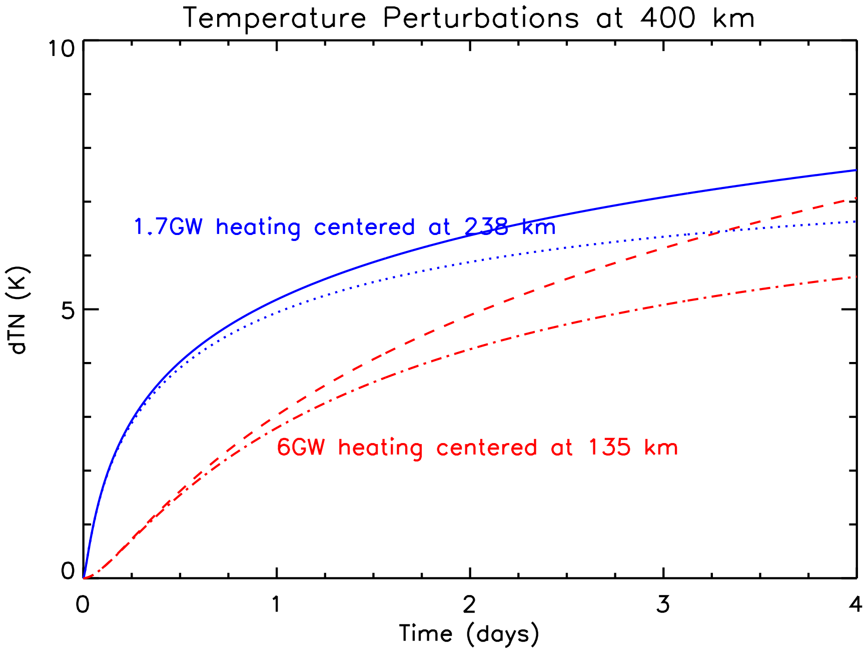

Figure 5.10. Temperature perturbations at 400 km due to heat deposited around 135 km or 238 km from the 1D model. Blue solid curve: high-altitude heating without radiative cooling. Blue dotted curve: high-altitude heating with radiative cooling. Red dashed curve: low-altitude heating without radiative cooling. Red dashed-dotted curve: low-altitude heating with radiative cooling. See text for details of model parameters used .

to Figure 5.3, the values of τ_1 are approximately 6 hours ($z_1 = -2.4$) or 0.5 hours ($z_1 = 0.6$). With reference to Figure 5.1, the global heating rates for the one-scale-height-thick layers centered at $z = -3$ and $z = 0$ are approximately 6 GW and 1.7 GW, respectively, for medium solar activity. If we equate these values to the global heating rate from our 1-D model, which is $4\pi R_E^2$ times the height integral of $\rho dQ_J/dt$, where R_E is the Earth radius and dQ_J/dt is given by (10), we find $(dQ_J/dt)_1$ values of 0.07 W/kg and 0.4 W/kg for the lower and upper layers, respectively, which are used for Figure 5.10. We use $c_p = 1100$ J/kg/K and a radiative time constant $\tau_r = 8$ days.

The curves in Figure 5.10 that include radiative cooling lie between the corrresponding solar-minimum and solar-maximum curves in Figure 4, indicating that the 1D model indeed represents the global average energetics reasonably well, in spite of its many simplifications. The high-altitude heating produces a rapid initial temperature response at 400 km that then slows, while the low-altitude heating produces a much slower initial temperature response that continues to grow for several days. Radiative cooling does not play a major role during the first few days. We might note that for times longer than a few days the heat will begin to conduct down to heights where turbulent heat conduction becomes important, and the heat will be removed from the upper altitudes more rapidly than this simple model predicts.

5.4 Conclusions

Studies of the thermospheric response to Joule heating cannot consider only the height-integrated heating, as approximated by the downward Poynting flux above the ionosphere, but must also consider how this heat is distributed in altitude. We conducted a detailed theoretical study on the altitudinal distribution of Joule heating and its influence on the thermosphere at satellite altitude for solar minimum and maximum conditions, using the latest version of the NCAR TIE-GCM. It is found that most of the Joule heating is deposited under 150 km, and the largest Joule heating deposition per scale height happens at about 125 km. However, the temperature and density changes at 400 km in steady state are largest for heat deposited at $\sim$140 km for solar minimum and $\sim$263 km for solar maximum. For solar minimum, the Joule heating above 150 km (18% of total heat) causes about 60% of the total temperature variation and 50% of the total density variation, while for solar maximum, it results in 90% of the temperature variation and 80% density variation due to 34% of the total heat. This indicates that the high-altitude Joule heating has a stronger impact on the atmosphere at 400 km.

The perturbation of the high-altitude thermosphere depends on the amount of heat deposited, on heat conduction and also on radiative cooling. At solar maximum, the temperature and density at 400 km respond most strongly to heating in the ionospheric *F* region, around pressure level 0 or height 263 km, for all time scales ranging from 3 hours to 4 days. In contrast, at solar minimum it is only for short time scales (∼3 hours) that the temperature and density at 400 km respond most strongly to *F*-region heating, around pressure level 0 or height 214 km, while the response on longer time scales becomes increasingly sensitive to heating in the upper *E* region, around pressure level -3 or height 140 km. This difference between solar minimum and maximum is due in large part to the relatively much greater *F*-region heating at solar maximum, but also to considerably stronger radiative cooling at solar maximum, in comparison with solar minimum.

The conduction time scale is much faster than the radiative cooling time scale at all heights, and radiative cooling is negligible for the short-time-scale response to heating, in comparison with heat conduction. Heat deposited at lower heights needs more time to conduct upward. The temperature at 400 km has some time delay to respond to the lower-level Joule heating, which indicates that the high-altitude heating is more important for a quick and intense (hours) Joule-heating event, while low-altitude Joule heating can become more important for long-term (days) variations, especially at solar minimum.

A simple one-dimensional time-dependent model is used to illustrate the effects of heat conduction and radiative cooling on the thermospheric response to Joule heating. The characteristic time scale for response is primarily the heat conduction time scale, which depends on the height of heat deposition, while radiative cooling becomes important only for longer time scales and is governed by the cooling rate at the lower altitudes, where most of the excess heat resides. An impulsive deposition of heat leads to rapid upward conduction and an initial temperature increase at high altitudes, followed by a slow decay, while conduction to lower altitudes proceeds much more slowly. Using a switch-on heating source at two different altitudes, with parameters corresponding to those from the TIE-GCM simulations, we find that the simple model can semi-quantitatively reproduce the principal features found in the global-average TIE-GCM results.

CHAPTER 6

SOLAR IRRADIANCE AND GEOMAGNETIC ENERGY INPUTS DURING LAST SOLAR CYCLE

6.1 Introduction

During the recent extended 23/24 solar cycle minimum, the solar irradiance, activity and interplanetary magnetic fields had reached levels lower than observed in past minima [35]. Consequently, the lowest observed thermospheric neutral density during 23/24 solar minimum decreased by 29% compared with 22/23 solar minimum after removing the seasonal and geomagnetic activity effects [24, 25]. [117] modeled a 30% decrease in the annual average neutral density from 1996 to 2008. Meanwhile, the global total electron content (TEC) from GPS observations showed a positive trend of 0.6 TEC per decade (1 TECU = $10^{16} elm^{-2}$) [55], while the f_0F_2 from ionosonde data was lower in 23/24 solar minimum than 22/23 at some locations [12, 60].

The record-low thermospheric density and the unusual variation of electron density during last solar minimum hav been mainly explained as the consequence of the anomalously low solar Extreme Ultraviolet (EUV) irradiance [24, 119, 117]. The variation of geomagnetic energy has received relatively less attention or has been treated as negligible [117, 12]. Actually, it is still in debate if the change of solar EUV irradiance is sufficient to cause the observed variation in the upper atmosphere or not. [24] showed that about 10% of neutral density difference is attributable to lower solar EUV irradiance and around 16% of the observed density difference remains unexplained. [117] reported that solar EUV irradiance change alone caused 22% annual average neutral density reduction. They found that combining the solar

EUV effect with the geomagnetic energy (2.2%) and CO_2 cooling (3%), totally 27% neutral density decrease can be explained, which is very close to the satellite observed value (30%). However, 15% lower solar irradiance in 2008 than in 1996 can result in a global TEC trend of 3 TECU per decade, which is much larger than the observation and can be implausible [55].

The Sun is the ultimate energy source for the upper atmosphere. Typically, the solar EUV irradiance is viewed as the direct solar source of energy deposition and the geomagnetic energy, including both Joule heating and particle precipitation energy, is treated as the indirect solar source, which is transported through the solar wind and magnetosphere [52, 150]. Given that the solar activity was extremely low in 23/24 solar minimum, both direct and indirect solar sources should vary accordingly and contribute to the change in the upper atmosphere. The globally averaged thermosphere mass density climatologically is a function of both solar irradiance and geomagnetic activity [25]. The total Joule heating from [141] model also shows a good correlation with the CHAMP and Grace satellite measurements [143]. It is very important to know how much energy was reduced in different forms between the last two solar minima, which is critical to explain the unusual variation in the upper atmosphere during 23/24 solar minimum. In this study, we have investigated the variation of the energy budget to the Earth's upper atmosphere from both solar EUV irradiance and geomagnetic energy (Joule heating and particle precipitation) during last solar cycle. Some idealized simulations from Thermosphere Ionosphere Electrodynamic General Circulation Model (TIE-GCM) have been conducted to illustrate their relative roles to the upper thermospheric neutral density variation.

6.2 Methodology

The EUV flux model for Aeronomic Calculations (EUVAC) [92, 116] has been used to calculate the solar power in the wavelength of 1 - 105 nm. EUVAC is based on the measured F74113 solar EUV reference spectrum and provides fluxes in the 37 wavelength bins that are in widespread use [92]. Individual bands and lines of solar EUV photon flux are calculated from a proxy based on the $F_{10.7}$ index and its 81-day average [117]. $F_{10.7}$ is the index of the 10.7 cm solar radio flux and widely used to represent the solar activity and EUV emissions. But [117, 12] reported some issues with $F_{10.7}$ during solar minimum conditions. The MgII core-to-wing ratio (c/w) is a good measure of solar chromospheric activity and a valuable proxy for solar EUV flux [117, 136]. After a linear fit of $F_{10.7}$ to MgII c/w, the $M_{10.7}$ index is calculated out from the equation (1) in [117], which is the MgII c/w scaled to $F_{10.7}$ with unit of 10^{-22} $\mathrm{Wm^{-2}Hz^{-1}}$. In this study, the solar EUV flux calculated from EUVAC model with both $F_{10.7}$ and $M_{10.7}$ indices is presented. The total solar EUV power is then estimated through multiplying the solar flux at 1 AU from EUVAC output with the cross section of Earth, $\pi \mathrm{R}^2$, where R is the Earth radius and typically set as 6600 km to include the contribution of the atmosphere. The measurements from the Solar EUV Experiment (SEE) [146] on the Thermosphere-Ionosphere- Mesosphere Energetics and Dynamics (TIMDE) satellite have been compared with the model outputs as well.

Joule heating has been calculated from the [141, 142] model (Weimer05), the empirical formula [28] and the Thermosphere Ionosphere Electrodynamics General Circulation Model (TIE-GCM) [107, 100]. Weimer05 is an empirical model of high-latitude electrodynamics, providing the electric potential, magnetic potential, field-aligned currents and Poynting flux. The downward Poynting flux at the top of ionosphere is obtained from the vector cross product of the electric and perturbation magnetic fields

$$S = \frac{E \times \Delta B}{\mu_0}, \tag{6.1}$$

[48, 33], which supplies one possible way to estimate the height-integrated Joule heating by application of Poynting's theorem [48, 96]. The empirical formula

$$Q_J(GW) \approx 4 + 20K_p, \tag{6.2}$$

from [28] gives a reasonable description of the single hemisphere Joule heating at the equinoxes for average conditions when $K_p < 6$. The global Joule heating is close to $2 \times \mathrm{Q}_J$ when ignoring the seasonal variations and the interhemispheric asymmetry. TIE-GCM is a global first-principle upper atmospheric model, which self-consistently simulates both the neutral and ion species. In the high latitudes, the electric potential pattern is imposed from [41] empirical model driven by the K_p index and the auroral particle precipitation is specified with the formalism of [104] for this study. The Joule heating has been calculated from the localized conductance, ion convection and neutral wind. A factor of 1.5 has been multiplied to Joule heating to compensate the contribution of small-scale processes.

The NOAA polar-orbiting operational environmental satellite (POES) continuously monitor the precipitating particles from 50 eV to 20 keV in the polar regions. A technique has been developed to estimate the total particle power deposited in the entire polar region, named as the hemispheric power (HP), from the particle power flux observations along a single satellite pass [31]. The NOAA HP data for each hemisphere during the whole solar cycle are available on the website (http://www.swpc.noaa.gov/ftpmenu/lists/hpi.html). The HP of TIE-GCM has been calculated from K_p-dependent empirical formulation based on TIMED/GUVI FUV data [153].

6.3 Results and Discussion

6.3.1 Solar EUV irradiance and geomagnetic energy variations

The primary energy sources of the upper atmosphere are the solar EUV irradiance, Joule heating and the particle precipitation, The solar EUV irradiance usually is the largest contributor (80%) to the heating budget, but Joule heating is the most variable one and exceeds the solar EUV irradiance power during some geomagnetic storm periods [62, 52]. We have examined how the different forms of energy varied between the last two solar minima.

Figure 6.1 depicts the 81-day centered running mean of the globally integrated solar EUV irradiance and geomagnetic energy during last solar cycle (1995 - 2009). The yellow shadow regions mark the 22/23 solar minimum in 1996 and 23/24 solar minimum in 2008. The top panel is the solar power in the wavelength of 0 - 105 nm calculated from EUVAC model driven by the $M_{10.7}$ index. The yearly average of solar power in 2008 was 300.6 GW, which was 33 GW (10%) lower than that in 1996 (333.6 GW). Due to the wavelength dependence of the solar irradiance, the overall percentage reduction in EUV (10%) was lower than that (15%) in the wavelength band of 26 - 34 nm measured by SOHO/SEM instrument [119]. The middle panel represents the globally integrated Joule heating from Weimer05 empirical model driven by the OMNI 2 hourly solar wind data. The quiet solar wind conditions:

$$B_y = B_z = 0, V_{sw} = 400km/s \tag{6.3}$$

have been filed in when there is a data gap in the OMNI 2 data. The typical Weimer05 output is a polar distribution of altitudinal integrated Joule heating in the northern hemisphere. To cover the southern hemisphere, Weimer05 was run with the same solar wind conditions but a flipped B_y value and a flipped dipole title angle, in which the inter-hemispheric asymmetry has been neglected. As illustrated in Figure

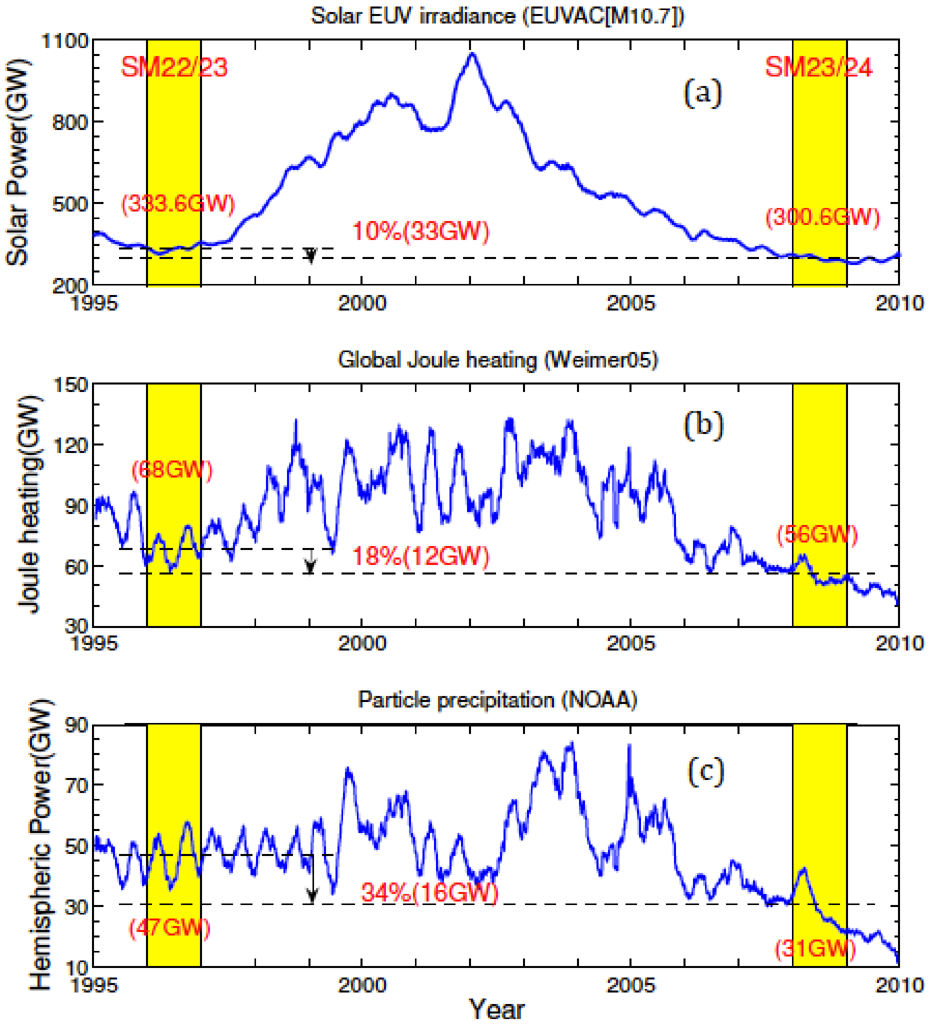

Figure 6.1. The 81-day running means of solar EUV irradiance and geomagnetic energy during last solar cycle (1995 - 2009). The yellow shadow regions mark the 22/23 solar minimum in 1996 and 23/24 solar minimum in 2008. (a) the solar power in the wavelength of 0- 105 nm calculated from EUVAC model. (b) the global integrated Joule heating from Weimer05 empirical model driven by the OMNI 2 solar wind data. (c) shows the global integrated particle precipitation energy from NOAA satellites measurements.

6.1, the globally integrated Joule heating was reduced by 13 GW (19%) from 1996 (67 GW) to 2008 (54 GW). The bottom panel shows that the globally integrated particle precipitation energy from NOAA satellite also decreased by 16 GW (34%)

in 2008. The total geomagnetic energy, including both Joule heating and particle precipitation energy, decreased by 29 GW (13 GW +16 GW), which was comparable with the reduction of the solar power (33 GW). It suggests that the contribution of geomagnetic energy variation to the neutral density reduction may not be negligible.

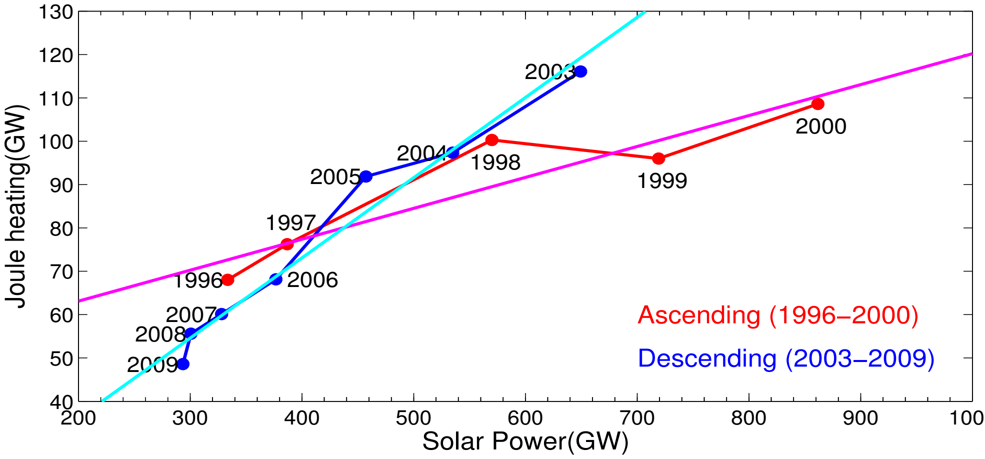

Figure 6.2. Comparison of the global integrated Joule heating annual averages to solar EUV power annual averages during solar cycle 23. Red lines, ascending phase (1996 - 2000); blue lines, descending phase (2003 - 2009). The magenta and light blue lines are the best linear fits for the ascending and descending phases.

Figure 6.2 compares the annual averages of the globally integrated Joule heating to the annual averages of the solar power from the EUVAC model driven by the $M_{10.7}$ index in both ascending and descending phases of the solar cycle. Clearly, both Joule heating and solar power in 2008 and 2009 were lower than those in 1996. The best linear fit is shown in magenta for ascending and light blue for descending. Since the large variation of Joule heating caused by the geomagnetic storms during solar maximum is out of the scope of this study, the points for the annual averages in 2000 - 2002 have been dropped out. In the ascending phase the slope was close to 0.07, which means the Joule heating increased by 0.07 GW for every 1 GW enhancement of the solar power. The slope for the descending phase was close to 0.18, which is more than two times higher than that in the ascending phase. In other words, the Joule heating changed relatively faster in the descending phase than the ascending phase. For example, from 1996 to 1997, the solar power and Joule heating increased by 53.3 GW and 5.4 GW, respectively. From 2008 to 2009, the solar power and Joule heating decreased by 7.1 GW and 6.8 GW, respectively. The variation of Joule heating was comparable with the variation of solar power from 2008 to 2009, while the variation of solar power was dominant in the total energy from 1996 to 1997. Therefore, the contribution of Joule heating variation to the total energy change in the descending phase was more significant than in the ascending phase.

6.3.2 Comparison of energy estimations from different sources

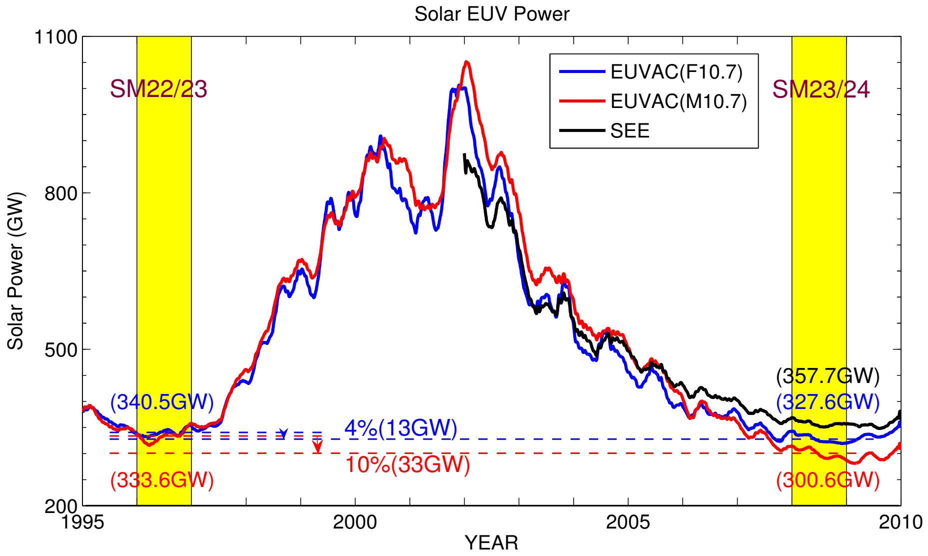

Figure 6.3. The same as Figure 1, but for the comparison of solar power from different sources including EUVAC driven by $F_{10.7}$ (Blue), EUVAC driven by $M_{10.7}$ (Red) and SEE measurements (Black). The annual averages in 1996 and 2008 and the difference between them have been marked.

The energy estimation uncertainty is one of the biggest problem in the upper atmosphere simulation. The solar power and Joule heating calculated from different models have therefore been compared in this section. Figure 6.3 shows the variation of solar power from EUVAC model and TIMED/SEE measurements during last solar cycle. The integrated EUV energy flux is derived from the EUVAC model using either $M_{10.7}$ or $F_{10.7}$ as input. The energy flux is normalized to 1 AU and not corrected for SUn-Earth distance, which is sufficient for this study since our main interest is the variation of yearly average.

As shown in red line, the yearly average of solar power in 2008 calculated from EUVAC ($M_{10.7}$) was 300.6 GW, which was reduced by 33 GW (10%) compared to the value in 1996 (333.6 GW). The blue line exhibits that the solar power reduction from 1996 to 2008 calculated from EUVAC ($F_{10.7}$) was close to 13 GW (4%). The change of the solar power calculated from $F_{10.7}$ index was smaller than that from $M_{10.7}$ index, which was due to the inaccuracy of $F_{10.7}$ to present the solar EUV power in the extreme low solar activity conditions during 23/24 solar minimum [117, 12]. As shown in [117], during solar minimum the $F_{10.7}$ variation was small while the solar EUV continued to decline. The measurements from SEE [146] on the TIMED satellite from 2002 to 2009 have also been plotted out in black line, which in general agreed very well with the EUVAC outputs. TIMED/SEE was smaller than EUVAC in solar maximum and larger in solar minimum. Due to the way that the irradiance ¡ 27 nm was processed, the total solar power from TIMED/SEE data can be different from version, which may contribute to the solar-cycle dependent difference between TIMED/SEE and EUVAC. From 27 to 105 nm, TIMED/SEE is based on EGS (EUV Grating Spectrometer) measurements, which are quite reliable [146]. Unfortunately, TIMED/SS does not go back to 1996 and has no comparison between the two solar minima.

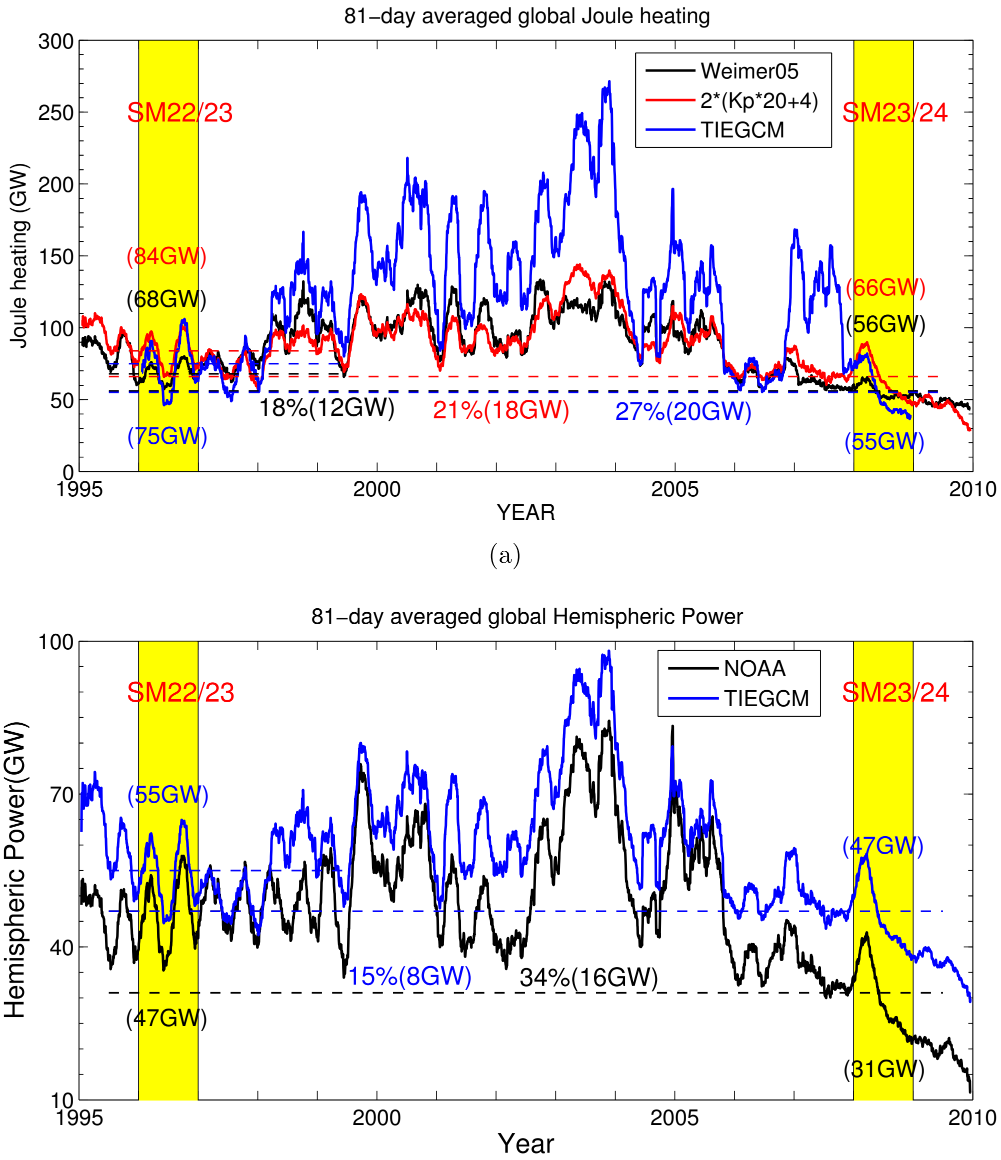

(a)

(b)

Figure 6.4. Comparison of 81-day averaged geomagnetic energy inputs. (a) The same as Figure 6.3, but for the comparison of global integrated Joule heating from different sources including Weimer05 (Black), empirical formula (Red) and TIEGCM (Blue). (b) The same as (a), but for the comparison of the total hemispheric power from NOAA (Black) and TIEGCM (Blue).

The geomagnetic energy inputs into the upper atmosphere vary significantly [62, 53] and it is very challenging to estimate them precisely. Figure 6.4(a) shows the calculated globally integrated Joule heating from Weimer05, empirical relationship between the global Joule heating and K_p index

$$JH = (20 \times K_p + 4) \times 2 \tag{6.4}$$

[28] and TIE-GCM. The annual average difference of Joule heating between 1996 and 2008 was 13 GW from Weimer05, 18 GW from empirical formula, and 20 GW from TIE-GCM. The estimate of Joule heating variation is limited by many processes, such as the inaccuracy of K_p index to describe the geomagnetic activity in the extreme quiet conditions during solar minimum 23/24. The Joule heating calculated from Weimer05 is influenced by the solar wind data gaps in the OMNI 2 data set and the limited capability of Weimer05 to describe the electrodynamics during northward IMF conditions, such as the floor (25 kV) of the Cross Polar Cap Potential (CPCP) [140]. The hemispheric power from NOAA measurement and TIE-GCM has been compared as well. Based on TIMED/GUVI FUV data, a global auroral model has been developed [153] and a K_p-dependent empirical formulation of the HP has been produced. Similar formulas have been utilized in TIE-GCM to calculate HP from K_p index [75]. As shown in Figure 6.4(b), HP from the empirical formulas in TIE-GCM is in general higher than NOAA HP, which has also been reported in [153] and may be related to the difference of the data coverage. While the HPs are estimated from both NOAA and TIMED/GUVI satellite data, the NOAA satellite tracks just cover a tiny fraction of the auroral oval and the TIMED/GUVI swath typically covers 1/3 to 1/2 of the auroral oval [153]. The difference of HP between the two solar minima is 16 GW and 8 GW in NOAA measurements and TIE-GCM., respectively. While the Joule heating reduction varied from 13 to 20 GW and the HP reduction also changed from 8 to 16 GW, all these sources consistently exhibited a decrease of geomagnetic energy during 23/24 solar minimum.

Weimer05 is an empirical model, which represents a climatologic distribution of the high-latitude electrodynamics. Figure 6.5 depicts the 81-day average of the northern hemispheric integrated Joule heating in 2005 from both Weimer05 and the Assimilative Mapping of Ionospheric Electrodynamics (AMIE) [97] outputs. In AMIE run, more than 80 ground-based magnetometers and DMSP satellite electric drift measurements have been assimilated. Since the data coverage in the southern hemisphere was not as good as the northern hemisphere, only the northern hemispheric integrated Joule heating has been compared. While the difference between these two models varied with the season, Weimer05 was consistently smaller than AMIE and the yearly averaged Joule heating from AMIE (85 GW) was almost two times larger than that from Weimer05 (46 GW). If the factor of two is kept for the whole solar cycle, the Joule heating difference between 1996 and 2008 from AMIE may also double the value from Weimer05 and reach 26 GW (2 × 13 GW). Certainly, more

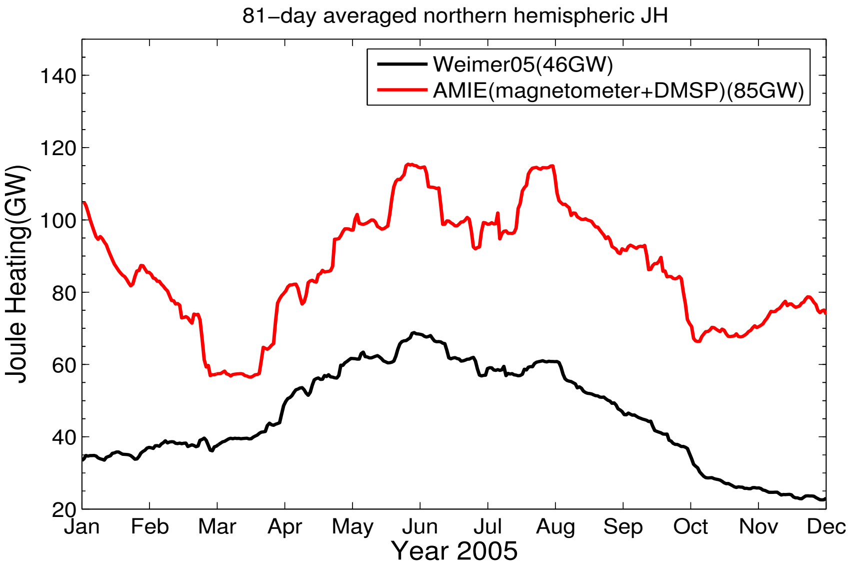

Figure 6.5. Comparison of the northern hemispherical integrated Joule heating between Weimer05 and AMIE during year 2005. The annual average values from both models are indicated in the legend.

comprehensive study using the AMIE outputs during the whole solar cycle is needed to reach a general conclusion.

6.3.3 Influence on the neutral density

The total energy powers just gives us a rough idea of the significance to the upper atmosphere, and the energy distribution and the heating efficiency are also critical to explain the upper atmosphere variations [96, 18]. Clearly, the solar irradiance, Joule heating and particle precipitation have very different horizontal as well as vertical distributions [31, 131, 53]. Meanwhile, their heating efficiencies to the thermosphere are quite different. The heating efficiency of solar EUV is roughly 50% [134], but Joule heating transfers the energy almost entirely to the neutral atmosphere [131, 53]. Due to these differences, the effects of the solar irradiance and Joule heating on the upper atmosphere can be different even though the same amount of energy has been deposited.

To investigate the relative contributions of solar EUV and geomagnetic energy to thermospheric density reduction, some idealized simulations have been conducted. The TIE-GCM does a reasonable job of tracing the satellite drag measurements of the neutral density [117] and has been employed for three different cases during both 1996 and 2008: case 1 with variable K_p and $M_{10.7}$ (black line in Figure 6.6), case 2 with a constant K_p of 0.5 and variable $M_{10.7}$ (red line in Figure 6.6) and case 3 with variable K_p and a constant $M_{10.7}$ of 56 (blue line in Figure 6.6). Case 1 represents a full simulation including the change of both geomagnetic activity and solar EUV irradiance. At 400 km altitude, the annual average density is 0.76 ng/m^3 in 1996 and 0.56 ng/m^3 in 2008. The total neutral density reduction is equal to 0.02 ng/m^3 (26%). In case 2 when K_p is a constant (0.5), the variation of the geomagnetic energy has been eliminated and the globally integrated Joule heating is close to 19

GW and the total HP is 29.7 GW. The yearly average density decreased from 0.61 ng/m^3 in 1996 to 0.46 ng/m^3 in 2008 and the neutral density reduction is 0.15 ng/m^3. The 0.15 ng/m^3 density change is due to the solar irradiance variation and accounts for 3/4 of the total density reduction (0.20 ng/m^3). In case 3, $M_{10.7}$ is set to be a constant (56). The variation of the solar irradiance has been eliminated and the solar power is close to 276 GW. The yearly averaged density is reduced from 0.50 ng/m^3 in 1996 to 0.44 ng/m^3 in 2008 at 400 km and the neutral density reduction is 0.06 ng/m^3. This 0.06 ng/m^3 density decrease represents the contribution of the

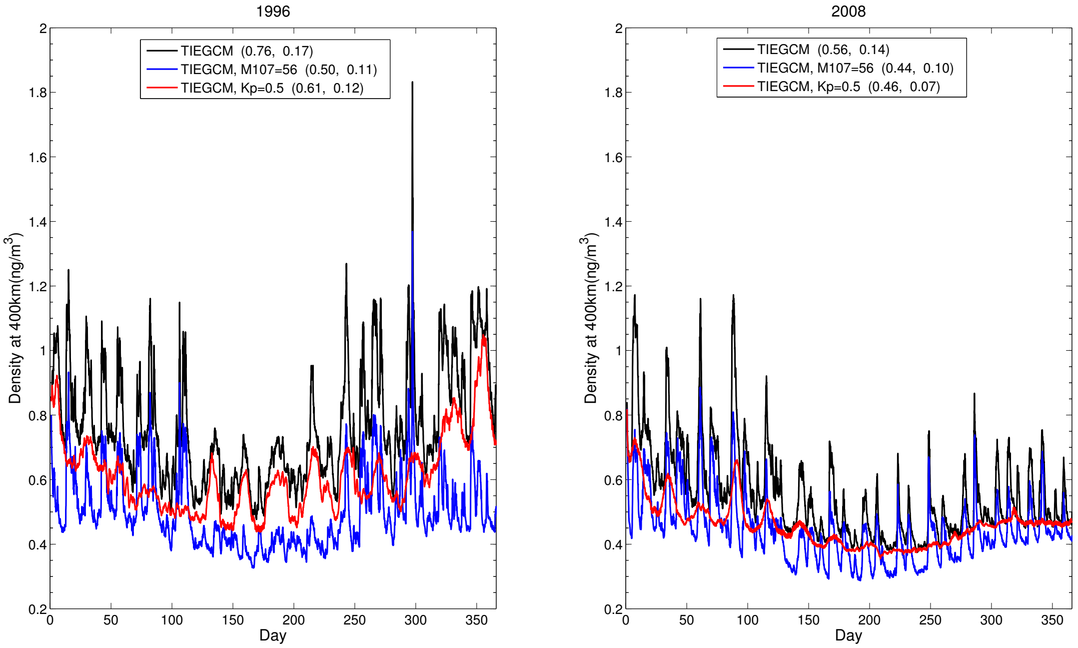

(a) (b)

Figure 6.6. Results of TIE-GCM simulations. The TIEGCM simulated daily global mean neutral density at 400 km for 1996 (a) and 2008 (b) using $M_{10.7}$ index for the solar irradiance and K_p index for the geomagnetic energy. Black lines, both $M_{10.7}$ and Kp change with time; blue lines, $M_{10.7}$ is a constant value of 56; red lines, K_p is a constant value of 0.5. The yearly mean and standard deviation for each case have been indicated in the legend.

geomagnetic energy change and is close to 1/4 of the total density change. While the change of the total geomagnetic energy (29 GW) between 1996 and 2008 is comparable to that of solar power (33 GW), the influence of geomagnetic energy to the neutral density at 400 km is almost three times smaller than the solar power (0.06 ng/m^3 versus 0.15 ng/m^3). This difference is related to the energy distribution and heating efficiency. For example, the altitudinal distribution of these two energy deposition is quite different. The solar irradiance peaks around 150 km altitude and the Joule heating usually maximizes at 120 km. The effective height of solar irradiance is higher than that of Joule heating. The solar irradiance is therefore more efficient to heat up the upper thermosphere at 400 km than Joule heating [18, 44].

As illustrated in Figure 6.6, the temporal variation of the neutral density during these two years are quite different. In case 2 with a constant K_p, the simulation displays a repeatable 27-day cycle after DOY 120 in 1996, which is related to the Sun rotation period and corona hole structure on the SUn during that time. On contrast, in 2008 after DOY 150, the red line is very smooth with little variation, which indicates the solar power has not changed much. The standard deviation of the red lines representing neutral density variation caused by the solar irradiance variation is 0.12 and 0.07 n 1996 and 2008, respectively. Therefore, the solar irradiance in 1996 is not only averagely higher, but also more variable than that in 2008. In case 3, when the $M_{10.7}$ is constant, the geomagnetic energy contributes significantly to the temporal variation of neutral density, such as the neutral density spike during the geomagnetic storm on DOY 297 in 1996 and neutral density oscillation during both 1996 and 2008. The neutral density minimum happens around DOY 200 in both years, which is related to the semi-annual variation and the inter-hemispheric asymmetry. Due to the semi-annual variation, the neutral density has minima in summer and winter solstices. Meanwhile, the southern hemisphere has a much stronger semi-annual variation than the northern hemisphere and dominates the global density variation. Around DOY 200, the southern hemisphere is winter and has the lowest neutral density. The result is consistent with the CHAMP satellite measured neutral density annual variation at 400 km during 2002 - 2007 [1].

6.4 Conclusion

The solar activity during 23/24 solar minimum reached levels lower than past minima. Consequently, the record-low thermospheric density and unusual ionospheric density variation during last solar minimum have been reported, which have been mainly explained as the consequence of the anomalously low solar EUV irradiance. On contrast, the variation of geomagnetic energy has been paid relatively less attention or has been treated negligible. Actually, the Sun is the ultimate energy sources for the upper atmosphere and the solar irradiance and the geomagnetic energy have been thought as the direct and indirect solar sources of energy deposition in the upper atmosphere. When the Sun activity was extremely low in 23/24 solar minimum, both direct and indirect solar sources should vary accordingly. The energy reduction in different forms is critical to explain the unusual variations in the upper atmosphere during 23/24 minimum. In this study, we examined the energy budget to Earth's upper atmosphere during last solar cycle from both solar EUV irradiance and geomagnetic energy, including Joule heating and particle precipitation. The solar EUV power in 2008 calculated from the EUVAC model was reduced by 33 GW compared to 1996. The reduction of the total geomagnetic energy was close to 29 GW including 13 GW for Joule heating from Weimer05 and 16 GW for particle precipitation from NOAA satellite measurements. While the estimations of the solar EUV power and geomagnetic energy vary from model to model, the change of the geomagnetic energy from 1996 to 2008 was comparable to that of the solar EUV power. The idealized simulations with TIE-GCM indicate that the variation of the solar irradiance and the geomagnetic energy accounts for 3/4 and 1/4 of the total neutral density reduction in 2008, respectively.

CHAPTER 7

CONCLUSIONS AND REMARKS

In this dissertation, we have investigated the primary energy sources of Earth's upper atmosphere including the solar irradiance and geomagnetic energy (Joule heating and particle precipitation), and their impacts on the coupled thermosphere - ionosphere system using different data (OMNI2, CHAMP, DMSP) and models (SOLAR2000, FISM, Weimer05, AMIE, NCAR TIE-GCM). We focus on the wavelength dependence of solar irradiance enhancement during flare events, the geomagnetic energy associated with high-speed solar wind streams, the altitudinal distribution of Joule heating in different solar conditions, and the variation of solar irradiance and geomagnetic energy inputs during last solar cycle.

The solar irradiance is the direct solar source of energy deposition and is usually the largest contributor to the energy budget of the upper atmosphere. Solar irradiance at different wavelengths has different magnitudes, durations and energy deposition heights during flares. The wavelength dependence of solar flare enhancement is one of the important factors determining how the terrestrial atmosphere response to flares. The Flare Irradiance Spectral Model (FISM) data show that the solar irradiance enhancement between the flare peak to the pre-flare condition has wavelength dependence for the 61 X-class solar flares between year 1989 and 2012. In the wavelength range between 0 - 190 nm, the percentage increase varies a lot from 1% to 10000%. The solar irradiance increased largest in the XUV range (0 - 25 nm), about 1000% on average, and increased about 100% in EUV range (25 - 120 nm). The thermospheric response to different wavebands of solar irradiance has been investigated for one of the strongest flare events on October 28^{th}, 2003 (X17.2). The incoming solar flux in XUV range (0 - 14 nm) was quite small before flare compared to EUV (25 - 105 nm) and FUV ranges (122 - 190 nm), but it increased most during flare. Consequently, the globally integrated solar heating (GISH) was largest in the XUV range. The impact of solar irradiance enhancement on the high-altitude thermosphere (400 km) is however largest in the EUV wavebands, which accounts for about 33 K temperature enhancement in total 45 K, and about 7.4% in total 11% neutral density enhancement. The effect of irradiance in FUV wavebands is small in magnitude, but decays slowly.

The geomagnetic energy, including both Joule heating and particle precipitation energy, is viewed as the indirect solar source, which is transported through the solar wind and deposited into the magnetosphere/ionosphere/thermosphere system. We have investigated the energy transfer processes into the upper atmosphere associated with high-speed solar wind stream in year 2005. A 9-day periodicity was found in the upper atmosphere in year 2005 that is consistent with a similar periodicity present in the solar wind speed. The Lomb-Scargle periodograms of Joule heating, cross polar cap potential (CPCP), hemispheric power (HP) and D_{st} index from Assimilative mapping of ionospheric electrodynamics (AMIE) model outputs also have clear peaks at 9 days. The presence of 9-day periodic oscillation in integrated Joule heating is demonstrated for the first time in this study. The strong correlation of the 9-day oscillation in Joule heating and particle precipitation to the variation in neutral density suggests that the energy transfer processes into the upper atmosphere associated with high-speed solar wind stream is a combination of Joule heating and particle precipitation, while Joule heating may play a more important role. The sensitivities of Joule heating and HP to the solar wind speed are about 0.40 GW/(km/s) and 0.15 GW/(km/s). When the solar wind changes from low-speed stream to high-speed stream, Joule heating and HP increase by 120 GW and 45 GW, respectively, which indicates that the high-speed solar wind streams roughly double the quiet time magnetospheric energy inputs into the upper atmosphere and cause global variations.

The capability of electrodynamic models representing the variations of ionospheric forcing related to the solar wind conditions varies. The CPCPs and northern hemisphere integrated Joule heating (IJH) calculated from different sources are compared for year 2005. We have collected a year of convection data from two DMSP satellites (F13 and F15), and yearly runs of the empirical model Weimer05 and two different inputs to the data assimilative model AMIE, one assimilating only the ground-based magnetometers (AMIE 1), the other assimilating both the magnetometer data and DMSP convection data (AMIE 2). The yearly averaged CPCPs from Weimer05 and AMIE 1 are very close whereas the yearly averaged CPCP from AMIE 2 is about 11% larger than that from Weimer05, and 15% larger than that from AMIE 1. The IJH from AMIE 1 is about 41% larger than that from Weimer05, and the IJH from AMIE 2 is about 85% large than that from Weimer05, and 31% larger than that from AMIE 1 on average. The potential drop measured by DMSP satellite F13 shows a clear seasonal variation, with summer less than winter, while CPCPs from other sources have larger values in summer. And for all the sources, IJHs are relatively larger in summer than in winter because of the additional solar conductance. Corresponding to the 9-day periodicity in solar wind speed, CPCPs and IJHs from different sources present dominant 9-day period peaks in the Lomb-Scargle spectra. The sensitivity of IJH to solar wind speed is investigated utilizing a bandpass filter from 6 to 12 days centered at 9 day. The variation of IJH shows a positive dependence on the variation of solar wind speed from all sources. However, the sensitivities of IJHs from AMIE 1 and 2 are about 2.2 and 2.4 times larger than that from Weimer05, respectively. Further study of the IJH dependence on solar wind dynamic pressure

Pd, $|B|$ and $|B|V^2$ consistently shows that IJHs from AMIE 1 and 2 have sensitivities about 2.2 and 2.4 times larger than that from Weimer05.

Studies of the thermospheric response to Joule heating should consider not only the height-integrated heating, as approximated by the downward Poynting flux above the ionosphere, but also how this heat is distributed in altitude. We have conducted a detailed theoretical study on the altitudinal distribution of Joule heating and its influence on the thermosphere at satellite altitude for both solar minimum and maximum conditions using the latest version of the National Center for Atmospheric Research (NCAR) Thermosphere-Ionosphere-Electrodynamics General Circulation Model (TIE-GCM). Most of the Joule heating is deposited under 150 km, and the largest Joule heating deposition per scale height happens at about 125 km. However, the temperature and density changes at 400 km are largest for heat deposited at $\sim$140 km for solar minimum and $\sim$263 km for solar maximum. For solar minimum, the Joule heating above 150 km (18% of total heat) causes about 60% of the total temperature variation and 50% of the total density variation, while for solar maximum, it results in 90% of the temperature variation and 80% density variation due to 34% of the total heat. This indicates that high-altitude Joule heating has a stronger impact on the atmosphere at 400 km. Since heat deposited at lower heights needs more time to conduct upward, the temperature at 400 km has some time delay to respond to the lower-level Joule heating, which indicates that the high-altitude heating is more important for a quick and intense (hours) Joule-heating event, while low-altitude Joule heating can become more important for long-term (days) variations.

The globally averaged thermosphere mass density climatologically is a function of both solar irradiance and geomagnetic activity. However, the contribution of geomagnetic energy has received relatively less attention or has been treated as negligible compared to the solar irradiance. The record-low thermospheric density and unusual ionospheric density variation during last solar minimum in year 2008 have been reported, which have been mainly explained as the consequence of the anomalously low solar EUV irradiance. Given that the solar activity was extremely low in 23/24 solar minimum, both direct and indirect solar sources should vary accordingly and contribute to the change in the upper atmosphere. The energy reduction in different forms is critical to explain the unusual variations in the upper atmosphere during 23/24 minimum. We have examined the energy budget to Earth's upper atmosphere during last solar cycle from both solar EUV irradiance and geomagnetic energy, including Joule heating and particle precipitation. The solar EUV power in 2008 calculated from the EUV flux model for Aeronomic Calculations (EUVAC) model was reduced by 33 GW compared to 1996. The reduction of the total geomagnetic energy was close to 29 GW including 13 GW for Joule heating from Weimer05 and 16 GW for particle precipitation from NOAA satellite measurements. While the estimations of the solar EUV power and geomagnetic energy vary from model to model, the change of the geomagnetic energy from 1996 to 2008 was comparable to that of the solar EUV power. The TIE-GCM simulations indicate that the variation of the solar irradiance and the geomagnetic energy accounts for 3/4 and 1/4 of the total neutral density reduction in 2008, respectively.

The main external forcing of the thermosphere-ionosphere (T-I) system includes the solar irradiance, geomagnetic energy inputs, and waves propagating from lower atmosphere. In this dissertation, we have focused on the first two, but it is also important to continue the study of low-altitude driver of the T-I system utilizing the observational data and models like the Thermosphere-Ionosphere-Mesosphere-Electrodynamics General Circulation Model (TIME-GCM). Further studies will focus on the propagation of waves through T-I system and their impact on the high-altitude thermosphere using observations from Challenging Minisatellite Payload (CHAMP) spacecraft, Gravity Recovery And Climate Experiment (GRACE) and Communications/Navigation Outage Forecasting System (C/NOFS) during the period for extreme solar minimum in year 2008.

As we proceed into the solar maximum, we will continue our investigation of the effect of geomagnetic activity on the thermosphere during storm periods, utilizing extensive accelerometer data available through an entire solar cycle. Thermospheric observations were obtained from the accelerometers on GRACE and CHAMP spacecraft, which will provide the altitude profiles of thermospheric density. The results will compare with empirical models based on diffusive equilibrium, and also with the NCAR Thermosphere Ionosphere Mesosphere Electrodynamics General Circulation Model (TIME-GCM).

REFERENCES

[1] E. A, A. J. Ridley, D. Zhang, and Z. Xiao. Analyzing the hemispheric asymmetry in the thermospheric density response to geomagnetic storms. *Journal of Geophysical Research (SpacePhysics)* , 117:8317, August 2012.

[2] C. A. Barth, G. Lu, and R. G. Roble. Joule heating and nitric oxide in the thermosphere. *Journal of Geophysical Research (SpacePhysics)* , 114:5301, May 2009.

[3] J. G. Beck. A comparison of differential rotation measurements - (Invited Review). *Sol.Phys.* , 191:47–70, January 2000.

[4] B. M. Bein, S. Berkebile-Stoiser, A. M. Veronig, M. Temmer, and B. Vršnak. Impulsive Acceleration of Coronal Mass Ejections. II. Relation to Soft X-Ray Flares and Filament Eruptions. *ApJ* , 755:44, August 2012.

[5] J. W. Belcher and L. Davis, Jr. Large-amplitude Alfvén waves in the interplanetary medium, 2. *Journal of Geophysical Research (SpacePhysics)* , 76:3534, 1971.

[6] L. Biermann, B. Brosowski, and H. U. Schmidt. The interactions of the solar wind with a comet. *Sol.Phys.* , 1:254–284, March 1967.

[7] W. H. Campbell. *Introduction to Geomagnetic Fields*. 1997.

[8] P. C. Chamberlin, R. O. Milligan, and T. N. Woods. Thermal Evolution and Radiative Output of Solar Flares Observed by the EUV Variability Experiment (EVE). *Sol.Phys.* , 279:23–42, July 2012.

[9] P. C. Chamberlin, T. N. Woods, and F. G. Eparvier. Flare Irradiance Spectral Model (FISM): Daily component algorithms and results. *Space Weather* , 5:7005, July 2007.

[10] P. C. Chamberlin, T. N. Woods, and F. G. Eparvier. Flare Irradiance Spectral Model (FISM): Flare component algorithms and results. *Space Weather* , 6:5001, May 2008.

[11] S. Chapman and R. Lindzen. *Atmospheric tides. Thermal and gravitational.* 1970.

[12] Y. Chen, L. Liu, and W. Wan. Does the $F_{10.7}$ index correctly describe solar EUV flux during the deep solar minimum of 2007-2009? *Journal of Geophysical Research (SpacePhysics)* , 116:4304, April 2011.

[13] R. B. Cosgrove, G. Lu, H. Bahcivan, T. Matsuo, C. J. Heinselman, and M. A. McCready. Comparison of AMIE-modeled and Sondrestrom-measured Joule heating: A study in model resolution and electric field-conductivity correlation. *Journal of Geophysical Research (SpacePhysics)* , 114:4316, April 2009.

[14] T. G. Cowling. On the Sun's general magnetic field. *MNRAS* , 105:166, 1945.

[15] T. E. Cravens, editor. *Physics of solar system plasmas /Thomas E. Cravens. Cambridge : Cambridge*, 1997.

[16] G. Crowley, A. Reynolds, J. P. Thayer, J. Lei, L. J. Paxton, A. B. Christensen, Y. Zhang, R. R. Meier, and D. J. Strickland. Periodic modulations in thermospheric composition by solar wind high speed streams. *Geophysical Research Letters* , 35:21106, November 2008.

[17] Y. Deng, T. J. Fuller-Rowell, R. A. Akmaev, and A. J. Ridley. Impact of the altitudinal Joule heating distribution on the thermosphere. *Journal of Geophysical Research (SpacePhysics)* , 116:5313, May 2011.

[18] Y. Deng, Y. Huang, J. Lei, A. J. Ridley, R. Lopez, and J. Thayer. Energy input into the upper atmosphere associated with high-speed solar wind streams in 2005. *Journal of Geophysical Research (Space Physics)*, 116:5303, May 2011.

[19] Y. Deng, A. Maute, A. D. Richmond, and R. G. Roble. Analysis of thermospheric response to magnetospheric inputs. *Journal of Geophysical Research* (*SpacePhysics*) , 113:4301, April 2008.

[20] Y. Deng, A. Maute, A. D. Richmond, and R. G. Roble. Impact of electric field variability on Joule heating and thermospheric temperature and density. *Geophysical Research Letters* , 36:8105, April 2009.

[21] R. E. Dickinson, E. C. Ridley, and R. G. Roble. Thermospheric general circulation with coupled dynamics and composition. *Journal of Atmospheric Sciences*, 41:205–219, January 1984.

[22] J. A. Eddy. The Maunder Minimum - A reappraisal. *Sol.Phys.* , 89:195–207, November 1983.

[23] B. A. Emery, I. G. Richardson, D. S. Evans, and F. J. Rich. Solar wind structure sources and periodicities of auroral electron power over three solar cycles. *Journal of Atmospheric and Solar-Terrestrial Physics*, 71:1157–1175, July 2009.

[24] J. T. Emmert, J. L. Lean, and J. M. Picone. Record-low thermospheric density during the 2008 solar minimum. *Geophysical Research Letters* , 37:12102, June 2010.

[25] J. T. Emmert and J. M. Picone. Climatology of globally averaged thermospheric mass density. *Journal of Geophysical Research* (*SpacePhysics*) , 115:9326, September 2010.

[26] F. G. Eparvier, T. N. Woods, G. J. Ucker, and D. L. Woodraska. TIMED solar EUV experiment: preflight calibration results for the EUV grating spec-

trograph. In O. H. Siegmund, S. Fineschi, and M. A. Gummin, editors, *Society of Photo-Optical Instrumentation Engineers (SPIE) Conference Series*, volume 4498 of *Society of Photo-Optical Instrumentation Engineers (SPIE) Conference Series*, pages 91–100, December 2001.

[27] D. S. Evans, T. J. Fuller-Rowell, S. Maeda, and J. Foster. Specification of the Heat input to the thermosphere from magnospheric processes using the TIROS/NOAA auroral particle observations. *in Proceedings of the AAS/AIAA Astrodynamics Conference*, pages 1649–1668, 1987.

[28] J. C. Foster, J.-P. St.-Maurice, and V. J. Abreu. Joule heating at high latitudes. *Journal of Geophysical Research (SpacePhysics)* , 88:4885–4897, June 1983.

[29] P. Foukal. *Solar astrophysics.* 1990.

[30] T. J. Fuller-Rowell. The "thermospheric spoon": A mechanism for the semi-annual density variation. *Journal of Geophysical Research (SpacePhysics)* , 103:3951–3956, March 1998.

[31] T. J. Fuller-Rowell and D. S. Evans. Height-integrated Pedersen and Hall conductivity patterns inferred from the TIROS-NOAA satellite data. *Journal of Geophysical Research (SpacePhysics)* , 92:7606–7618, July 1987.

[32] H. A. Garcia. Thermal-Spatial Analysis of Medium and Large Solar Flares, 1976 to 1996. *ApJS* , 127:189–210, March 2000.

[33] J. B. Gary, R. A. Heelis, and J. P. Thayer. Summary of field-aligned Poynting flux observations from DE 2. *Geophysical Research Letters* , 22:1861–1864, 1995.

[34] P. R. Gazis. Limits on longitudinal asymmetries and deceleration of the solar wind in the outer heliosphere . *AIP Conference Proceedings*, 1996.

[35] S. E. Gibson, G. de Toma, B. Emery, P. Riley, L. Zhao, Y. Elsworth, R. J. Leamon, J. Lei, S. McIntosh, R. A. Mewaldt, B. J. Thompson, and D. Webb.

The Whole Heliosphere Interval in the Context of a Long and Structured Solar Minimum: An Overview from Sun to Earth. *Sol.Phys.* , 274:5–27, December 2011.

[36] S. E. Gibson, J. U. Kozyra, G. de Toma, B. A. Emery, T. Onsager, and B. J. Thompson. If the Sun is so quiet, why is the Earth ringing? A comparison of two solar minimum intervals. *Journal of Geophysical Research (SpacePhysics)* , 114:9105, September 2009.

[37] T. I. Gombosi, editor. *Physics of the space environment*, 1998.

[38] J. K. Hargreaves. *The solar-terrestrial environment. an introduction to geospace - the science of the terrestrial upper atmosphere, ionosphere and magnetosphere.* 1992.

[39] P. B. Hays, R. A. Jones, and M. H. Rees. Auroral heating and the composition of the neutral atmosphere. *Planetary and Space Science* , 21:559–573, April 1973.

[40] R. A. Heelis and W. R. Coley. Global and local Joule heating effects seen by DE 2. *Journal of Geophysical Research (SpacePhysics)* , 93:7551–7557, July 1988.

[41] R. A. Heelis, J. K. Lowell, and R. W. Spiro. A model of the high-latitude ionospheric convection pattern. *Journal of Geophysical Research (SpacePhysics)* , 87:6339–6345, August 1982.

[42] H. E. Hinteregger. Representations of solar EUV fluxes for aeronomical applications. *Advances in Space Research* , 1:39–52, 1981.

[43] Y. Huang, Y. Deng, J. Lei, A. Ridley, R. Lopez, R. C. Allen, and B. Mac Butler. Comparison of Joule heating associated with high-speed solar wind

between different models and observations. *Journal of Atmospheric &Solar−Terrestrial Physics* , 75:5–14, February 2012.

[44] Y. Huang, A. D. Richmond, Y. Deng, and R. Roble. Height distribution of Joule heating and its influence on the thermosphere. *Journal of Geophysical Research (SpacePhysics)* , 117:8334, August 2012.

[45] A. J. Hundhausen. *Coronal Expansion and Solar Wind.* 1972.

[46] R. P. Kane. Some Implications Using the Group Sunspot Number Reconstruction. *Sol.Phys.* , 205:383–401, February 2002.

[47] M. C. Kelley. *The Earth's Ionosphere.* 1989.

[48] M. C. Kelley, D. J. Knudsen, and J. F. Vickrey. Poynting flux measurements on a satellite - A diagnostic tool for space research. *Journal of Geophysical Research (SpacePhysics)* , 96:201–207, January 1991.

[49] E. A. Kihn, R. Redmon, A. J. Ridley, and M. R. Hairston. A statistical comparison of the AMIE derived and DMSP-SSIES observed high-latitude ionospheric electric field. *Journal of Geophysical Research (SpacePhysics)* , 111:8303, August 2006.

[50] J. H. King and N. E. Papitashvili. Solar wind spatial scales in and comparisons of hourly Wind and ACE plasma and magnetic field data. *Journal of Geophysical Research (SpacePhysics)* , 110:2104, February 2005.

[51] M. G. Kivelson and C. T. Russell. *Introduction to Space Physics.* April 1995.

[52] D. J. Knipp, W. K. Tobiska, and B. A. Emery. Direct and Indirect Thermospheric Heating Sources for Solar Cycles 21-23. *Sol.Phys.* , 224:495–505, October 2004.

[53] D. J. Knipp, T. Welliver, M. G. McHarg, F. K. Chun, W. K. Tobiska, and D. Evans. Climatology of extreme upper atmospheric heating events. *Advances in Space Research* , 36:2506–2510, 2005.

[54] Y.-S. Kwak, K.-H. Kim, Y. Deng, and J. M. Forbes. Response of thermosphere density to changes in interplanetary magnetic field sector polarity. *Journal of Geophysical Research (SpacePhysics)* , 116:11316, November 2011.

[55] J. L. Lean, R. R. Meier, J. M. Picone, and J. T. Emmert. Ionospheric total electron content: Global and hemispheric climatology. *Journal of Geophysical Research (SpacePhysics)* , 116:10318, October 2011.

[56] J. L. Lean, J. M. Picone, J. T. Emmert, and G. Moore. Thermospheric densities derived from spacecraft orbits: Application to the Starshine satellites. *Journal of Geophysical Research (SpacePhysics)* , 111:4301, April 2006.

[57] J. Lei, J. P. Thayer, A. G. Burns, G. Lu, and Y. Deng. Wind and temperature effects on thermosphere mass density response to the November 2004 geomagnetic storm. *Journal of Geophysical Research (SpacePhysics)* , 115:5303, May 2010.

[58] J. Lei, J. P. Thayer, J. M. Forbes, E. K. Sutton, and R. S. Nerem. Rotating solar coronal holes and periodic modulation of the upper atmosphere. *Geophysical Research Letters* , 35:10109, May 2008.

[59] J. Lei, J. P. Thayer, J. M. Forbes, Q. Wu, C. She, W. Wan, and W. Wang. Ionosphere response to solar wind high-speed streams. *Geophysical Research Letters* , 35:19105, October 2008.

[60] L. Liu, Y. Chen, H. Le, V. I. Kurkin, N. M. Polekh, and C.-C. Lee. The ionosphere under extremely prolonged low solar activity. *Journal of Geophysical Research (SpacePhysics)* , 116:4320, April 2011.

[61] N. R. Lomb. Least-squares frequency analysis of unequally spaced data. *Ap&SS* , 39:447–462, February 1976.

[62] G. Lu, D. N. Baker, R. L. McPherron, C. J. Farrugia, D. Lummerzheim, J. M. Ruohoniemi, F. J. Rich, D. S. Evans, R. P. Lepping, M. Brittnacher, X. Li, R. Greenwald, G. Sofko, J. Villain, M. Lester, J. Thayer, T. Moretto, D. Milling, O. Troshichev, A. Zaitzev, V. Odintzov, G. Makarov, and K. Hayashi. Global energy deposition during the January 1997 magnetic cloud event. *Journal of Geophysical Research (SpacePhysics)* , 103:11685–11694, June 1998.

[63] G. Lu, M. G. Mlynczak, L. A. Hunt, T. N. Woods, and R. G. Roble. On the relationship of Joule heating and nitric oxide radiative cooling in the thermosphere. *Journal of Geophysical Research (SpacePhysics)* , 115:5306, May 2010.

[64] G. Lu, A. D. Richmond, B. A. Emery, and R. G. Roble. Magnetosphere-ionosphere-thermosphere coupling: Effect of neutral winds on energy transfer and field-aligned current. *Journal of Geophysical Research (SpacePhysics)* , 100:19643–19660, October 1995.

[65] L. R. Lyons. Formation of auroral arcs via magnetosphere-ionosphere coupling. *Reviews of Geophysics*, 30:93–112, May 1992.

[66] T. Matsuo, A. D. Richmond, and K. Hensel. High-latitude ionospheric electric field variability and electric potential derived from DE-2 plasma drift measurements: Dependence on IMF and dipole tilt. *Journal of Geophysical Research (SpacePhysics)* , 108:1005, January 2003.

[67] D. J. McComas, R. W. Ebert, H. A. Elliott, B. E. Goldstein, J. T. Gosling, N. A. Schwadron, and R. M. Skoug. Weaker solar wind from the polar coronal

holes and the whole Sun. *Geophysical Research Letters* , 35:18103, September 2008.

[68] M. McHarg, F. Chun, D. Knipp, G. Lu, B. Emery, and A. Ridley. High-latitude Joule heating response to IMF inputs. *Journal of Geophysical Research (SpacePhysics)* , 110:8309, August 2005.

[69] G. Michalek. Two types of flare-associated coronal mass ejections. *A&A* , 494:263–268, January 2009.

[70] A. P. Mitra, editor. *Ionospheric effects of solar flares*, volume 46 of *Astrophysics and Space Science Library*, 1974.

[71] M. Mlynczak, F. J. Martin-Torres, J. Russell, K. Beaumont, S. Jacobson, J. Kozyra, M. Lopez-Puertas, B. Funke, C. Mertens, L. Gordley, R. Picard, J. Winick, P. Wintersteiner, and L. Paxton. The natural thermostat of nitric oxide emission at 5.3 μm in the thermosphere observed during the solar storms of April 2002. *Geophysical Research Letters* , 30(21):210000–1, November 2003.

[72] E. I. Mogilevsky, V. N. Obridko, and N. S. Shilova. Large-Scale Magnetic Field Structures and Coronal Holes on the Sun. *Sol.Phys.* , 176:107–121, November 1997.

[73] D. J. Mullan. Solar Physics: From the Deep Interior to the Hot Corona. In D. Page and J. G. Hirsch, editors, *From the Sun to the Great Attractor*, volume 556 of *Lecture Notes in Physics, Berlin Springer Verlag*, page 1, 2000.

[74] P. T. Newell, T. Sotirelis, K. Liou, and F. J. Rich. Pairs of solar wind-magnetosphere coupling functions: Combining a merging term with a viscous term works best. *Journal of Geophysical Research (SpacePhysics)* , 113:4218, April 2008.

[75] High Altitude Observatory. TIEGCM V1.94 model description. *Natl. Cent. for Atmos. Res., Boulder, Colo.*, 2011.

[76] J. A. Ottley and R. W. Schunk. Density and temperature structure of helium ions in the topside polar ionosphere for subsonic outflows. *Journal of Geophysical Research (SpacePhysics)* , 85:4177–4190, August 1980.

[77] M. Palmroth, T. I. Pulkkinen, P. Janhunen, D. J. McComas, C. W. Smith, and H. E. J. Koskinen. Role of solar wind dynamic pressure in driving ionospheric Joule heating. *Journal of Geophysical Research (SpacePhysics)* , 109:11302, November 2004.

[78] V. O. Papitashvili and F. J. Rich. High-latitude ionospheric convection models derived from Defense Meteorological Satellite Program ion drift observations and parameterized by the interplanetary magnetic field strength and direction. *Journal of Geophysical Research (SpacePhysics)* , 107:1198, August 2002.

[79] E. N. Parker. Dynamics of the Interplanetary Gas and Magnetic Fields. *ApJ* , 128:664, November 1958.

[80] E. N. Parker. Dynamical Theory of the Solar Wind. *Space Sci. Rev.* , 4:666–708, September 1965.

[81] K. J. H. Phillips. *Guide to the Sun.* March 1995.

[82] J. M. Picone, A. E. Hedin, D. P. Drob, and A. C. Aikin. NRLMSISE-00 empirical model of the atmosphere: Statistical comparisons and scientific issues. *Journal of Geophysical Research (SpacePhysics)* , 107:1468, December 2002.

[83] L. A. Pustil'Nik and G. Y. Din. Influence of solar activity on the state of the wheat market in medieval England. *Sol.Phys.* , 223:335–356, September 2004.

[84] L. Qian. Modeling Thermospheric Neutral Density. *Pennsylvania State University*, 2007.

[85] L. Qian, A. G. Burns, P. C. Chamberlin, and S. C. Solomon. Variability of thermosphere and ionosphere responses to solar flares. *Journal of Geophysical Research (SpacePhysics)* , 116:10309, October 2011.

[86] L. Qian and S. C. Solomon. Thermospheric Density: An Overview of Temporal and Spatial Variations. *Space Sci. Rev.* , 168:147–173, June 2012.

[87] L. Qian, S. C. Solomon, and T. J. Kane. Seasonal variation of thermospheric density and composition. *Journal of Geophysical Research (SpacePhysics)* , 114:1312, January 2009.

[88] L. Qian, S. C. Solomon, and M. G. Mlynczak. Model simulation of thermospheric response to recurrent geomagnetic forcing. *Journal of Geophysical Research (SpacePhysics)* , 115:10301, October 2010.

[89] W. J. Raitt, R. W. Schunk, and P. M. Banks. Quantitative calculations of helium ion escape fluxes from the polar ionospheres. *Journal of Geophysical Research (SpacePhysics)* , 83:5617–5623, December 1978.

[90] M. H. Rees, K. Stamnes, B. A. Emery, and R. G. Roble. Neutral and ion gas heating by auroral electron precipitation. *Journal of Geophysical Research (SpacePhysics)* , 88:6289–6300, August 1983.

[91] C. Reigber, H. Lühr, and P. Schwintzer. CHAMP mission status. *Advances in Space Research* , 30:129–134, July 2002.

[92] P. G. Richards, J. A. Fennelly, and D. G. Torr. EUVAC: A solar EUV flux model for aeronomic calculations. *Journal of Geophysical Research (SpacePhysics)* , 99:8981–8992, May 1994.

[93] P. G. Richards, R. W. Schunk, and J. J. Sojka. Large-scale counterstreaming of H(+) and He(+) along plasmaspheric flux tubes.

Journal of Geophysical Research (SpacePhysics) , 88:7879–7886, October 1983.

[94] I. G. Richardson and H. V. Cane. Near-Earth Interplanetary Coronal Mass Ejections During Solar Cycle 23 (1996 - 2009): Catalog and Summary of Properties. *Sol.Phys.* , 264:189–237, June 2010.

[95] A. D. Richmond. Assimilative mapping of ionospheric electrodynamics. *Advances in Space Research* , 12:59–68, 1992.

[96] A. D. Richmond. On the ionospheric application of Poynting's theorem. *Journal of Geophysical Research (SpacePhysics)* , 115:10311, October 2010.

[97] A. D. Richmond and Y. Kamide. Mapping electrodynamic features of the high-latitude ionosphere from localized observations - Technique. *Journal of Geophysical Research (SpacePhysics)* , 93:5741–5759, June 1988.

[98] A. D. Richmond, Y. Kamide, S.-I. Akasofu, D. Alcayde, and M. Blanc. Global measures of ionospheric electrodynamic activity inferred from combined incoherent scatter radar and ground magnetometer observations. *Journal of Geophysical Research (SpacePhysics)* , 95:1061–1071, February 1990.

[99] A. D. Richmond, G. Lu, B. A. Emery, and D. J. Knipp. The AMIE procedure: prospects for space weather specification and prediction. *Advances in Space Research* , 22:103–112, 1998.

[100] A. D. Richmond, E. C. Ridley, and R. G. Roble. A thermosphere/ionosphere general circulation model with coupled electrodynamics. *Geophysical Research Letters* , 19:601–604, March 1992.

[101] A. J. Ridley, Y. Deng, and G. Tóth. The global ionosphere thermosphere model. *Journal of Atmospheric &Solar – Terrestrial Physics* , 68:839–864, May 2006.

[102] A. J. Ridley and E. A. Kihn. Polar cap index comparisons with AMIE cross polar cap potential, electric field, and polar cap area. *Geophysical Research Letters* , 31:7801, April 2004.

[103] R. G. Roble and E. C. Ridley. An auroral model for the NCAR thermospheric general circulation model (TGCM). *Annales Geophysicae*, 5:369–382, December 1987.

[104] R. G. Roble and E. C. Ridley. An auroral model for the NCAR thermospheric general circulation model (TGCM). *Annales Geophysicae*, 5:369–382, December 1987.

[105] R. G. Roble and E. C. Ridley. A thermosphere-ionosphere-mesosphere-electrodynamics general circulation model (time-GCM): Equinox solar cycle minimum simulations (30-500 km). *Geophysical Research Letters* , 21:417–420, March 1994.

[106] R. G. Roble, E. C. Ridley, and R. E. Dickinson. On the global mean structure of the thermosphere. *Journal of Geophysical Research (SpacePhysics)* , 92:8745–8758, August 1987.

[107] R. G. Roble, E. C. Ridley, A. D. Richmond, and R. E. Dickinson. A coupled thermosphere/ionosphere general circulation model. *Geophysical Research Letters* , 15:1325–1328, November 1988.

[108] G. Rottman. Solar UV Irradiance Measurements: The UARS and EOS SOLSTICE. *Physics and Chemistry of the Earth C*, 25:401–404, 2000.

[109] J. D. Scargle. Studies in astronomical time series analysis. II - Statistical aspects of spectral analysis of unevenly spaced data. *ApJ* , 263:835–853, December 1982.

[110] K. H. Schatten, J. M. Wilcox, and N. F. Ness. A model of interplanetary and coronal magnetic fields. *Sol.Phys.* , 6:442–455, March 1969.

[111] R. W. Schunk and A. F. Nagy. *Ionospheres.* November 2004.

[112] D. G. Sibeck, R. E. Lopez, and E. C. Roelof. Solar wind control of the magnetopause shape, location, and motion. *Journal of Geophysical Research* (*SpacePhysics*) , 96:5489–5495, April 1991.

[113] S. P. Slinker, J. A. Fedder, B. A. Emery, K. B. Baker, D. Lummerzheim, J. G. Lyon, and F. J. Rich. Comparison of global MHD simulations with AMIE simulations for the events of May 19-20, 1996. *Journal of Geophysical Research* (*SpacePhysics*) , 104:28379–28396, 1999.

[114] H. B. Snodgrass and R. K. Ulrich. Rotation of Doppler features in the solar photosphere. *ApJ* , 351:309–316, March 1990.

[115] J. J. Sojka, R. L. McPherron, A. P. van Eyken, M. J. Nicolls, C. J. Heinselman, and J. D. Kelly. Observations of ionospheric heating during the passage of solar coronal hole fast streams. *Geophysical Research Letters* , 36:19105, October 2009.

[116] S. C. Solomon and L. Qian. Solar extreme-ultraviolet irradiance for general circulation models. *Journal of Geophysical Research* (*SpacePhysics*) , 110:10306, October 2005.

[117] S. C. Solomon, L. Qian, L. V. Didkovsky, R. A. Viereck, and T. N. Woods. Causes of low thermospheric density during the 2007-2009 solar minimum. *Journal of Geophysical Research* (*SpacePhysics*) , 116:0, July 2011.

[118] S. C. Solomon, L. Qian, G. R. Gladstone, S. M. Bailey, and E. M. Rodgers. Thermospheric Response to Solar EUV during Quiet and Flare Conditions. *AGU Fall Meeting Abstracts*, page A1108, December 2005.

[119] S. C. Solomon, T. N. Woods, L. V. Didkovsky, J. T. Emmert, and L. Qian. Anomalously low solar extreme-ultraviolet irradiance and thermospheric density during solar minimum. *Geophysical Research Letters* , 37:16103, August 2010.

[120] R. S. Stolarski. Energetics of the midlatitude thermosphere. *Journal of Atmospheric &Solar – Terrestrial Physics* , 38:863–868, August 1976.

[121] D. F. Strobel. Parameterization of the atmospheric heating rate from 15 to 120 km due to O2 and O3 absorption of solar radiation. *Journal of Geophysical Research (SpacePhysics)* , 83:6225–6230, December 1978.

[122] E. K. Sutton, J. M. Forbes, and D. J. Knipp. Rapid response of the thermosphere to variations in Joule heating. *Journal of Geophysical Research (SpacePhysics)* , 114:4319, April 2009.

[123] E. K. Sutton, J. M. Forbes, and R. S. Nerem. Global thermospheric neutral density and wind response to the severe 2003 geomagnetic storms from CHAMP accelerometer data. *Journal of Geophysical Research (SpacePhysics)* , 110:9, September 2005.

[124] E. K. Sutton, J. M. Forbes, R. S. Nerem, and T. N. Woods. Neutral density response to the solar flares of October and November, 2003. *Geophysical Research Letters* , 33:22101, November 2006.

[125] E. K. Sutton, R. S. Nerem, and J. M. Forbes. Density and Winds in the Thermosphere Deduced from Accelerometer Data. *Journal of Spacecraft and Rockets*, 44:1210–1219, November 2007.

[126] E. Tandberg-Hanssen and A. G. Emslie. *The physics of solar flares.* 1988.

[127] T. F. Tascione. *Introduction to the space environment.* 1988.

[128] M. Temmer, B. Vršnak, and A. M. Veronig. Periodic Appearance of Coronal Holes and the Related Variation of Solar Wind Parameters. *Sol.Phys.* , 241:371–383, April 2007.

[129] J. P. Thayer. Height-resolved Joule heating rates in the high-latitude formula E region and the influence of neutral winds. *Journal of Geophysical Research (SpacePhysics)* , 103:471–487, January 1998.

[130] J. P. Thayer, J. Lei, J. M. Forbes, E. K. Sutton, and R. S. Nerem. Thermospheric density oscillations due to periodic solar wind high-speed streams. *Journal of Geophysical Research (SpacePhysics)* , 113:6307, June 2008.

[131] J. P. Thayer and J. Semeter. The convergence of magnetospheric energy flux in the polar atmosphere. *Journal of Atmospheric &Solar−Terrestrial Physics* , 66:807–824, July 2004.

[132] J. P. Thayer, J. F. Vickrey, R. A. Heelis, and J. B. Gary. Interpretation and modeling of the high-latitude electromagnetic energy flux. *Journal of Geophysical Research (SpacePhysics)* , 100:19715–19728, October 1995.

[133] N. R. Thomson, C. J. Rodger, and R. L. Dowden. Ionosphere gives size of greatest solar flare. *Geophysical Research Letters* , 31:6803, March 2004.

[134] M. R. Torr, D. G. Torr, and P. G. Richards. A new determination of the ultraviolet heating efficiency of the thermosphere. *Journal of Geophysical Research (SpacePhysics)* , 85:6819–6826, December 1980.

[135] B. T. Tsurutani, D. L. Judge, F. L. Guarnieri, P. Gangopadhyay, A. R. Jones, J. Nuttall, G. A. Zambon, L. Didkovsky, A. J. Mannucci, B. Iijima, R. R. Meier, T. J. Immel, T. N. Woods, S. Prasad, L. Floyd, J. Huba, S. C. Solomon,

P. Straus, and R. Viereck. The October 28, 2003 extreme EUV solar flare and resultant extreme ionospheric effects: Comparison to other Halloween events and the Bastille Day event. *Geophysical Research Letters* , 32:3, January 2005.

[136] R. A. Viereck, L. E. Floyd, P. C. Crane, T. N. Woods, B. G. Knapp, G. Rottman, M. Weber, L. C. Puga, and M. T. DeLand. A composite Mg II index spanning from 1978 to 2003. *Space Weather* , 2:5, October 2004.

[137] W. Wang. A thermosphere-ionosphere nested grid (TING) model. *University of Michigan*, 1998.

[138] D. R. Weimer. Models of high-latitude electric potentials derived with a least error fit of spherical harmonic coefficients. *Journal of Geophysical Research* (*SpacePhysics*) , 100:19595–19608, October 1995.

[139] D. R. Weimer. A flexible, IMF dependent model of high-latitude electric potentials having "space weather" applications. *Geophysical Research Letters* , 23:2549–2552, 1996.

[140] D. R. Weimer. An improved model of ionospheric electric potentials including substorm perturbations and application to the Geospace Environment Modeling November 24, 1996, event. *Journal of Geophysical Research* (*SpacePhysics*) , 106:407–416, January 2001.

[141] D. R. Weimer. Improved ionospheric electrodynamic models and application to calculating Joule heating rates. *Journal of Geophysical Research* (*SpacePhysics*) , 110:5306, May 2005.

[142] D. R. Weimer. Predicting surface geomagnetic variations using ionospheric electrodynamic models. *Journal of Geophysical Research* (*SpacePhysics*) , 110:12307, December 2005.

[143] D. R. Weimer, B. R. Bowman, E. K. Sutton, and W. K. Tobiska. Predicting global average thermospheric temperature changes resulting from auroral heating. *Journal of Geophysical Research* (*SpacePhysics*) , 116:1312, January 2011.

[144] F. D. Wilder, G. Crowley, B. J. Anderson, and A. D. Richmond. Intense dayside Joule heating during the 5 April 2010 geomagnetic storm recovery phase observed by AMIE and AMPERE. *Journal of Geophysical Research (Space Physics)*, 117:5207, May 2012.

[145] G. R. Wilson, D. R. Weimer, J. O. Wise, and F. A. Marcos. Response of the thermosphere to Joule heating and particle precipitation. *Journal of Geophysical Research* (*SpacePhysics*) , 111:10314, October 2006.

[146] T. N. Woods, F. G. Eparvier, S. M. Bailey, P. C. Chamberlin, J. Lean, G. J. Rottman, S. C. Solomon, W. K. Tobiska, and D. L. Woodraska. Solar EUV Experiment (SEE): Mission overview and first results. *Journal of Geophysical Research* (*SpacePhysics*) , 110:1312, January 2005.

[147] T. N. Woods, F. G. Eparvier, R. Hock, A. R. Jones, D. Woodraska, D. Judge, L. Didkovsky, J. Lean, J. Mariska, H. Warren, D. McMullin, P. Chamberlin, G. Berthiaume, S. Bailey, T. Fuller-Rowell, J. Sojka, W. K. Tobiska, and R. Viereck. Extreme Ultraviolet Variability Experiment (EVE) on the Solar Dynamics Observatory (SDO): Overview of Science Objectives, Instrument Design, Data Products, and Model Developments. *Sol.Phys.* , 275:115–143, January 2012.

[148] T. N. Woods, R. Hock, F. Eparvier, A. R. Jones, P. C. Chamberlin, J. A. Klimchuk, L. Didkovsky, D. Judge, J. Mariska, H. Warren, C. J. Schrijver, D. F. Webb, S. Bailey, and W. K. Tobiska. New Solar Extreme-ultraviolet Irradiance Observations during Flares. *ApJ* , 739:59, October 2011.

[149] T. N. Woods and G. J. Rottman. *Solar Ultraviolet Variability Over Time Periods of Aeronomic Interest*, page 221. 2002.

[150] W. Xu. Energy budget in the coupling processes of the solar wind, magnetosphere and ionosphere. *Chin. J. Space Sci.*, 2011.

[151] D. H. Zhang, X. H. Mo, L. Cai, W. Zhang, M. Feng, Y. Q. Hao, and Z. Xiao. Impact factor for the ionospheric total electron content response to solar flare irradiation. *Journal of Geophysical Research (SpacePhysics)* , 116:4311, April 2011.

[152] X. X. Zhang, C. Wang, T. Chen, Y. L. Wang, A. Tan, T. S. Wu, G. A. Germany, and W. Wang. Global patterns of Joule heating in the high-latitude ionosphere. *Journal of Geophysical Research (SpacePhysics)* , 110:12208, December 2005.

[153] Y. Zhang and L. J. Paxton. An empirical Kp-dependent global auroral model based on TIMED/GUVI FUV data. *Journal of Atmospheric &Solar − Terrestrial Physics* , 70:1231–1242, June 2008.

[154] Y. Zhang, L. J. Paxton, and D. Morrison. Auroral and thermospheric response to the 9 day periodic variations in the dayside reconnection rate in 2005. *Space Weather* , 8:7001, July 2010.

[155] J. B. Zirker. *Journey from the center of the sun.* 2002.

BIOGRAPHICAL STATEMENT

Yanshi Huang graduated from University of Science and Technology of China in 2007, with a Bachelor of Science degree in Space Physics. From 2007 to 2009, Yanshi continued to pursue a Master of Science in Atmospheric and Space Science at University of Michigan, analyzing data from Galileo Spacecraft and using Space Weather Modeling Framework to do numerical simulations.

In August 2009, Yanshi attended University of Texas at Arlington for a Doctorate of Philosophy in Applied Physics. Under the guidance of Dr. Yue Deng, Yanshi worked on several different research projects, such as improving the quantitive understanding of the solar wind/magnetosphere/ionosphere coupling process by comparing Joule heating results between different models and observations. Yanshi was selected by the Graduate Visitor Program/Advanced Study Program twice, and visited the High Altitude Observatory at the National Center for Atmospheric Research during summers, collaborating with scientists for different projects.

In 2011, Yanshi was presented with the Outstanding Physics Major Award in the Physics Department for her academic and research achievement. The poster presented by Yanshi at 2011 CEDAR-GEM joint meeting was awarded the second prize of Ionosphere-Thermosphere competitions. In 2012, Yanshi was honored the 2012 Texas Section of the American Physical Society Robert S. Hyer Research Award for her excellent research and potential impact in the relevant scientific community.

Yanshi was the first author of three scientific papers, one published, one in press and one submitted. Yanshi also co-authored other five papers which are published or in press.